UNIVERSIDAD NACIONAL AUTÓNOMA DE MÉXICO
POSGRADO EN CIENCIA E INGENIERÍA DE MATERIALES
INSTITUTO DE INVESTIGACIÓN EN MATERIALES
CENTRO DE FÍSICA APLICADA Y TECNOLOGÍA AVANZADA

CORRELATION BETWEEN THE THERMAL, ELECTRICAL, AND STRUCTURAL PROPERTIES FOR *p*-TYPE SILICON

TESIS
QUE PARA OPTAR POR EL GRADO DE:
MAESTRO EN CIENCIA E INGENIERÍA DE MATERIALES

PRESENTA
FIS. HAROL DAVID MARTÍNEZ HERNÁNDEZ

TUTOR
DR. MARIO ENRIQUE RODRÍGUEZ GARCÍA
CENTRO DE FÍSICA APLICADA Y TECNOLOGÍA AVANZADA

COMITÉ TUTOR
DR. ERIC MAURICIO RIVERA MUÑOZ
CENTRO DE FÍSICA APLICADA Y TECNOLOGÍA AVANZADA
DR. RAFAEL RAMÍREZ BON
CENTRO DE INVESTIGACIÓN Y DE ESTUDIOS AVANZADOS

JURIQUILLA, QUERÉTARO. OCTUBRE DE 2021

Acknowledgments

I thank my parents for being fundamental support during my educational process.

I appreciate my main tutor, Dr. Mario Enrique Rodríguez, for opening his laboratory doors to me to carry out this thesis. His fraternity and humor sense have been fundamental to my formation as a researcher and as a person.

I render thanks to my tutoring committee.

I warm thanks to my radiometry labmates.

I thankfulness to Centro de Física Aplicada y Tecnología Avanzada, UNAM, Campus Juriquilla, in which this thesis was developed, to its academics and technicians who supported this research work.

I thank Consejo Nacional de Ciencia y Tecnología (CONACYT) for financial support for my master's studies.

I gratefulness to the National Materials Characterization Laboratory (LaNCaM) for the X-ray diffraction measurements.

I thank the PAEP for the financial support to present the results of this work at international conferences.

I am grateful to Dra. Beatriz Millán Malo for the X-Ray diffraction measurements.

Contents

FIGURES LIST

TABLES LIST

Abstract

Thermophysical properties of semiconductor materials used in the electronics industry must be studied to enhance electronic device design and integrated circuits, where electro-thermal interactions play a significant role in performance. These materials can transport heat and energy via lattice vibrations and free electrons. In monocrystalline structures, their structural properties determine thermal and electrical ones. Here, it was investigated the effect of defects induced by intrinsic and extrinsic parameters on the thermal and electrical properties. The manufacturing processes and samples preparation in *p*-type silicon wafers with different carrier concentrations were considered. Photoacoustic technique and thermal relaxation method sensed local variations in the thermal diffusivity and volumetric heat capacity, respectively. These variations are due to the local changes in the defect density produced by polishing processes and doping inclusion. The Hall effect sensed the effective carrier lifetime changes by the presence of defects in the crystalline structure. The carrier distribution was determined by photothermal and photocarrier images allowing to see local variations in the boron distribution. The crystalline quality obtained by studying the FWHM of the X-Ray diffraction patterns elucidated the effect of samples polishing and preparation on the thermal properties and the carrier concentration effect on the structural properties. Photothermal techniques sensed local variations in the defect densities and the carrier distribution.

Resumen

Las propiedades termofísicas de los materiales semiconductores utilizados en la industria electrónica deben estudiarse para mejorar el diseño de los dispositivos electrónicos y los circuitos integrados, donde las interacciones electrotérmicas desempeñan un papel importante en su rendimiento. Estos materiales pueden transportar calor y energía a través de las vibraciones de la red y los electrones libres. En las estructuras monocristalinas, sus propiedades estructurales determinan las propiedades térmicas y eléctricas. En este trabajo se investigó el efecto de los defectos inducidos por parámetros intrínsecos y extrínsecos sobre las propiedades térmicas y eléctricas durante los procesos de fabricación y preparación de muestras de obleas de silicio tipo *p* con diferentes concentraciones de portadores. La técnica fotoacústica y el método de relajación térmica detectaron variaciones locales en la difusividad térmica y la capacidad calorífica volumétrica, respectivamente. Estas variaciones se deben a los cambios locales en la densidad de defectos producidos por los procesos de pulido y por la inclusión de dopaje. El efecto Hall detectó los cambios en el tiempo de vida efectivo de los portadores por la presencia de defectos en la estructura cristalina. La distribución de portadores se determinó mediante imágenes fototérmicas y de fotoportadores que permitieron ver las variaciones locales en la distribución del boro. La calidad cristalina obtenida mediante el estudio del FWHM de los patrones de difracción de rayos X dilucidó el efecto del pulido y de la preparación de las muestras en las propiedades térmicas, así como el efecto de la concentración de portadores en las propiedades estructurales. Las técnicas fototérmicas detectaron variaciones locales en las densidades de defectos y en la distribución de portadores.

CHAPTER 1

Introduction

Thermoelectric properties in semiconductor materials depend on the behavior of the carrier charges, the lattice, and the interaction between these. The knowledge of the properties is essential for developing different devices to take advantage of the properties for various applications. The electronic industry is a case where it is used the mixture of different materials with particular optical, thermal, and electrical properties for applications in distinct areas. The development of new and better semiconductor materials has allowed significant advances in devices and integrated circuit design and the development of more accurate new characterization techniques. The awareness of the thermoelectric properties is fundamental because the performance of one electronic device is determined by the ability to diffuse heat. Also, the electric conductivity is a function of the temperature limiting the flawless operation of a particular device. A lot of the semiconductor material properties are defined by the material structure and defects, such as dislocations, inclusions, vacancies, stacking faults, and grain boundaries. In the particular case of silicon (Si), its thermal properties do not depend only on the density of states; also, these are dependent on the thermoelectric distribution and the crystalline quality, which define the electric resistivity.

Intrinsic (carrier distribution, lifetime of carriers, diffusion coefficient, recombination velocity) and extrinsic (defect densities, pressure for growing, annealing) parameters are involved in machining Si wafers. It is well known that the pressure applied during semiconductor crystal growing depends on the diffusion of chemical species. In this way, the growth rate is roughly constant for low pressures, and for high pressures, this rate decreases. Crystals are grown using a pressure where the growth rate is minimum so that the diffusion of the chemical species is favored. Their diffusion determines the carrier distribution and the structure of the crystal, which are directly related to the thermoelectric properties.

The effect of mechanical damages in Si wafers has been studied using different contact and non-contact techniques correlated to the thermal properties. Photothermal radiometry (PTR) was used to find the carrier lifetimes and the effective thermal diffusivity when mechanical damage is introduced. An average recombination lifetime is posed; it includes the bulk and the surface recombination lifetime. A decrease in the thermal diffusivity associated with the surface state was found. It is necessary to refer to an effective thermal diffusivity conformed by the rough surface and the below layer [1].

Thermal annealing repair structural damages in monocrystalline Si; chemical and electrical properties can be recovered to their original states to some extent [2]. On the other hand, defect densities appear in the crystal structure when Si wafers are manufactured due to surface polishing. A surface mechanical polishing process generates 10^2 cm^{-2} defect density, and a surface chemical polishing process generates 10^6 cm^{-2}. There is a great deformation in the wafer surface by mechanical polishing compared with chemical polishing; thermal oxidation corrects the deformation due to mechanical polishing [3]. A chemical etching conformed by HF/HNO_3 and conductive atomic force microscopy (CAFM) was used to identify ultrathin amorphous damage on monocrystalline Si. An appropriated HF/HNO_3 mixture eliminates the apparition amorphous damage upon the machining process [4]. The works previously cited do not report a correlation between thermoelectric properties and structural damages on Si.

Directly and indirectly measurements for the thermal conductivities on silicon and germanium (Ge) have been reported. The measurements were carried out from 3 K to their melting points to find electronic and phononic contributions to the thermal conductivity. Only phonons contribute to the heat transport up to 700 K and 1000 K on Si and Ge, respectively, close to their melting points; the electronic contribution appears to represent 40 % of the total thermal conductivity [5,6]. Nevertheless, the sample preparation is not reported; it is unclear if the samples were cut, which can modify the crystal structure, introduce defects, and affect the thermal conductivity results. The defects reduce the thermal phonon flux producing a decrease in the heat flux by dispersion.

There is a correlation between crystalline quality and thermoelectric properties. The full width at half maximum (FWHM) of a peak in X-ray diffraction (DRX) measurement characterizes the material crystalline quality. High crystalline quality implies a low FWHM, and low crystalline quality implies a high FWHM [7]. Thermoelectric properties measured in function of temperature for *n*-type and *p*-type Si cut rectangular bars (23 mm × 6.5 mm) present an excellent agreement with first-principle calculations for the Seebeck coefficient [8]. The thermal conductivity results were compared with data obtained by using sophisticated measurement systems that measure the complete Si wafers. But, in this report, it is not considered the defects produced by the cutting. It is not possible that the measured values for thermal conductivity agree with report values because structural damages are introduced. Likewise, the Seebeck coefficient comes from a diffusive model, and it is affected by structural changes since the lifetime of the carriers decreases. Seebeck coefficient values should not agree with first-principles calculations.

This work presents the changes in the volumetric heat capacity, thermal diffusivity, and conductivity of Si samples with different resistivity considering the effects of the damages introduced by the sample preparation and the manufacturing processes. Photoacoustic was used to determine the thermal diffusivity, and the relaxation method was used to determine the volumetric heat capacity; the thermal conductivity was calculated. Electrical properties were obtained by the four-point method and a Hall effect system. The resistivity for each one of the samples was measured, and it was calculated the carrier concentration. An apparent increase in carrier concentration is reported, and it is correlated with a carrier lifetime change produced by the defects. Finally, the crystalline quality of the samples was obtained by studying the changes in the FWHM of the X-ray diffraction patterns. A correlation between thermal, electrical, and structural properties is reported.

CHAPTER 2

Electrical Properties in Semiconductors

Paul Drude explained the transport properties of electrons in materials (especially metals) in 1900. The fundamental hypothesis of Drude model is to consider the valence electrons like free electrons, and these can be treated like molecules in kinetic gas theory. The model also supposes that the electrons experiment collisions almost instantaneously; while the collisions occur, the electrons are in thermal equilibrium at temperature T; the electrons travel straight line following Newton's laws.

The equation that describes the movement of a free electron in the presence of an electric and magnetic field is:

$$\vec{F} = -e\left(\vec{E} + \vec{v} \times \vec{B}\right) \tag{2.1}$$

Eq. (2.1), written for particles, also can be used for describing the movement of the electrons in plane wave states terms. If the particle is considered as a plane wave states superposition, the group velocity has the form:

$$\vec{v}_g = \frac{\hbar \vec{k}}{m_e} \tag{2.2}$$

In real materials is impossible to think of free electrons because there is electron dispersion due to defects and lattice vibrations, and to the collision between electrons too. The dispersion causes a decrease in the average momentum of the electrons, and it is considered a damping strength. It is defined τ as the mean free time elapsed in each collision; after each collision, the electrons return to the thermal equilibrium [9]. A constant electric field appears, giving the electrons an average speed corresponding to the time. This speed is known as drift speed given by:

$$\vec{v}_d = -\left(\frac{e\vec{E}}{m_e}\right)\tau \tag{2.3}$$

2.1. Electrical Resistivity and Conductivity

Electrical resistivity is an intrinsic property of materials of opposing the charge flux. Electrical conductivity is the inverse of resistivity and quantifies how a material conducts electricity. Consider a cross-section with uniform physical composition across the material; also, consider an electric field and a current density, parallels, and constants everywhere (see Fig. 2.1). Electrical resistivity can be calculated by:

$$\rho = R\frac{A}{L} \tag{2.4}$$

R represents the electrical resistance of a homogeneous material, l is the sample length, and A is the cross-section area. Resistance and resistivity are properties that describe the current flow through a material; resistivity is an intrinsic property, resistance does not. This implies that pure conductor wires of the same material have the same resistivity independent of size and shape, but a thin wire has a much larger resistance than a thick short conductor wire.

The electrical transport in a material can be quantified by the electrical conductivity σ defined as the proportionality constant between the electric current density $\vec{j}$ and the electric field $\vec{E}$:

$$\vec{j} = \sigma\vec{E} \tag{2.5}$$

The current density also can be defined in terms of the carrier density $\vec{j} = -en\vec{v}_d$, where n represents the carrier density [10]. By using Eqs. (2.3) and (2.5), the conductivity is:

$$\sigma = \frac{ne^2\tau}{m_e} \tag{2.6}$$

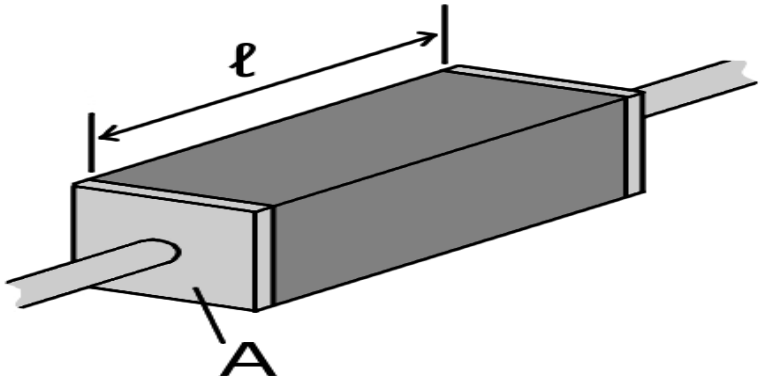

Figure 2.1: Schematic representation of a homogeneous material with length L, and cross-section area A.

2.1.1. Conductivity Causes

An atom or electron in a crystal can only exhibits exact energy levels, according to elementary quantum mechanics; energies between these levels are not allowed. When a group of such permitted levels has closely spaced energy values, i.e., energies that differ just slightly, the group is referred to as an "energy band." Depending on the atomic number of the component atoms and their arrangement inside the crystal, a material can have several such energy bands.

The electrons in the material try to reduce the overall energy in the material by settling into low-energy states; however, the Pauli exclusion principle says that only one may exist in each of these states. As a result, the electrons begin to "fill up" the band structure from the bottom. The Fermi level is the typical energy level to which the electrons have filled. For electrical conduction, the Fermi's level location to the band structure is critical: Only electrons in energy levels close to or above the Fermi level are free to travel into the broader material structure since electrons in that area may readily hop between partially occupied states. On the other hand, the low energy states are always filled with a set number of electrons, whereas the high energy states are always devoid of electrons.

An electron flow constitutes an electric current. There are numerous electron energy levels around the Fermi level in metals, thus there are a lot of electrons to travel about. This is what gives metals their great electronic conductivity.

One of the most significant aspects of band theory is the possibility of prohibited energy bands: energy intervals with no energy levels. The electron number in insulators and semiconductors is precisely the appropriate quantity to fill a specific integer number of low energy bands to the border. The Fermi level is within a bandgap in this situation. The electronic conductivity is very low because there are no accessible states at the Fermi level, and the electrons are not readily mobile [11].

Each atom in a metal has an outer shell of electrons that may easily split from their host atoms and move across the lattice. A positive ionic lattice is another name for this. The metal may carry electric current because of this sea of dissociable electrons. The resultant electric field leads electrons to wander towards the positive terminal when an electrical potential difference (voltage) is applied across the metal. Electrons real drift velocity is generally measured in meters per hour. However, even a sluggish drift velocity results in a significant current density due to the sheer quantity of traveling electrons. Although the mechanism is comparable to the momentum transfer of balls in a Newton's cradle, the rapid electric energy propagation along a wire is due to the propagation of an energy-carrying electromagnetic field directed by the wire rather than mechanical forces.

Electrical resistance is present in almost all metals. This may be described in simpler models (non-quantum mechanical theories) by substituting electrons and the crystal lattice with a wave-like structure. The waves interfere as the electron wave passes across the lattice, causing resistance. The minor disturbance and hence the less resistance, the more regular the

lattice is. Thus, two variables are primarily responsible for the quantity of resistance. The temperature, and therefore the crystal lattice vibration degree, are the first causes. Higher temperatures produce larger vibrations in the lattice, which behave as irregularities. Second, as the various ions mixing is also an irregularity, metal purity is important. The loss of long-range crystalline order causes a slight reduction in conductivity when pure metals are melted. The short-range order is preserved, and a significant correlation between ion locations leads to coherence between waves diffracted by nearby ions.

The Fermi level in metals is located in the conduction band, resulting in free conduction electrons. However, in semiconductors, the Fermi level is located inside the bandgap, about midway between the conduction band minimum and the valence band maximum (the top of the second band of filled electron energy levels). For intrinsic (undoped) semiconductors, this is true. This means there are no free conduction electrons at absolute zero temperature, and the resistance is infinite. On the other hand, the resistance falls as the charge carrier density (or, without going into too much detail, the density of electrons) in the conduction band rises. Dopant atoms enhance the predominant charge carrier concentration in extrinsic (doped) semiconductors by donating electrons to the conduction band or generating holes in the valence band. (A "hole" is a missing electron that behaves similarly to electrons.) Increased dopant density lowers resistance for both kinds of donor and acceptor atoms. As a result, heavily doped semiconductors exhibit a metallic behavior. The contribution of thermally produced carriers exceeds the contribution of dopant atoms at very high temperatures, and the resistance falls exponentially with temperature [10].

2.2. Electrical Mobility

Electrical mobility is the tendency of charged elementary particles (such as electrons or protons) to move, other than engaging in a stationary orbit (for example, within a given atom or molecule). When a uniform electric field acts upon a charged particle in a gas or liquid, it will be accelerated until it reaches a constant drift velocity according to the equation:

$$\vec{v}_d = \mu\vec{E} \tag{2.7}$$

where μ represents the electrical mobility being the proportionality constant between the drift speed and the electric field. From Eq. (2.3), the electrical mobility for electrons can be written as:

$$\mu_e = \frac{e\tau}{m_e} \tag{2.8}$$

In the semiconductor case where carriers are electrons (n) and holes (p) with mobilities μ_n, μ_p respectively, the resistivity and mobilities are related by:

$$\rho = \frac{1}{q(n\mu_n + \mu_p)} \tag{2.9}$$

In an extrinsic semiconductor where the majority carrier density is higher than the minority carrier density is possible to compute the resistivity value despising the minority carriers. In several cases, these are unknown parameters so that are necessary to use measurement techniques for ρ determination [12].

2.3. Hall Effect

Suppose an electric current is circulated along the x-direction through a conductor with a constant magnetic field along the z-direction. In that case, an electric field is established along the y-axis, perpendicular to the applied electric and magnetic fields, as indicated in Fig. 2.2. The apparition of the electric field in the y-axis is called Hall field, and it corresponds to the Hall effect. The equation of motion for the electron in an electric and a magnetic field is:

$$m\left(\frac{d\vec{v}}{dt}+\frac{\vec{v}}{\tau}\right)=-e\left(\vec{E}+\vec{v}\times\vec{B}\right) \tag{2.10}$$

The $\vec{v}/\tau$ term is a 'friction strength' due to the collisions, and $d\vec{v}/dt=0$. A three-equation system is possible to write from Eq. (2.10):

$$\begin{aligned} m\frac{v_x}{\tau} &= -eE_x + ev_yB \\ m\frac{v_y}{\tau} &= -eE_y + ev_xB \\ m\frac{v_z}{\tau} &= -eE_z \end{aligned} \tag{2.11}$$

Since the current cannot flow along the y-direction, there is an electric field component E_y such that $v_y=0$. E_y is the Hall field given by the second equation of the Syst. (2.11):

$$E_y = v_xB \tag{2.12}$$

From the first equation of the Syst. (2.11), and $v_y=0$:

$$v_x=-\frac{e\tau}{m}E_x \tag{2.13}$$

so that:

$$\frac{E_y}{E_x}=-\frac{eB\tau}{m} \tag{2.14}$$

By introducing the Hall coefficient $R_H=E_y/J_xB$ and using $J_x=ne^2\tau E_x/m$:

$$R_H = -\frac{eB\tau E_x/m}{ne^2\tau E_x B/m} \tag{2.15}$$

$$R_H = -\frac{1}{ne} \tag{2.16}$$

On the other hand, the Hall coefficient also can be written as follows:

$$R_H = -\frac{\rho e\tau}{m_e^*} \tag{2.17}$$

From Eqs. (2.16) and (2.17), the carrier concentration is given by:

$$n = \frac{m_e^*}{\rho\tau e^2} \tag{2.18}$$

Therefore, the Hall coefficient is negative for free electrons. The use of the Hall effect provides a tool for measuring the carrier density n and determining whether the carriers are electrons or holes. If the carriers are holes, the Hall coefficient is positive. As the carrier concentration decreases, the Hall coefficient increases [13].

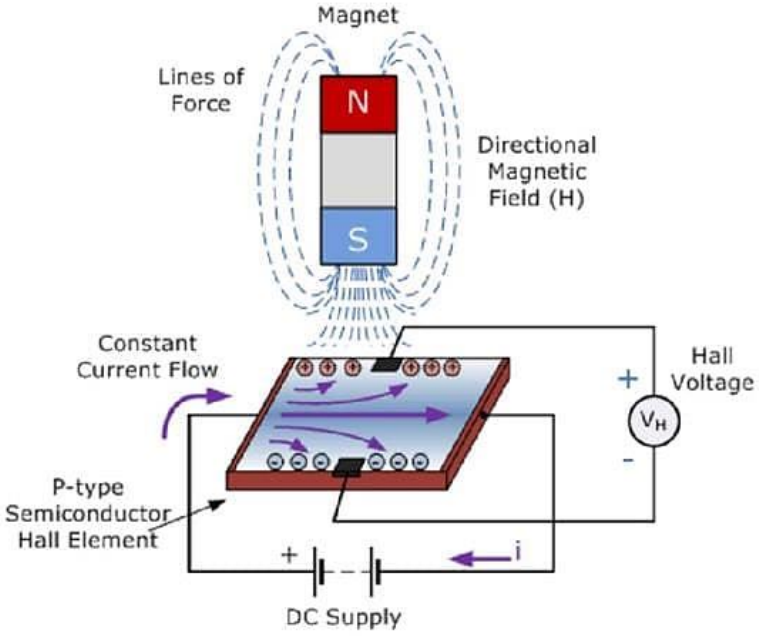

Figure 2.2: Hall effect schematic representation.

Image taken from: *https://static4.arrow.com/-/media/arrow/images/miscellaneous/0/0815-product-roundup-hall-effect-sensors-secondary-1.jpg?h=486&w=613?mw=290&hash=EDBA1D7951BDFDFCB204BAB8FB356BAFBA202EA3*

2.4. Van der Pauw Method

The Van der Pauw measurement method [14,15], named after its inventor Leo J. van der Pauw, is a widely used as a 4-point measurement for determining the sheet resistance and the Hall coefficient of materials.

In 1958 van der Pauw solved the general problem of potential distribution in a thin conductive layer of any shape and thus made it possible to carry out Hall and resistance measurements on them. However, some prerequisites must be met for a correct measurement. The thickness l of the sample must be homogeneous and small in relation to the distance between the contacts. It must consist of a continuous form in the mathematical sense and must therefore not have any holes or islands made of highly conductive material. The four contacts must be on the edge of the sample and small in relation to the area of the sample.

Van der Pauw proved that the mean resistivity of the sample is given by:

$$\rho = R_s l \tag{2.19}$$

where l is the sample thickness, and R_s can be obtained by the following equation:

$$e^{-\pi R_{12,34}/R_S} + e^{-\pi R_{23,41}/R_S} = 1 \tag{2.20}$$

In this direction, the measurement is made by introducing a current through one sample edge (see Fig. 2.3) to measure the voltage on the opposite side; with the current and voltage values is possible to compute the resistances $R_{12,34}$, and $R_{23,41}$:

$$R_{12,34} = \frac{V_{34}}{I_{12}} \tag{2.21}$$

Analogously, $R_{23,41}$ is computed. Eqs. (2.20) and (2.19) allow to find the resistivity.

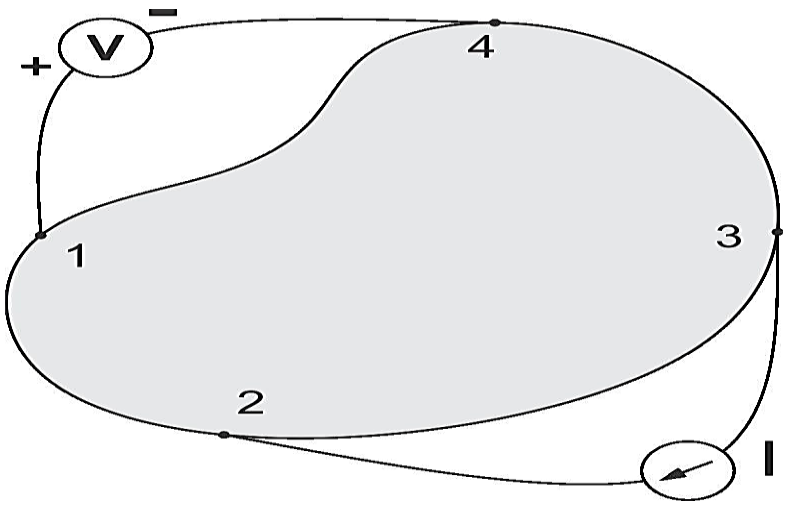

Figure 2.3: Van der Pauw method representation for an arbitrary shape sample.

2.5. Van der Pauw Method and Hall Effect

The aim of the Hall effect measurements by using the Van der Pauw method is determining the carrier density n_s, starting with the Hall voltage V_H measurements. A constant current I and a constant magnetic field B are used for the Hall voltage determination. In Fig. 2.4 is shown a square sample where the current is injected through 2-4 contacts while the Hall voltage $V_H = V_{13}$ is measured in the 1-3 contacts. The carrier density is obtained with the V_H measurement and knowing the I and B values:

$$n_s = \frac{IB}{q|V_H|} \tag{2.22}$$

q represents the carrier charge.

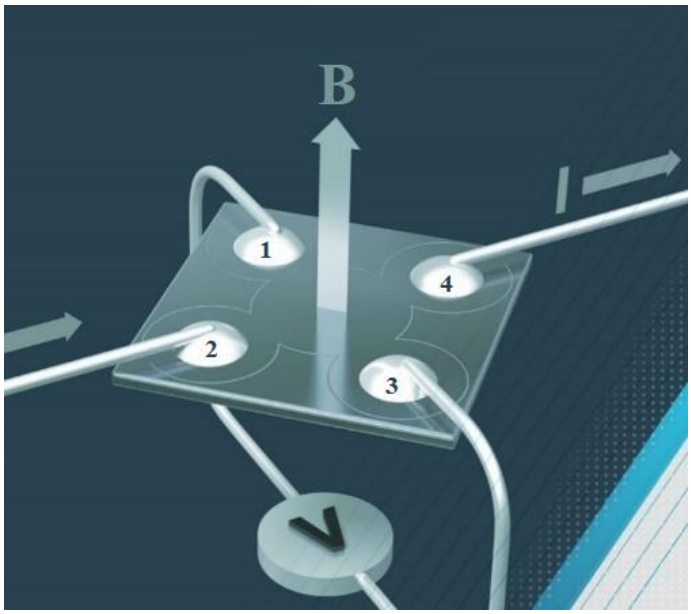

Figure 2.4: Schematic representation of the Hall voltage measurement when the current is injected for the 2-4 contacts (I_{24}), and the Hall voltage measured in the 1-3 contacts (V_{13}). The magnetic field is in positive orientation.

Image adapted from: *https://www.linseis.com/wp-content/uploads/2020/07/sample-configuration-Hall-coefficient-measurement-using-Van-der-Pauw-technology.jpg*

For the sample type (n or p) determination, and the carrier density calculation of a more accurate way, eight measurements are usually done: four with the magnetic field in one orientation (positive), and four with the magnetic field in the contrary orientation (negative). In each measurement respective voltages are measured as is indicated in Fig. 2.5, in order to guarantee the sample homogeneity which is a Van der Pauw method requirement.

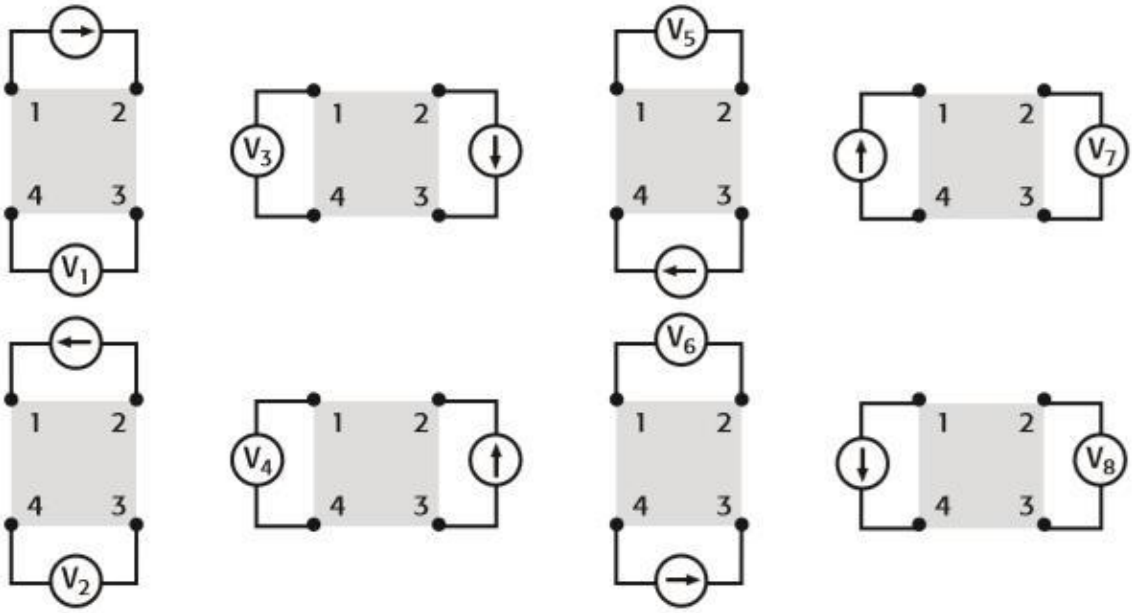

Figure 2.5: Methodology to take the eight Hall voltage measurements by using the Van der Pauw method.

Image taken from: *https://docplayer.es/docs-images/69/60826094/images/59-1.jpg*

CHAPTER 3

Thermal Properties in Semiconductors

Thermal property is understood as the response that exhibits materials to heat application. Temperature and dimensions increases due the energy absorption are examples of this. Some thermal properties present in solids are heat capacity, thermal conductivity, thermal diffusivity, and thermal effusivity.

The thermal and optical properties of crystalline Si have been studied by techniques base on photothermal phenomena, such as the photoacoustic technique. The photothermal phenomena are produced when a material absorbs and turns radiation into heat due to non-radiative deexcitation processes. The usual design of a measurement technique based on photothermal processes consists of a radiation source with a modulated beam, which is incident on a sample producing periodic temperature variations. The temperature in the material increases and decreases periodically, transferring heat from the sample to the nearest layer of gas. In the same way, the gas layer expands and contracts periodically over the gas producing an acoustic or pressure wave that can be detected with a microphone. The signal captured by the detector depends not only on the optical absorption coefficient and the efficiency of the sample to convert the absorbed radiation into heat but also on the ability of the material to diffuse the absorbed heat. The thermal diffusivity, α, of a material, is the ratio between the heat transported by conduction and the volumetric heat capacity. The thermal diffusivity can be measured, and the thermal conductivity κ can be calculated, which is directly related to the electrical conductivity. Thermal diffusivity measurement is of paramount importance in the semiconductor industry. Power dissipation in microelectronics and optoelectronic devices is an important mechanism limiting their performance. Therefore, the materials thermal diffusivity value used in these devices is a parameter to consider for their optimization [16].

3.1. Heat Capacity

Heat capacity is a property that indicates the "ability" of a material to absorb heat from a thermal source. Quantitatively, it represents the amount of energy required to increase the temperature in one unit. Mathematically the heat capacity C is expressed as:

$$C = \frac{dQ}{dT} \tag{3.1}$$

where dQ is the required energy to produce a temperature change dT. Usually, the heat capacity is specified for substance mole $[J/mol \cdot K]$, while the specific heat c is used to represent the heat capacity per mass unit $[J/kg \cdot K]$.

There are two ways to measure heat capacity: at constant pressure C_p and at constant volume C_V. Because thermal expansion in solids is small (compared to that occurring in gases), the heat capacity at constant volume is almost equal at constant pressure.

Some thermal properties come from diffusive phenomena where lattice vibrations and electron movement make the energy transport in heat form. This is the case of heat capacity; it has two contributions: vibrational heat capacity and electronic heat capacity.

3.1.1. Vibrational Heat Capacity

In most solids, the mechanism for absorbing thermal energy is by increasing the lattice vibrational energy. These vibrations are coordinated in such a way generating waves that travel through the solid. These waves, considered as elastic waves, have small wavelengths and high frequencies. The vibrational thermal energy for a material is quantized, and a quantum of thermal energy is called a phonon.

In internal energy terms, the specific heat to constant volume c_V can be written as:

$$c_V = \left(\frac{dU}{dT}\right)_V \tag{3.2}$$

The vibrational contribution to the internal energy is given by the product between a particular phonon energy $\hbar\omega_k(p)$ for the p branch, the phonon occupancy number, and the vibration modes in k-space. Mathematically is:

$$c_V = \frac{\partial}{\partial T}\sum_p \int \frac{V}{(2\pi)^3}\frac{\hbar\omega_k(p)}{e^{\hbar\omega(p)/\kappa_B T} - 1} \tag{3.3}$$

where the integral is taken for k-vectors of the first Brillouin zone.

The Eq. (3.3) can be written by using the general form for the vibrational density of states:

$$c_V = \frac{\partial}{\partial T}\sum_{k,p}\frac{\hbar\omega_k(p)}{e^{\hbar\omega(p)/\kappa_B T}-1} \tag{3.4}$$

For high temperatures, $\hbar\omega_k(p) \ll \kappa_B T$, the Eq. (3.4) sum can be expressed making $x = \hbar\omega_k(p) \ll \kappa_B T \ll 1$, which is expand as:

$$\frac{\hbar\omega_k(p)}{e^x-1} = \frac{\hbar\omega_k(p)}{x+\frac{x^2}{2}+\frac{x^3}{3}+\cdots} \approx \frac{\hbar\omega_k(p)}{x}\left(1-\frac{x}{2}+\frac{x}{12}\right) \tag{3.5}$$

Using the first expansion term of Eq. (3.5), the sum $\hbar\omega_k(p)/x$ over all k-vectors and p-branch converges to a constant value for the specific heat:

$$c_V = 3N_A\kappa_B = 3R \tag{3.6}$$

N_A represents the Avogadro number, κ_B corresponds to the Boltzmann constant, and R is the ideal gasses constant. This result was seen by Dulong and Petit, who obtained a c_V value approximated to $2.49 \times 10^4\ J/kmol \cdot K$ for different elemental solids [17].

3.1.2. Electronic Heat Capacity

There is also an electronic contribution to the heat capacity since it can be thermally exciting at higher energy levels. The electronic heat capacity added to the vibrational term fully expresses the heat capacity of a solid, i.e.:

$$C = C_{\text{phononic}} + C_{\text{electronic}} \tag{3.7}$$

In most cases, the electronic contribution is much smaller than the vibrational contribution. The electronic contribution occurs when electrons absorb thermal energy and increase their kinetic energy; however, this is only possible for free electrons. The free electrons present in the solid are considered a classical $N_{\text{particles}}$ gas, and the thermal energy acquired is merely translational. In the limit when $\kappa_B T \gg \Delta s$ (Dulong-Petit limit), where Δs is the energy between energy levels, the heat capacity is expected to be independent of temperature.

In metals, only electrons near the Fermi level have been excited from a full to an empty state participate, representing a small fraction of the total number of electrons. In a semiconductor or an insulator, only electrons that have been thermally excited from the valence band to the conduction band contribute to the electronic heat capacity. However, only a tiny portion of electrons can make this transition, resulting in negligible electronic contribution at room temperature [18].

3.2. Thermal Conductivity

Thermal conductivity is a physical property of materials that measures the "capability" to conduct heat. In other words, thermal conductivity is also the "ability" of a substance to transfer the kinetic energy of its molecules to adjacent molecules or to substances with which it is in contact. In metallic solids, heat, like electricity, is conducted by free electrons moving in the lattice. In all solids, heat is conducted by propagating vibrational energy of lattice. Thermal conductivity is an intensive quantity because it does not depend on the mass, and by dividing the portion of matter into small pieces, its properties are not additive.

Fourier's law allows quantify this property that for an isotropic (its properties do not change with direction) material is a scalar:

$$\kappa = -\frac{\dot{q}}{\vec{\nabla}T} \tag{3.8}$$

where $\dot{q}$ is the heat flux per time unit and length unit, and $\vec{\nabla}T$ is the temperature gradient established in two different system points.

In a solid material, heat conduction occurs through lattice vibrations propagating along the material (phonons) and the movement of free electrons. The thermal conductivity is associated with each of these mechanisms, and the total conductivity is the sum of both. The thermal energy associated with lattice vibrations is transported from areas of higher temperature to areas of lower temperature when there is a temperature gradient in the material as the second thermodynamics law predicts (see Fig. 3.1). Free electrons also participate in thermal conduction; they migrate from hot regions of the solid, where electrons gain kinetic energy, to cold areas where they transfer kinetic energy to the atoms due to collisions with phonons, other electrons, or material imperfections. The relative contribution of to the total thermal conductivity increases with the increase of free electrons in the material.

In highly pure metals, electron heat transport is much more efficient than the phonon contribution because there are many free electrons, and they are not easily scattered and have high velocities. Since the free electrons are moving in the material, not only will there be a heat flow, but also an electric current is generated. The relationship between these two parameters is stated in the Wiedemann-Franz law [17].

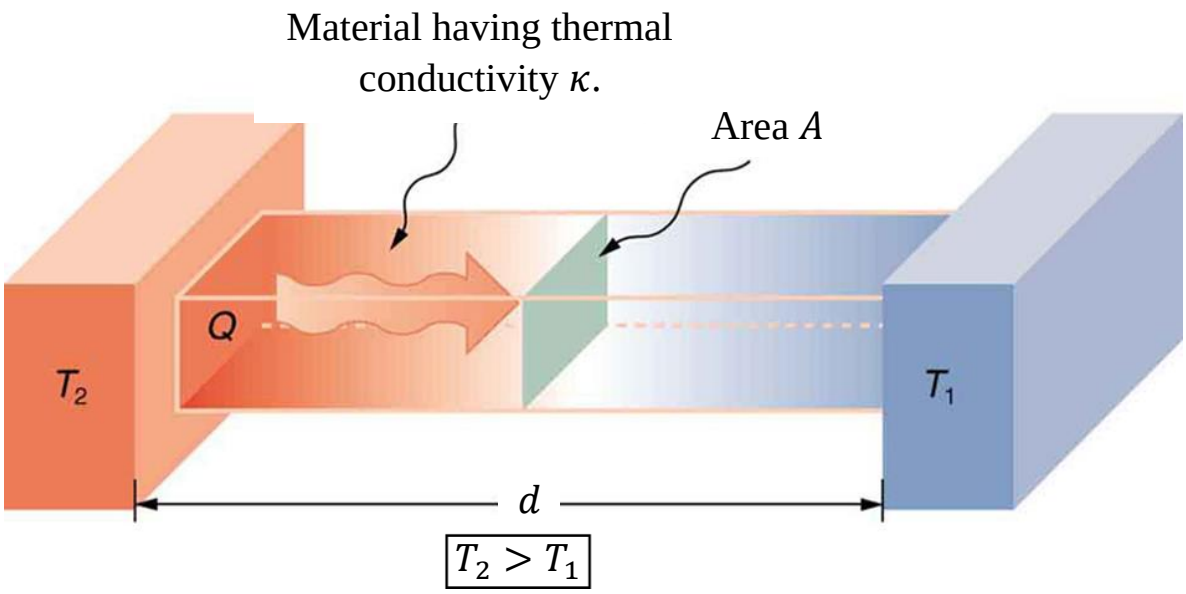

Figure 3.1: Schematic representation of heat conduction phenomenon accord to Fourier's law and the second thermodynamic law.

Image taken from: *https://cdn.kastatic.org/ka-perseus-images/ac67696eb6a0451324b5a0855ce6888d34155198.jpg*

On the other hand, from the kinetic theory of gases, the electronic contribution to the thermal conductivity of a system of independent particles can be known as follows:

$$\kappa_{\text{el}} = \frac{1}{3} c_{el} v l \tag{3.9}$$

c_{el} is the electronic specific heat per volume unit, v is the mean speed particles, and l is the mean free path. The formula basis is that heat is exchanged between particles only during collisions. It can be applied to independent electrons in metal with minor modifications because the exclusion principle is applied. The electronic specific heat is:

$$c_{\text{el}} = \frac{\pi^2 n \kappa_B{}^2 T}{2E_F} \tag{3.10}$$

E_F corresponds to the Fermi energy, and n is the electronic density. For the velocity v, the Fermi velocity will be used because only electrons near the Fermi energy can change their state (i.e., be scattered) and absorb or release energy. The mean free path of electrons at Fermi energy, which is $v_F \tau$, will be taken. Therefore, the electronic thermal conductivity can be written as:

$$\kappa_{\text{el}} = \frac{1}{3} \frac{\pi^2 n \kappa_B{}^2 T v_F{}^2 \tau}{2E_F} \tag{3.11}$$

Taking $E_F = m v_F{}^2/2$:

$$\kappa_{\text{el}} = \frac{\pi^2 n {\kappa_B}^2 \tau}{3m} T \tag{3.12}$$

In pure metals, the electronic contribution to thermal conductivity dominates over the contribution from lattice vibrations at all temperatures. In disordered alloys where the mean free path is greatly reduced, the electronic contribution is comparable to the contribution from lattice vibrations [13].

3.2.1. Wiedemann-Franz Law

Perhaps the most outstanding achievement of Drude free-electron theory was to explain the Wiedemann-Franz law. This empirical law states that the ratio of thermal conductivity to electrical conductivity is proportional to temperature. Furthermore, the proportionality constant, called Lorentz number, L, is independent of the type of metal. Using the equations for electrical conductivity σ and electronic thermal conductivity K_{el}, it follows that:

$$\frac{\kappa_{\text{el}}}{\sigma} = \frac{\frac{\pi^2 n {\kappa_B}^2 \tau T}{3m}}{\frac{n e^2 \tau}{m}} \tag{3.13}$$

$$\frac{\kappa_{\text{el}}}{\sigma} = \frac{\pi^2}{3}\left(\frac{\kappa_B}{e}\right)^2 T \tag{3.14}$$

$$\frac{\kappa_{\text{el}}}{\sigma} = LT \tag{3.15}$$

where:

$$L = \frac{\pi^2}{3}\left(\frac{\kappa_B}{e}\right)^2 = 2.45 \times 10^{-8} \frac{W\Omega}{K^2} \tag{3.16}$$

is the Lorenz number. The experimental Lorenz numbers for elementary metals vary between 2.30×10^{-8} and $3.20\times10^{-8}\ W\Omega/K^2$ for temperatures between 0 and $100°C$. It is to be considered that in the equation derived for the Wiedemann-Franz law, it was assumed the same collision times for the electrical and thermal conductivities. This assumption does not hold at low temperatures, and the Lorenz number for pure copper near 15 K is an order of magnitude smaller than the Lorenz number at room temperature [13].

3.1. Thermal Diffusivity

The quantity that measures temperature change produced in a material volume unit due to a heat amount flowing throughout a cross-section unit and in a time unit, when a temperature gradient setting, is called thermal diffusivity. The thermal diffusivity physical meaning is related to the rate of heat propagation during temperature changes over time [19].

In the heat transfer analysis, the ratio of the thermal conductivity of the volumetric heat capacity, defining mathematically the thermal diffusivity:

$$\alpha = \frac{\kappa}{\rho C} \tag{3.17}$$

ρ represents the material density, and α has cm^2/s units. High thermal diffusivity materials heat or cool quickly, while low thermal diffusivity materials heat or cool slowly. When it comes to unsteady-state heat transport, thermal diffusivity is a crucial property to consider. Thermal diffusivities can be calculated experimentally or by determining κ and ρC separately.

CHAPTER 4

Structural Properties in Semiconductors

Solids are classified in various ways, but crystalline and amorphous solids are likely the most common in materials science. A regular repeating arrangement of atoms is characterized by a repeat unit known as the unit cell in crystalline solids. Amorphous solids do not have this regular repeating structure. Many solids are wrongly classified as amorphous, yet they are microcrystalline or nanocrystalline, with minuscule crystallite sizes that fail to produce crystalline X-ray diffraction patterns. However, electron diffraction can often prove the crystalline nature of these materials, with lattice pictures routinely generated from particles in the 5 nm range.

A semiconductor is often described as a material with an electrical resistivity between 10^{-2} and 10^{9} Ω·cm. It can also be characterized as a material with an energy gap for electronic excitations of 0 to 4 electron volts (eV) approximately. Metals and semimetals have zero bandgaps, whereas insulators have energy gaps greater than 3 eV. There are certain exceptions to these conventions. Two cases are semiconducting diamond (energy gap of roughly 6 eV) and semi-insulating GaAs (energy gap of 1.5 eV), commonly used. GaN is gaining popularity as an optoelectronic material in the blue region with a 3.5 eV gap. Silicon is, without a doubt, the most well-known semiconductor. Aside from silicon, there are numerous other semiconductors. Many minerals found in nature are semiconductors, including zinc-blende (ZnS), cuprite (Cu_2O), and galena (PbS), to mention a few. Semiconductors are one of the most versatile materials known to man including laboratory-made semiconductors. Semiconductors are found in a wide range of chemical compositions and crystal structures. They can be elemental semiconductors like silicon (Si), carbon (C60) or nanotubes, and selenium (Se), or binary compounds like gallium arsenide (GaAs). Many organic molecules are semiconductors, such as polyacetylene $(CH)_n$. Magnetic or ferroelectric phenomena may be found in several semiconductors [12].

4.1. Elemental Semiconductors

Elements like silicon (Si), germanium (Ge), and tin (Sn) in group IV, and selenium (Se), and tellurium (Te) in group VI of the periodic table, are elemental semiconductors conformed by single species of atoms. Si is, of course, the most well-known semiconductor. Its crystal structure is alike of germanium (Ge), and it is the prototype of a broad family of semiconductors. Si and Ge crystal structures are the same as diamond (see Fig. 4.1) and α-tin (a zero-gap semiconductor commonly known as "gray" tin). Each atom in this configuration is surrounded by four nearest-neighbor atoms, producing a tetrahedron (each atom is said to be four-fold coordinated).

The electronics industry foundation and the cornerstone of current technology are these tetrahedrally bonded semiconductors. Semiconductors include elements from the periodic table groups V and VI, such as phosphorus (P), sulfur (S), selenium (Se), and tellurium (Te). Three-fold (P), two-fold (S, Se, Te), or four-fold coordinated atoms can be found in these crystals. These elements may exist in a variety of crystal forms and can also be used to make glass. Se, for example, has been produced as glass or with monoclinic and trigonal crystal forms (which can also be considered a polymer).

The bandgap in an elemental semiconductor gives emission in the infrared range rather than the visible range; hence, elemental semiconductors cannot be utilized to create visible LEDs because the energy emitted by the holes-electrons recombination does not fall within the visible spectrum [12].

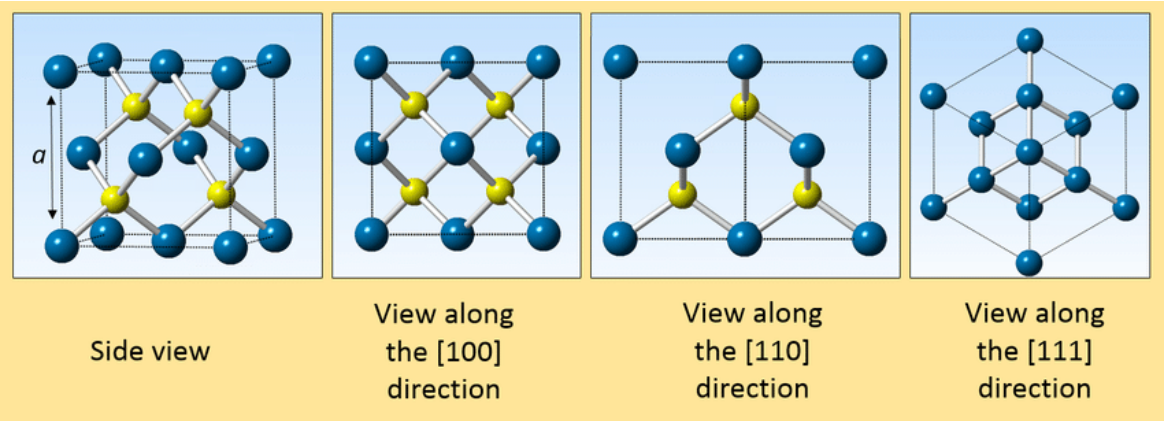

Figure 4.1: Schematic representation of face-centered cubic (fcc) diamond-type structure. The yellow spheres correspond to atoms surrounded by four near-neighbor atoms, which should not get confused with atoms of another element because it would be a Zinc-Blende structure.

Image taken from: *https://www.researchgate.net/profile/Julie-Tournet-2/publication/325870832/figure/fig5/AS:639520269672469@1529484922716/Schema-of-face-centered-cubic-a-and-Zinc-Blende-b-structures-The-diamond-cubic.png*

4.2. Binary Compound Semiconductors

The compound properties produced from periodic table elements in groups III and V (such as GaAs) are remarkably similar to those of their group IV equivalents. Due to electrical charge transfer from the group III atom to the group V atom, the bounding of the elements III-V compounds becomes partially ionic. Ionicity modifies the semiconductor properties significantly. It increases the Coulomb interactions between ions and the energy of the electronic band structure fundamental gap. In II-VI compounds like ZnS, the ionicity becomes considerably bigger. As a result, the bandgaps of most II-VI compound semiconductors are more than 1 eV. Compounds containing the heavy element mercury (Hg) are an exception. Mercury telluride (HgTe), like gray tin, is a zero-bandgap semiconductor (or semimetal). While large bandgap II-VI compound semiconductors may have applications in screens and lasers, smaller bandgap II-VI semiconductors are interesting materials for infrared detectors manufacturing. As a result of their high ionicity, the I–VII compounds (for example, CuCl) have large bandgaps (3 eV). Rather than being semiconductors, many of them are classified as insulators. Furthermore, the Coulomb interaction between the ions increases the cohesive energy of the crystal, favoring the rock-salt structure with six-fold coordinated atoms, as it is shown in Fig. 4.2b, instead of tetrahedral bonds. Semiconductors include binary compounds made up of group IV and VI elements, such as lead sulfide (PbS), PbTe, and tin sulfide (SnS). Six-fold coordinated ions are also favored by these high ionicity compounds. They have relatively narrow bandgaps despite their high ionicity, akin to mercury chalcogenides. These IV-VI semiconductors with small bandgaps are also useful as infrared detectors. For blue light-emitting diodes and lasers, GaN, a high bandgap III–V compound, as well as $GaIn_{1-x}N_x$ mixed crystals, are employed [12].

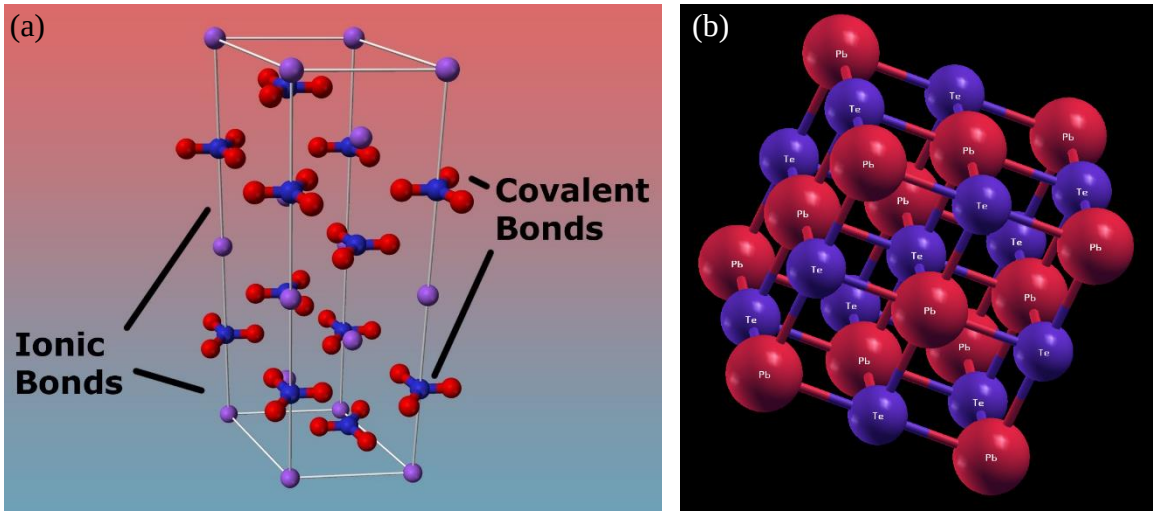

Figure 4.2: (a) A compound material structure exhibiting the covalent and ionic bond differences, and (b) PbTe crystal structure where is appreciated six-fold coordinated atoms.

Images respectively taken from: *https://sciencenotes.org/wp-content/uploads/2020/05/ionic-covalent-bonds.jpg, and https://lh3.googleusercontent.com/proxy/SUqe32yTe5CMes2_LuVlIiEvzZVtSB_JimozAd4dWwSozK_bVEy0d5cBe4VMQdVzDbrf5oW8mSwpAw6UHSbzOswcfnH8UrTxNKrt5Dy-UNgMdlxvS0WKPVilqA*

4.3. Bands and Bandgaps Origin

Single and isolated atom electrons occupy atomic orbitals, each with its discrete energy level. Their atomic orbitals overlap when two or more atoms come together to create a molecule. No two electrons in a molecule may have the same quantum number, according to the Pauli exclusion principle. When two identical atoms unite to produce a diatomic molecule, each atomic orbital splits into two molecular orbitals with different energies, allowing the electrons in the prior atomic orbitals to appears in the new orbital structure. At the same time, none of them have the same energy. By the analogous manner, when N identical atoms join together to create a solid, such as a crystal lattice, their atomic orbitals overlap. Because no two electrons in a solid have the same quantum number, each atomic orbital breaks up into N distinct molecular orbitals, each with a different energy. The number of atoms in a macroscopic solid ($N \sim 10^{22}$) is enormous; therefore, the number of orbitals is also very large. They are relatively tightly spaced in energy (on the order of 10^{-22} eV) due to the energy of neighboring levels is so close together, they may be thought of as a continuous energy band.

By the other hand, bandgaps are a residual range of energy not covered by any band due to the finite width energy bands. The bandwidths vary depending on the degree of overlap in the atomic orbitals from which they originate. It is possible that two neighboring bands are not wide enough to encompass the entire energy range.

Fig. 4.3 illustrates a hypothetical example for understanding the electronic bands formation. The energy levels as a function of crystal-cell size are shown on the right graph (a typical spacing between atoms). All N atoms have discrete valence orbitals p and s when they are far apart. When the atoms get near enough, their electron orbitals start to overlap spatially, and each atomic level divides into N levels with differing energies according to the Pauli exclusion principle. Because N is such a high number, neighboring levels are energetically near to one another, essentially forming a continuous energy band. The formed bands are known as valence and conduction bands are generated at the actual diamond crystal cell size (denoted by a) and are separated by a 5.5 eV bandgap. The band structure is further modified by reducing the inter-atomic gap even further (e.g., at high pressure).

An electronic band structure of a solid (or simply band structure) specifies the range of energy levels that electrons can have within it and the ranges of energy they cannot have (called band gaps or forbidden bands). These bands and band gaps are derived from band theory by studying the allowable quantum mechanical wave functions for an electron in a large periodic lattice of atoms or molecules. Band theory has been utilized properly to explain many physical properties of solids, including electrical resistivity and optical absorption, and it is the cornerstone of all-solid-state device (transistors, solar cells, etc.) knowledge.

Fig. 4.4 shows the electronic states fill at equilibrium of diverse materials. Height represents energy, whereas width is the density of possible states for given energy in the specific material. According to the Fermi–Dirac equation (black: all states filled, white: no state filled), the shade is distributed. The Fermi level EF is found inside at least one band in metals and semimetals [20].

The Fermi level is inside a bandgap in insulators and semiconductors. Still, the bands in semiconductors are close enough to the Fermi level to be thermally filled with electrons or holes.

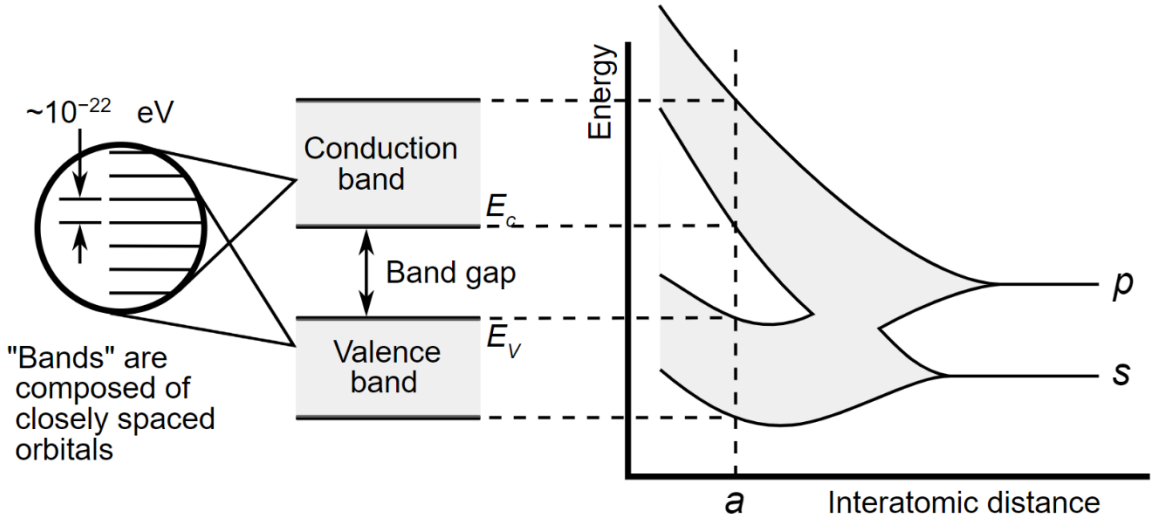

Figure 4.3: Hypothetical scenario in which a considerable number of carbon atoms are brought together to create a diamond crystal illustrating the development of the electronic band structure.

Image taken from:
https://upload.wikimedia.org/wikipedia/commons/thumb/e/ef/Solid_state_electronic_band_structure.svg/1920px-Solid_state_electronic_band_structure.svg.png

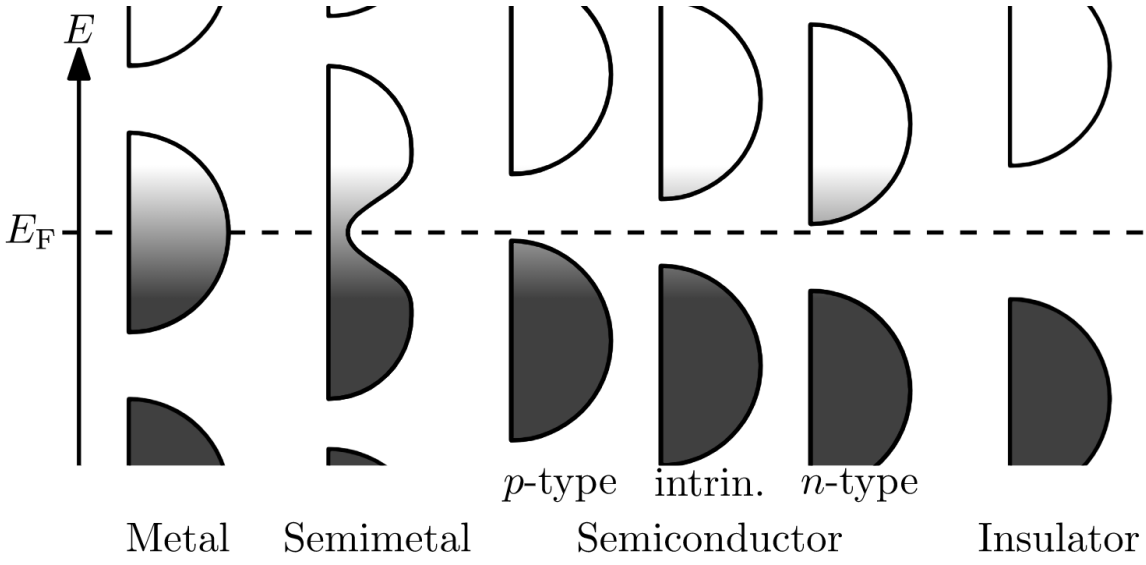

Figure 4.4: A metal, a semimetal, a semiconductor, and an insulator energy bands comparison.

Image taken from:
https://upload.wikimedia.org/wikipedia/commons/thumb/9/9d/Band_filling_diagram.svg/1920px-Band_filling_diagram.svg.png

4.3. Band Structures, Translational Symmetry (Bloch Theorem), and Brillouin Zones

Semiconductors differentiate from other materials in the electrons behavior, specifically by the gaps present in their electronic excitation spectra. The electronic band structure is the most convenient way to describe the microscopic electrons behavior in a material.

A perfect crystal can be described by the following Hamiltonian:

$$\hat{H} = \sum_i \frac{\hat{p}_i^{\,2}}{2m_i} + \sum_i \frac{\hat{P}_j^{\,2}}{2M_j} + \frac{1}{2}\sum_{j',j} \frac{Z_j Z_{j'} e^2}{4\pi\varepsilon_0 \left|\vec{R}_j - \vec{R}_{j'}\right|} - \sum_{j,i} \frac{Z_j e^2}{4\pi\varepsilon_0 \left|\vec{r}_i - \vec{R}_j\right|} + \frac{1}{2}\sum_{i,i'} \frac{e^2}{4\pi\varepsilon_0 |\vec{r}_i - \vec{r}_{i'}|} \tag{4.1}$$

Eq. (4.1) is written in the CGS units system. $\vec{r}_i$ corresponds to the ith electron position, $\vec{R}_j$ represents the jth nucleus position, Z_j is the nucleus atomic number, $\hat{p}_i$ and $\hat{P}_j$ are the momentum operators of the electrons and nuclei, respectively, ε_0 is the vacuum permittivity, and e is the electron charge. In the third and fifth terms of Eq. (1), the summation is done for $j' \neq j$ and $i \neq i'$.

The many-particle Hamiltonian in Eq. (2.1) obviously cannot be solved without a significant number of simplifications. The first approach is to divide electrons into two groups: valence and core electrons. The electrons in the filled orbitals are the core electrons. In the case of Si, the core electrons are those in the filled orbitals, such as the $1s^2$, $2s^2$, and $2p^6$ electrons. Since these core electrons are primarily localized around the nuclei, they can be "lumped" together with the nuclei to create ion cores. As a result of this approximation, the indices j and j' in Eq. (2.1) will now designate the ion cores, but the electron indices i and i' will only mark the valence electrons. These are electrons in partially filled shells, including the 3s and 3p electrons in the case of Si.

The Born–Oppenheimer or adiabatic approximation is the next approximation employed. Ions move considerably slower than electrons because they are much heavier. Ionic vibrations in materials generally have frequencies smaller than 10^{13} s^{-1}. To determine the electron response time, consider that the energy required to excite electrons in a semiconductor is given by its basic bandgap, which is typical of the order of 1 eV in most semiconductors. Hence, the electronic motion frequencies in semiconductors are on the order of 10^{15} s^{-1}. Electrons may respond to ionic motion extremely instantly, or, to put it another way, the ions are practically immobile to the electrons. On the other hand, ions are unable to track electron mobility and instead observe only a time-averaged adiabatic electronic potential. The Hamiltonian given in Eq. (2.1) takes the three terms sum form by using the Born-Oppenheimer approximation:

$$\hat{H} = \hat{H}_{\text{ions}}\left(\vec{R}_j\right) + \hat{H}_{\text{e}}\left(\vec{r}_i, \vec{R}_{j0}\right) + \hat{H}_{\text{e-ion}}\left(\vec{r}_i, \delta\vec{R}_j\right) \tag{4.2}$$

where $\widehat{H}_{\text{ions}}(\vec{R}_j)$ is the Hamiltonian defining ionic motion in the presence of ionic potentials as well as time-averaged adiabatic electronic potentials. $\widehat{H}_{\text{e}}(\vec{r}_i, \vec{R}_{j0})$ is the electrons Hamiltonian with ions fixed in their equilibrium positions $\vec{R}_{j0}$, and $\widehat{H}_{\text{e-ion}}(\vec{r}_i, \delta\vec{R}_j)$ corresponds to the electronic energy change due to the ions equilibrium position displacements, $\delta\vec{R}_j$. $\widehat{H}_{\text{e-ion}}(\vec{r}_i, \delta\vec{R}_j)$ is responsible for electrical resistance in reasonably pure semiconductors at room temperature and is known as the electron-phonon interaction.

The electronic Hamiltonian $\widehat{H}_{\text{e}}$ has the form:

$$\widehat{H} = \sum_i \frac{\hat{p}_i^{\,2}}{2m_i} + \frac{1}{2}\sum_{i,i'} \frac{e^2}{4\pi\varepsilon_0|\vec{r}_i - \vec{r}_{i'}|} - \sum_{i,j} \frac{Z_j e^2}{4\pi\varepsilon_0|\vec{r}_i - \vec{R}_j|} \tag{4.3}$$

Because a semiconductor has 10^{23} electrons/cm^3, diagonalizing this Hamiltonian is a difficult task. For that reason, it is will use a new approximation called the mean-field approximation, which is a pretty severe approximation assuming the same average potential $V(\vec{r})$ for each electron. The electron motions can be described by the Schrödinger equation as follows:

$$\widehat{H}_{1\text{e}}\psi_n(\vec{r}) = \left[\frac{\hat{p}^2}{2m} + V(\vec{r})\right]\psi_n(\vec{r}) = E_n\psi_n(\vec{r}) \tag{4.4}$$

$\widehat{H}_{1\text{e}}$ is the one-electron Hamiltonian, $\psi_n(\vec{r})$ and E_n corresponds to the wavefunction and energy of an electron in an n-eigenstate, respectively. It is important to note that each eigenstate can only hold two electrons with opposite spins (Pauli's exclusion principle).

There are two processes to calculating the electronic energies E_n. The determination of the one-electron potential $V(\vec{r})$ is the initial stage. $V(\vec{r})$ may be computed from first-principles using only the atomic numbers and positions as input parameters. The potential is represented in terms of parameters obtained by fitting experimental data in more straightforward, so-called semi-empirical techniques. After determining the potential, a complex computation must be completed to solve Eq. (4.4). To make this computation easier, the symmetry of the crystal is frequently used. By "symmetry," it implies geometrical alterations that do not modify the crystal shape.

The invariance of a crystal under particular translations is its most significant symmetry. Most crystals include rotational and reflection symmetry in addition to translational symmetry. Most semiconductors, it turns out, have high degrees of rotational symmetry, which helps to simplify the process of determining their energy band structures.

The called Bloch functions can be used to represent the wavefunctions of a particle moving in a periodic potential. It is will suppose Eq. (4.4) is one-dimensional and $V(x)$ is a periodic function with a translational period equal to R, this to understand what Bloch functions are. A translation operator T_R will be defined as an operator whose effect on any function $f(x)$ is specified by:

$$T_R f(x) = f(x + R) \tag{4.5}$$

A new function $\psi_k(x)$ is introduced and is defined by:

$$\psi_k(x) = e^{ikx}u_k(x) \tag{4.6}$$

where $u_k(x)$ has the same periodicity of V being a periodic function, which is $u_k(x + nR) = u_k(x)$ for all integers n. $\psi_k(x)$ with this form, multiplied by $e^{-i\omega t}$ represents a plane wave with modulated amplitude by the periodic function $u_k(x)$. $\psi_k(x)$ is known as a Bloch function. In the x to $x + R$ changes, by definition, $\psi_k(x)$ changes as follows:

$$T_R\psi_k(x) = \psi_k(x + R) = e^{ikR}\psi_k(x) \tag{4.7}$$

$\psi_k(x)$ is an eigenfunction of T_R as indicates in Eq. (2.7), with eigenvalue e^{ikR}. By the other hand, the Hamiltonian $\hat{H}_{1e}$ is invariant under R translation, thus, $\hat{H}_{1e}$ commutes with T_R, i.e., the $\hat{H}_{1e}$ eigenfunctions can be written as T_R eigenfunctions, thereby, an eigenfunction $\psi(x)$ of $\hat{H}_{1e}$ is expressed as a Bloch functions sum:

$$\psi(x) = \sum_k A_k\psi_k(x) = \sum_k A_k e^{ikx}u_k(x) \tag{4.8}$$

where A_k are constants. k constants index the one-electron wavefunctions being the plane waves vectors establishing the Bloch functions origin. The crystal electronic band structure is a plot of the electron energies in Eq. (4.4) as a function of k.

The extended zone scheme is a band structure plot in which k can take whatever possible value. The choice of k in a wave function indexing is not unique, as shown in Eq. (4.6). k and $k + 2n\pi/R$ will satisfy Eq. (4.6) with n an integer, which is a crystal translation symmetry consequence. In this way, k can be replace by $k' = k - 2n\pi/R$ where n is chosen to the $[-\pi/R,\ \pi/R]$ interval for k' limit. The defined $[-\pi/R,\ \pi/R]$ k-space region is called first Brillouin zone. When k is restricted to the first Brillouin zone, the band structure plot is known as the reduced zone scheme.

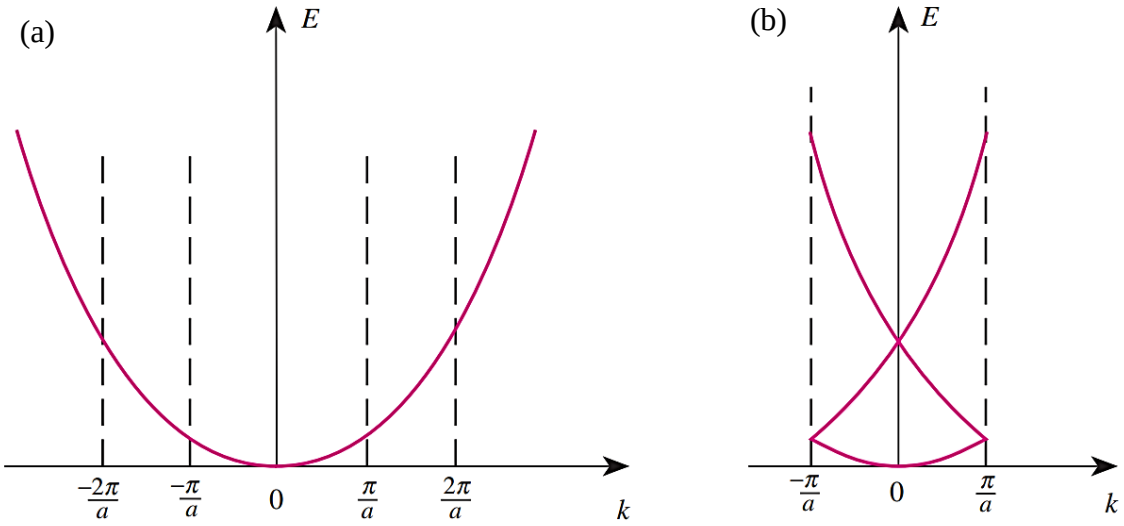

Figure 4.5: Free particle band structure in (a) the extended zone scheme and (b) the reduced zone scheme.

Image taken from: Ref. [12].

The "nearly free" ($V \to 0$) electron band structure moving in a one-dimensional lattice with the lattice constant a is illustrated in both schemes in Fig. 2.1. In the reduced zone scheme, band structures are displayed more compactly. Furthermore, in the reduced zone scheme, when electrons move from one state to another under the influence of a translationally invariant operator, k is preserved, while k is conserved in the extended zone scheme only to $2\pi/R$ multiple. In the literature, the reduced zone scheme is commonly used [20].

4.3.1. Linear Combination of Atomic Orbitals (LCAO) or Tight-Binding Approach for the Semiconductors Band Structure

Linear combinations of the atomic wave functions to approximate the electronic wave functions in the solid will used. The Linear Combination of Atomic Orbitals (LCAO) method is also called tight-binding approximation. This method gives a good approximation for understanding the electronic properties due to the semiconductor covalent bonds nature because it has two kinds of electronic states. Considering that the valence electrons are localized primarily on bonds, they keep more their atomic nature. Bonding orbitals in molecules should be highly comparable to the valence electron wave functions. The LCAO method has the benefit of allowing the band structure to be described in terms of a minimal number of overlap parameters and providing a good approximation for estimating the valence band structure.

To demonstrate the tight-binding method to computing band structures, it will stick to tetrahedrally bound semiconductors. These semiconductors valence electrons are located in the *s* and *p* orbitals. In Figs. 4.6a, 4.6b, and 4.6c, two identical and isolated atoms are shown schematically on the left sides, on the right sides are shown the atomic orbitals when two atoms are brought together in the x-direction until there is an overlap to create a diatomic molecule. Two new orbitals are formed when the two atomic orbitals interact. The bonding orbital is symmetric with regard to the exchange of the two atoms, while the antibonding orbital is antisymmetric. *p* orbitals can overlap in two ways. They are said to form bonds when they overlap in the *p* orbital direction (see Fig. 4.6b) forming σ bonds. In the case when the overlap is in a perpendicular direction to the p orbitals, π bonds are formed (see Fig. 4.6c).

The energy of the atomic orbitals is changed by their interaction. The interaction Hamiltonian $\hat{H}$ determines how much the antibonding orbital energy is enhanced in most cases. The bonding orbitals energy is reduced by the same amount. Fig. 4.7a illustrates the changes in orbital energy for a homopolar molecule, and Fig. 4.7b illustrates the changes in orbital energies for a heteropolar molecule. V is the overlap parameter in both situations since it is the matrix element of the interaction Hamiltonian between the atomic orbitals. There are four nonzero overlap parameters for a homopolar molecule with just s and p valence electrons. It shall designate the atomic orbital on one of the atoms as $|\alpha\rangle$ and the atomic orbital on the second atom as $|\beta\rangle$ to obtain this result.

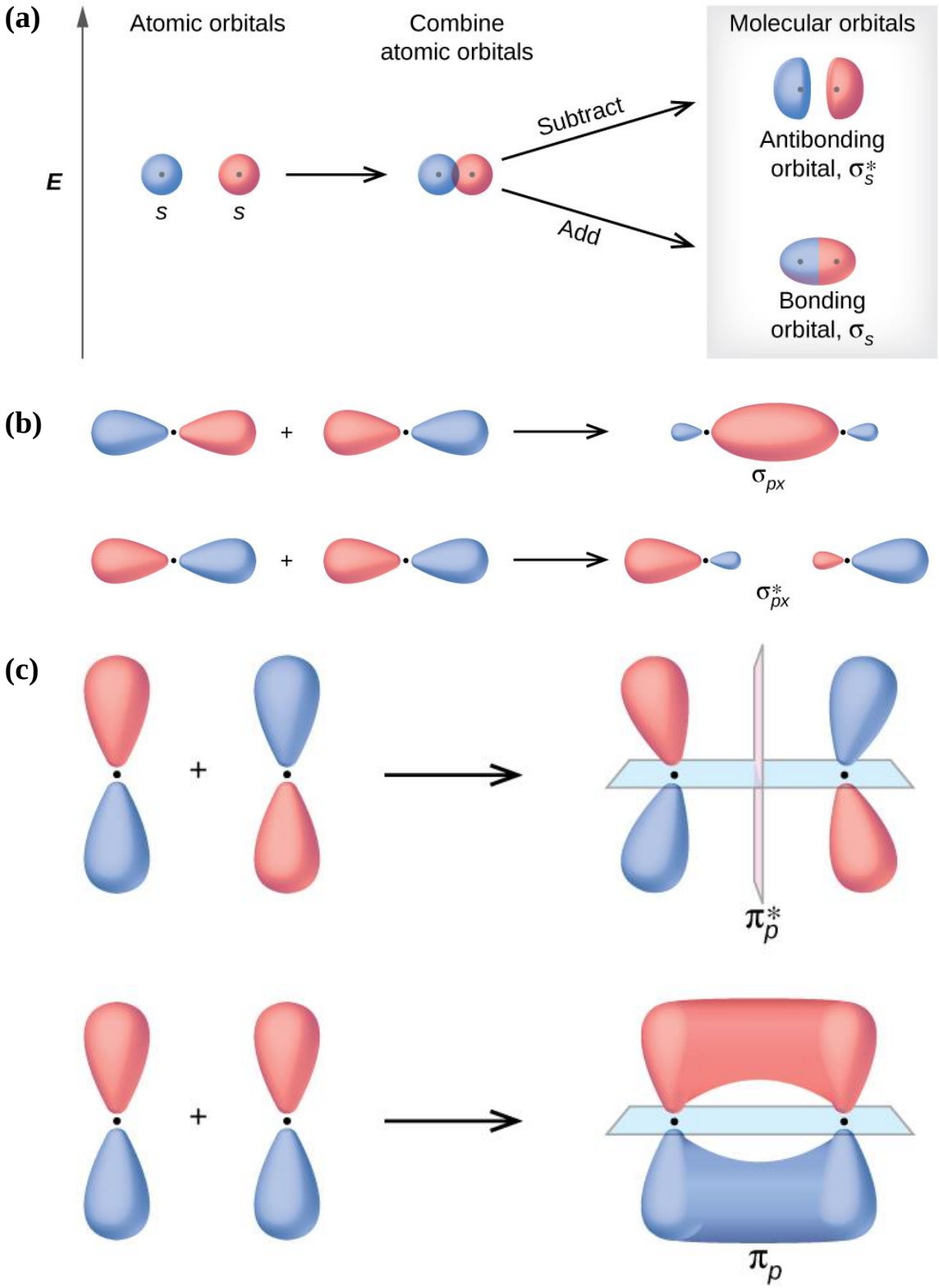

Figure 4.6: (a) Bonding and antibonding molecular orbitals formed by the combination of two s atomic orbitals, (b) p atomic orbitals wave functions combining along the internuclear axis creates two molecular orbitals, and (c) π molecular orbitals formation due to side-by-side overlap of each two orbitals.

Images taken from: *https://opentextbc.ca/chemistry/chapter/8-4-molecular-orbital-theory/*

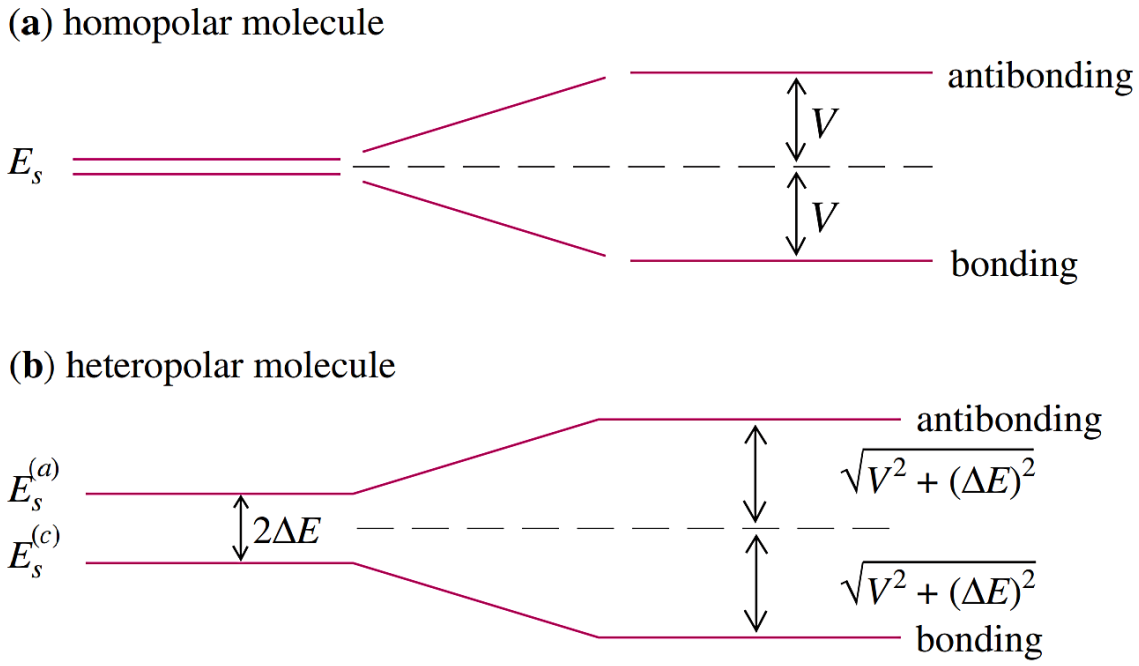

Figure 4.7: Orbital overlap effect on the energy levels in (a) a diatomic homopolar molecule, and (b) a diatomic heteropolar molecule. V corresponds to the interaction Hamiltonian matrix element.

Images taken from: Ref. [12].

In order to express theses orbitals as a product between a radial wave function and a spherical harmonic $Y_{lm}(\theta, \phi)$ with the atom located in the origin. It suggests the using of spherical coordinate system where the Hamiltonian $\hat{H}$ is independent of ϕ. Hence, the matrix element $\langle \alpha | \hat{H} | \beta \rangle$ is proportional to the azimuthal wave functions integral $e^{i(m-m')\phi}$. When $m = m'$, the integral does not vanish. This selection rule allows seeing four nonzero overlap parameters linearly independent for the *s* and *p* electrons. The overlap parameters are following:

$$\langle s|\hat{H}|s\rangle = V_{ss\sigma}; \quad \langle s|\hat{H}|p_z\rangle = V_{sp\sigma}; \quad \langle p_z|\hat{H}|p_z\rangle = V_{pp\sigma}; \quad \langle p_x|\hat{H}|p_x\rangle = V_{pp\pi} \qquad (4.9)$$

Considering as a symmetry result $\langle p_x|\hat{H}|p_y\rangle = 0$ and $\langle p_y|\hat{H}|p_y\rangle = \langle p_x|\hat{H}|p_x\rangle$. σ, π and δ are used for labeling the overlap parameters with $l = 2$ wave functions, depending if m is 0, 1 or 2 corresponding to *s*, *p*, and *d* atomic wave functions, respectively.

If the orbitals of each atom in the crystal overlap only with those of its nearest neighbors, the notion of bonding and antibonding orbitals developed for molecules may be applied to crystals. For most solids, this is a fair approximation. The bonding and antibonding orbitals in a solid are expanded into bands as a result of orbital overlap. Those that are filled with electrons create valence bands, whereas those that are empty form conduction bands. In a tetrahedral semiconductor, the *s* and *p* orbitals develop into bands, as seen in Fig. 4.8. The valence bands are formed when the bonding orbitals are filled with electrons, whereas the conduction bands are formed by the antibonding orbitals [13,21].

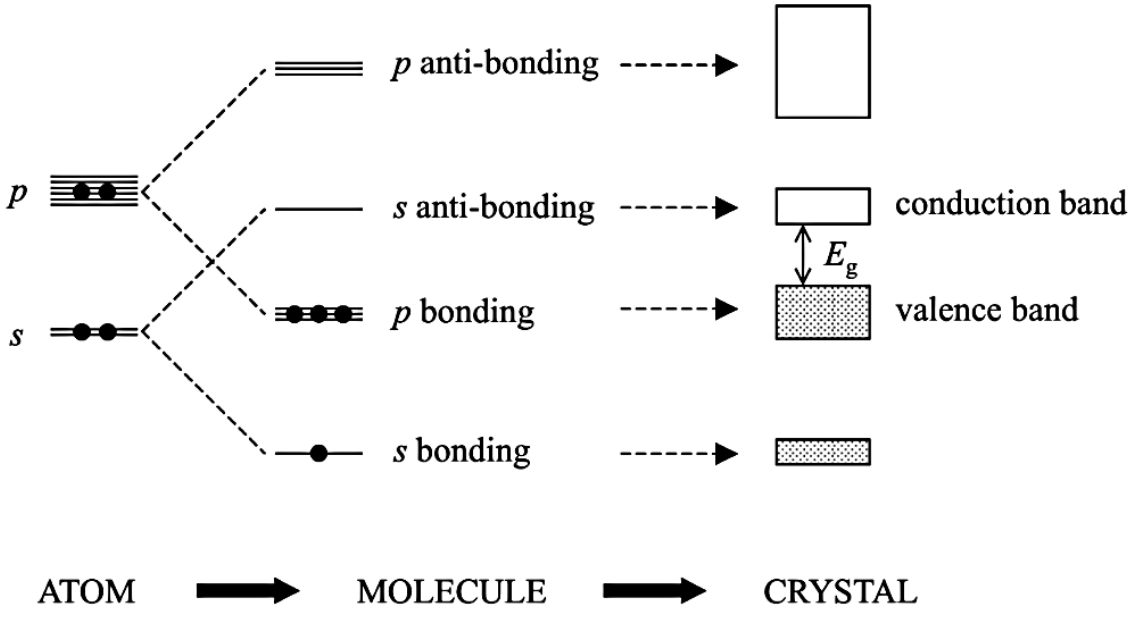

Figure 4.8: Development of atomic *s* and *p* orbitals into valence and conduction bands for a semiconductor. E_g corresponds to the gap energy.

Image taken from: Ref. [21].

4.3.2. Overlap Parameters and Nearest-Neighbor Distances

The following simple reasoning may predict a connection between the overlap parameters and the interatomic distance. The atomic energy levels widen into bands owing to atomic orbital overlap, as seen in Figs. 4.7 and 4.8. The bandwidths is basically $2V$, with V being the appropriate overlap parameter. As a result of this overlap, the electron wave functions become delocalized across a distance equal to the nearest-neighbor separation (i.e., the bond length) d. The delocalized electrons momentum is calculated to be $\hbar^2\pi^2/d$ using the uncertainty principle; therefore, the electron kinetic energy is $\hbar^2\pi^2/2md^2$. As a result, the overlap parameters appear to be dependent on d as d^{-2}. By comparing the band structures estimated by the tight-binding method with the nearly free electron model, this basic heuristic argument may be made more robust. Consider the lowest energy valence band in a crystal with a simple cubic structure as an example. The bonding *s* orbitals may be used to identify this band, and its dispersion in the [100] direction can be calculated resulting $E_s - 4V_{ss\sigma} - 2V_{ss\sigma}\cos(kx)$, $4V_{ss\sigma}$ is the bandwidth of this band, and the bandwidth gives by the nearly free electron model is $\hbar^2\pi^2/2md^2$. These two bandwidths can be equating:

$$4V_{ss\sigma} = \frac{\hbar^2\pi^2}{2md^2} \tag{4.10}$$

In this sense, for the *s* and *p* orbitals, the four overlap parameters are:

$$V_{ll'm} = \tau_{ll'm}\frac{\hbar^2}{md^2} \tag{4.11}$$

the crystal symmetry determines the factor $\tau_{ll'm}$; Eq. (4.10) gives $\tau_{ss\sigma} = \pi^2/8$ for a simple cubic crystalline structure. In fitting Si and Ge energy bands, it has considered the factors $\tau_{ll'm}$ as changeable parameters for diamond and zinc-blende crystals. For three of the parameters, it was found good agreement between the calculated and adjusted values. The exception is $\tau_{pp\pi}$, where the fitted value was -0.81 and it is slightly lower than the calculated value. The conduction and valence bands symmetry in the Brillouin zone center of the three group-IV elements Si, Ge, and gray tin (or α-Sn) may be understood qualitatively. Si has a higher lattice constant than α-Sn decreasing the overlap parameters $|V_{ss}|$ and $|V_{xx}|$; $|V_{ss}|$ is larger than for $|V_{xx}|$. Fig. 4.9 shows the changes in the ordering of *s* and *p* orbitals from Si to α-Sn. By filling the bands with the eight available valence electrons locates the Fermi level. As can be observed, the lowest conduction band in Si at the zone center is p-like, whereas the equivalent band in Ge is s-like. Fig. 4.9c shows the lower band energies for α-Sn due to *s* orbitals [13].

4.4. Indirect and Direct Semiconductors

As seen in previous sections, the valence band of a semiconductor is fill, whereas the conduction band is empty. Thermal excitation or optical absorption can both excite electrons from the valence band into the conduction band. The energy is released as heat or photons when the electron returns to the valence band. In the absence of defects, photons (electromagnetic radiation) are the primary mechanism for energy release in direct bandgap semiconductors, whereas phonons are the dominating mechanism in indirect bandgap semiconductors (heat). Optoelectronic devices like LEDs and lasers are manufactured with direct bandgap semiconductors.

The band structure of direct and indirect bandgap semiconductors is what distinguishes them. Electrons exhibit a wave-like character. A wave vector $\vec{k}$ is used to describe an electron wave. Thus, E vs. $\vec{k}$ graphs may be plotted for crystalline materials. These are similar to the simple band diagrams that depict the valence and conduction bands. Fig. 4.10a shows a partial band structure for Si. At absolute zero, all energy levels below it are full, and the 0 eV refers to the valence band top, denoted as Γ point. The line marked with the arrows has a minimum at X point representing the conduction band bottom, empty at 0 K. In this sense, the valence band maximum and the conduction band minimum do not match at $\vec{k} = 0$ (Γ point), fact that makes Si an indirect bandgap semiconductor. The same analysis is applicable for Ge (See Fig. 4.10b). It is necessary a crystal momentum change for a direct transition occurring in an indirect bandgap semiconductor. Because the curves are parabolic, a direct transition from the valence band into the conduction band of an electron needs a photon with a greater energy than the bandgap. However, making the shift at lower energy is doable, but the transition will need a phonon [22].

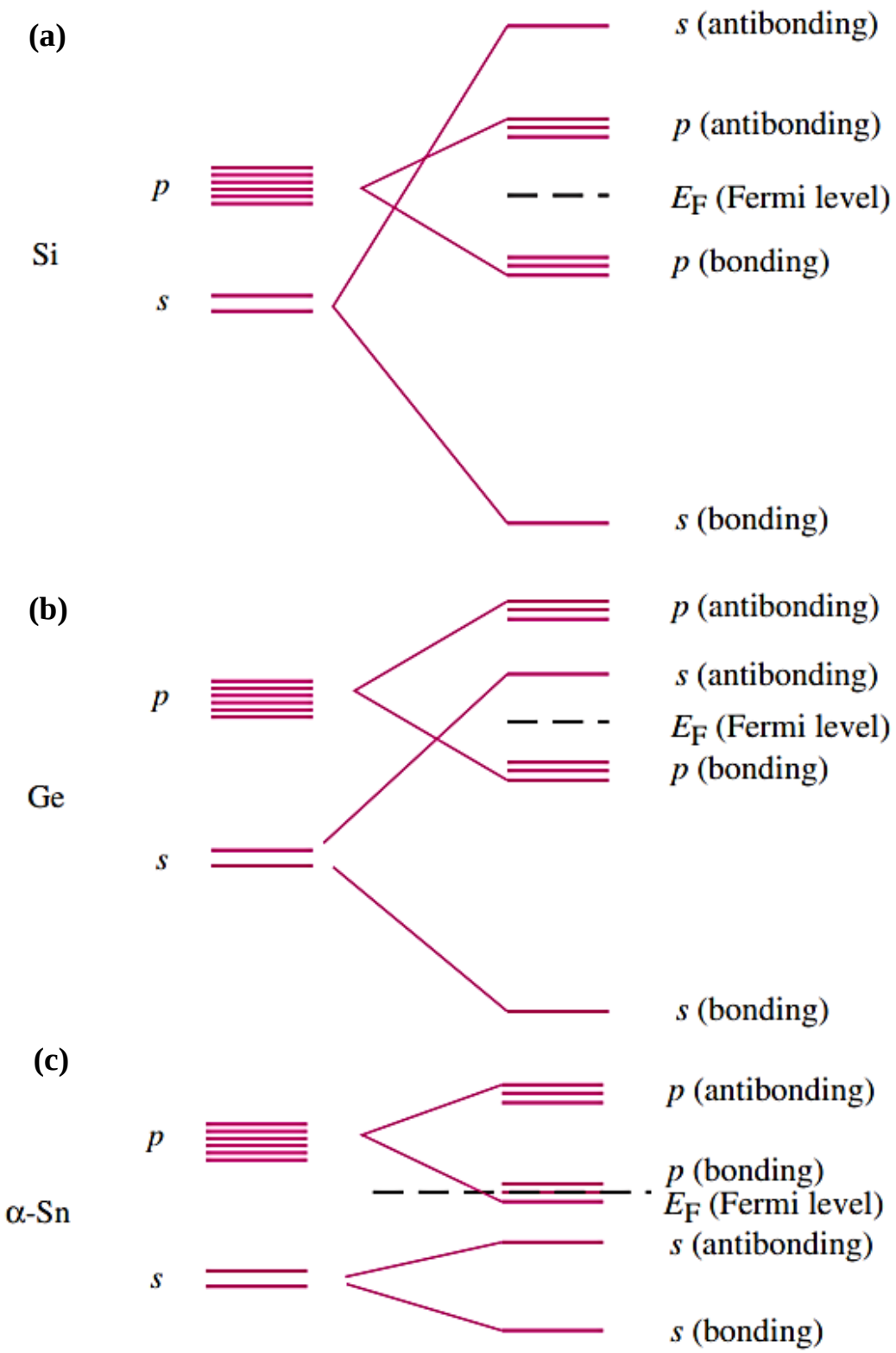

Figure 4.9: Development of atomic *s* and *p* orbitals into valence and conduction bands for (a) Si, (b) Ge, and (c) α-Sn. E_F is the Fermi level.

Image taken from: Ref. [12].

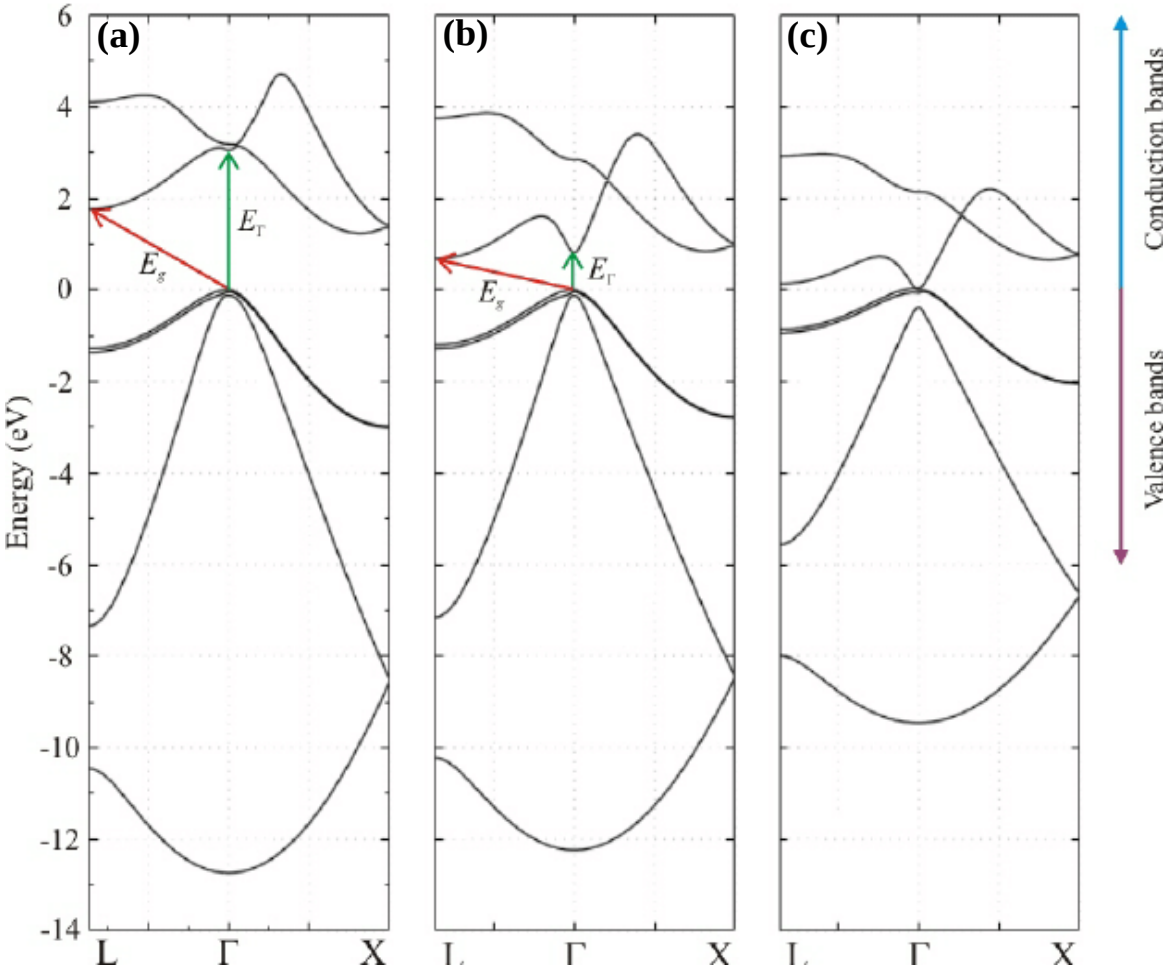

Figure 4.10: Electronic and structures for (a) Si, (b) Ge, and (c) α-Sn. E_F is the Fermi level. E_g and E_Γ are the gap energy and the gap energy at Γ point, i.e., when $\vec{k} = 0$, respectively.

Image taken from: *https://www.researchgate.net/profile/Filipe-Oliveira-25/publication/287201711/figure/fig2/AS:307674475450369@1450366719905/Electronic-band-structure-for-Si-Ge-and-a-Sn-Eg-and-E-G-are-the-energy-gap-and-the.png*

On the other hand, in a direct bandgap semiconductor, the valence band maximum matches the conduction band minimum at $\vec{k} = 0$. In Fig. 4.10c is shown a partial band structure for α-Sn. In this figure is possible seeing how at Γ point occurs the above-mentioned. Without changing the wave vector, an electron can go from the valence to the conduction band. This is readily achieved by absorbing a photon with the right energy. Similarly, an electron from the conduction band may readily move to the valence band by emitting a photon [22].

4.5. Defects in Semiconductors

Crystallographic defects are breaks in crystalline solids regular patterns because the locations of atoms or molecules at repeated fixed distances specified by unit cell parameters in crystals with a periodic crystal structure are generally imperfect. A regular repeating arrangement of atoms in three dimensions gives rise to the crystalline state. The net result is a perfect crystalline solid with all of its atoms present and optimal locations. On the other hand, the ideal crystalline state has zero entropy and hence can only exist at absolute zero temperature. There is a limited chance that defects from ideality will occur at this temperature. Although the number of defects in a perfect crystal is generally tiny, they have a significant impact on the crystal characteristics, such as electronic conductivity and mechanical strength.

4.5.1. Defects Classification

Crystal defects exist in a wide range of forms, and they may be classified in different ways. The main defect types are following:

1. Lattice vacancies/interstitials.
2. Defect clusters.
3. Dislocations.
4. Stacking faults.
5. Grain boundaries

4.5.1.1. Lattice Vacancies/interstitials

4.5.1.1.1. Intrinsic Defects

At thermodynamic equilibrium, intrinsic imperfections such as lattice vacancies and interstitials are in the pure crystal. The simplest crystalline defects, known as point defects, include single or pairs of atoms or ions. Schottky defects, in which an atom or ion pair is absent from the lattice (See Fig. 4.11a), are the most common form of a point defect. An atom or ion is pushed into an interstitial site from its ideal lattice location in Frenkel defects (See Fig. 4.11b).

Consider two isostructural solids, NaCl and AgCl, to illustrate these points. The fcc rock salt structure is adopted by both solids, with ccp Cl^- and Na^+ or Ag^+ in the octahedral positions. Schottky defects are seen in NaCl, where pairs of Na^+ and Cl^- ions are absent from their ideal lattice positions. Overall electroneutrality and stoichiometry are preserved because the anion and cation sublattices have the same vacancies amount. A Frenkel defect with some silver ions displaced from their usual octahedral positions into interstitial tetrahedral sites is favored in AgCl. Because a cation interstitial is generated for every cation vacancy introduced, the anion sublattice remains intact [23].

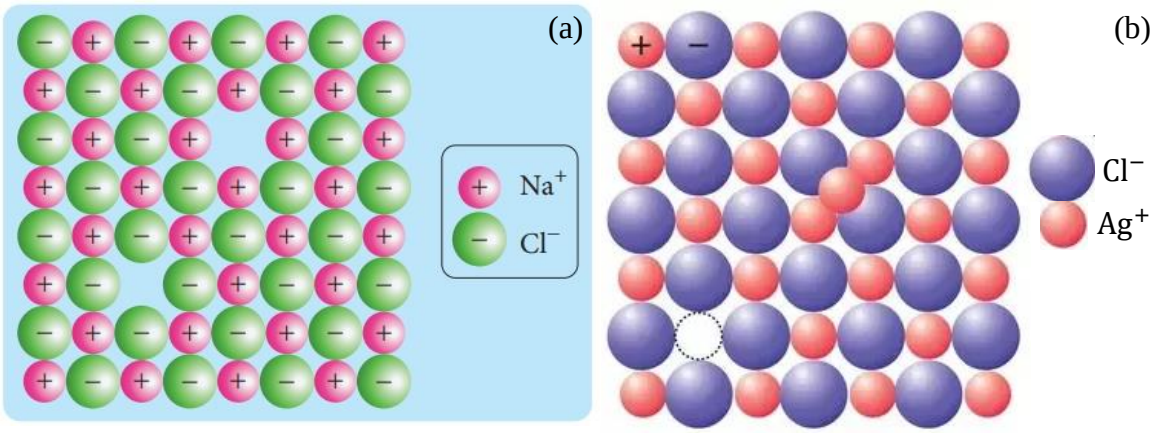

Figure 4.11: (a) Schottky defect representation in NaCl, (b) Frenkel defect representation in AgCl.

Images taken from: (a) *https://img.brainkart.com/extra3/tYnOSrR.jpg, (b) https://3.bp.blogspot.com/-t3jxIsvtLKs/UR8k6qVVejI/AAAAAAAAEPY/w5G5JppBfPg/s1600/Schottky+defect+and+Frenkel+defect.jpg*

Fig. 5 displays two isostructural solids exhibiting two different point defect kinds. This fact is due to the bonding nature between these two solids. NaCl bondings have a high ionic character degree. The cations, which are highly electropositive, follow Pauling's principles well and are difficult to fit into the small tetrahedral site. If sodium ions filled the interstitial tetrahedral sites, which share faces with occupied octahedral sites, they would display substantial cation–cation repulsion. The Ag–Cl covalency bond is significantly greater, with Ag^+ being far less electropositive than Na^+. This indicates that in AgCl, the tight cation-cation interaction necessary for interstitial tetrahedral position occupancy favorable than in NaCl, and the lower coordination number of 4 may be tolerated more readily.

4.5.1.1.2. Extrinsic Defects

At temperatures much below the melting point, the intrinsic defects concentration is generally relatively low. Schottky defects in NaCl, for example, have a concentration of $10^{-17}\cdot mol^{-1}$ at room temperature. The impurity presence or dopant atoms, on the other hand, might enhance the defect concentrations. Extrinsic defects arise when an impurity atom or ion is integrated into the lattice, either by replacement onto the regular lattice site or by insertion into interstitial locations. A compensatory charge must be found inside the lattice to maintain electroneutrality when the impurity is aliovalent to the host sublattice. In the crystal lattice of NaCl, for example, the inclusion of Mg^{2+} results in a cation vacancies equal number. As a result, these defects change the solid compositions. The dopant ion concentration may change dramatically in many systems, which can be exploited to customize specific properties [23].

4.5.1.2. Defect Clusters

The assumption in the simple point defects mentioned above is that structures are unaffected by vacancies or interstitials. This, however, is an oversimplification, as evidenced by the fact that atoms or ions directly surrounding a defect have been discovered to be moved away from their optimum locations in several cases. The defect has grown to include two or more atoms, and it may now be classified as a defect cluster or aggregate. Charge interactions cause the ions around an interstitial to be deformed away from the interstitial ion in ionic crystals where vacancies are effectively charged, with anion vacancies having a positive overall charge and cation vacancies having a negative overall charge. As a result, cation vacancies and interstitial cations are attracted to one another and form simple clusters. Although these clusters are electroneutral on the whole, they do have a dipole, which can attract other defects and lead to the formation of bigger clusters. As a result, given favorable circumstances, individual point defects may merge to create defect clusters. These defect clusters allow for a reduction in total free energy in the development of individual defects. Although these clusters are electroneutral on the whole, they do have a dipole, which can attract other defects and lead to the formation of bigger clusters. As a result, given favorable circumstances, individual point defects may merge to create defect clusters. These defect clusters allow for a reduction in total free energy in the development of individual defects. Solid electrolytes are commonly massively defective systems with large ionic conductivities, and defect clustering is significant in these systems. It was recently proposed that the defect clusters in the solid electrolyte LISICON and its analogs, which have been characterized by neutron diffraction, are mobile and that ionic conduction involves the effective movement of these clusters through an interstitially mechanism rather than a simple ion-hopping model.

The wurtzite defect structure suggested $Fe_{1-x}O$ is a now-classic defect clustering example. Iron would entirely occupy the octahedral sites in fully stoichiometric FeO, expected to adopt the rock salt structure. Nonstoichiometric wurtzite includes a substantial quantity of Fe^{3+}, some of which have been proven to occupy tetrahedral positions by neutron and X-ray diffraction analyses. Even though occupying the tetrahedral site would result in brief interactions between Fe^{3+} in the tetrahedral sites and iron in the octahedral sites, they are unlikely to be occupied at the same time in any structure part. The Koch cluster occurs when alternate tetrahedral sites in the fcc cell are occupied. All adjacent octahedral sites are empty (See Fig. 4.12), resulting in 4 Fe^{3+} interstitials and 13 vacancies, producing a –14 net formal charge. Fe^{3+} ions in adjacent octahedral positions preserve overall electroneutrality. The concentration of Fe^{3+} increases as x increases in $Fe_{1-x}O$, and therefore the spacing between clusters reduces, eventually leading to ordering forming a superlattice structure [23].

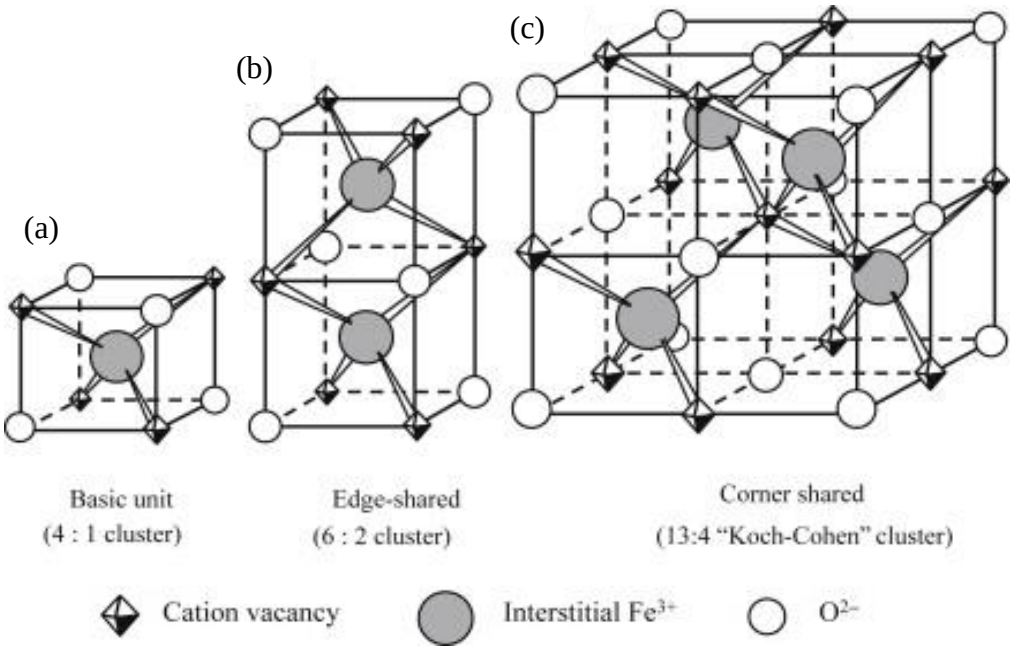

Figure 4.12: Cluster association and vacancy clustering in iron-deficient $Fe_{1-x}O$. (a) The fundamental unit is a 4:1 cluster, which consists of four vacancies and one Fe^{3+} ion in the interstitial space, (b) an edge-shared 6:2 cluster complex was formed by combining two basic units, and (c) a corner-shared 13:4 cluster complex representing a superlattice known as a Koch–Cohen cluster formed by four basic units

Image taken from: *https://ars.els-cdn.com/content/image/3-s2.0-B9780444563699000046-f04-01-9780444563699.jpg*

4.5.1.3. Dislocations

Simple point defects are described so that we get the sense that point defects or tiny defect clusters seem as solitary features in otherwise perfect crystals. This is not wholly true. Individual point defects in many crystals combine to form an extended defect or dislocation. An edge dislocation is the simplest of these, in which an additional atom half-planes form within the lattice (See Fig. 4.13b). The atoms present in the layers above and below the half-plane deform and become non-planar beyond its edge. The half-plane edge direction into the crystal is called the dislocation line.

The Burger's vector is a vector that characterizes dislocations. In a perfect crystal area, if a circular pathway is traced from lattice point to lattice point, the endpoint will be the same lattice point as the starting position. However, if the region includes an edge dislocation, the beginning and finishing positions will not be the same. The distance and direction between them will match the Burger's vector magnitude and direction. Burger's vector is perpendicular to the dislocation line and parallels to the dislocation motion under applied stress for an edge dislocation (See Fig. 4.13b). A screw dislocation is another dislocation kind that arises when an additional step is produced on the crystal surface, resulting in a mismatch that spirals through the crystal. A helix is made when a circular path is followed through lattice points

around a screw dislocation [23]. The resultant Burger's vector is now parallel to the dislocation line (See Fig. 4.13c).

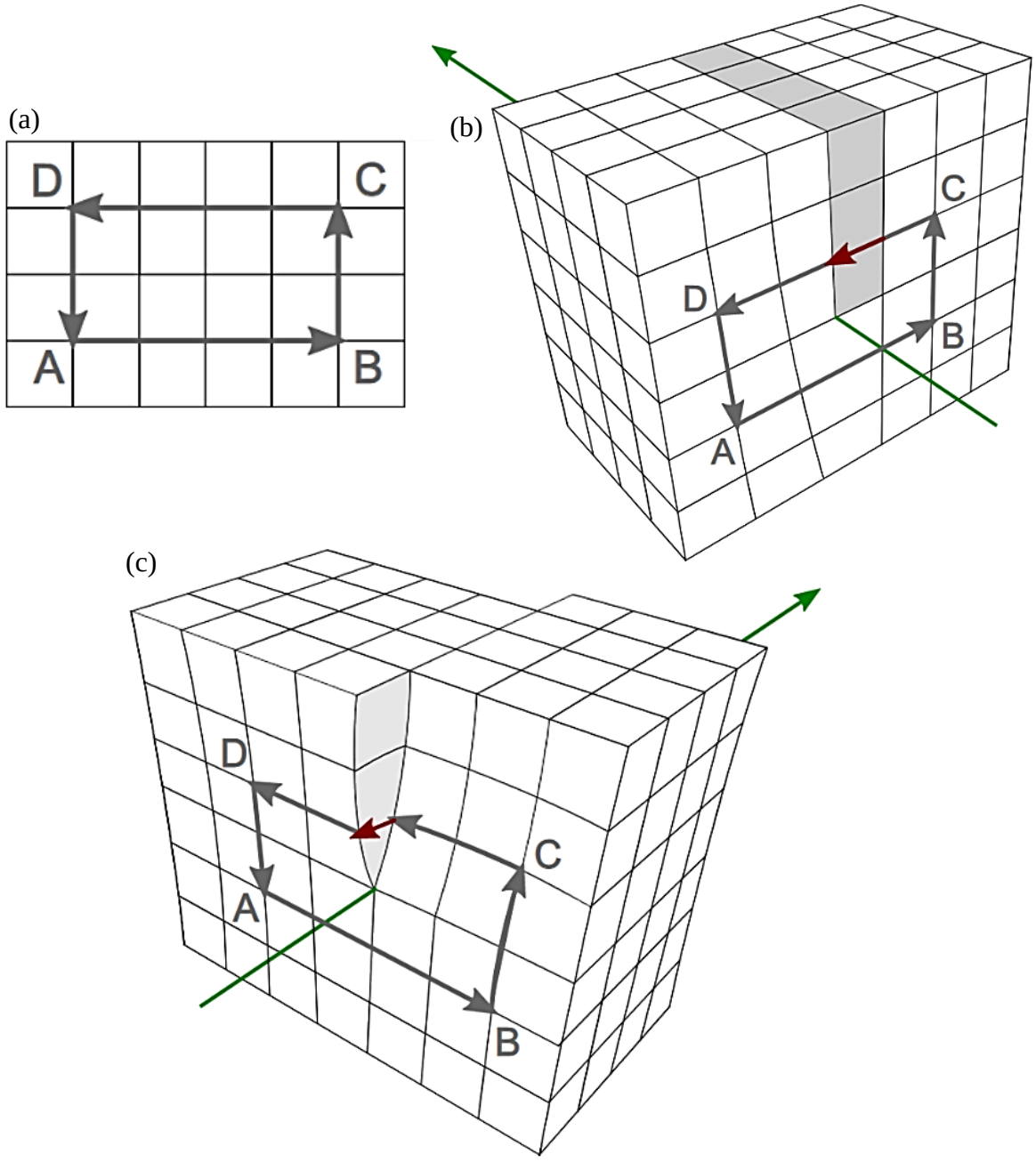

Figure 4.13: Burger's vector in ABCD path for (a) perfect lattice, (b) lattice containing an edge dislocation, and (c) lattice containing a screw dislocation. The green arrow represents the dislocation line, and the vinous arrow corresponds to Burger's vector.

Image adapted from:
https://upload.wikimedia.org/wikipedia/commons/1/1f/Burgers_Vector_and_dislocations_%28screw_and_edge_type%29.svg

4.5.1.4. Stacking Faults

Stacking faults are mismatched layers, as the name indicates. In close-packed systems, a stacking fault can occur during the stacking of individual layers, such as the omission of a C layer in a ccp system, resulting in ...ABCABABC… (See Fig. 4.14a). As a result, the ccp system develops a hcp region. In the case of hcp, a stacking fault may occur when a C layer is added, resulting in the formation of a ccp area within the hcp lattice (Figure 4.14b). Various stacking faults may arise within close-packed systems, although the creation of AA, BB, or CC faults in most systems is extremely energetically unfavorable and is seldom observed. A partial dislocation occurs when the additional plane does not extend across the entire crystal (Figure 4.14c) [23].

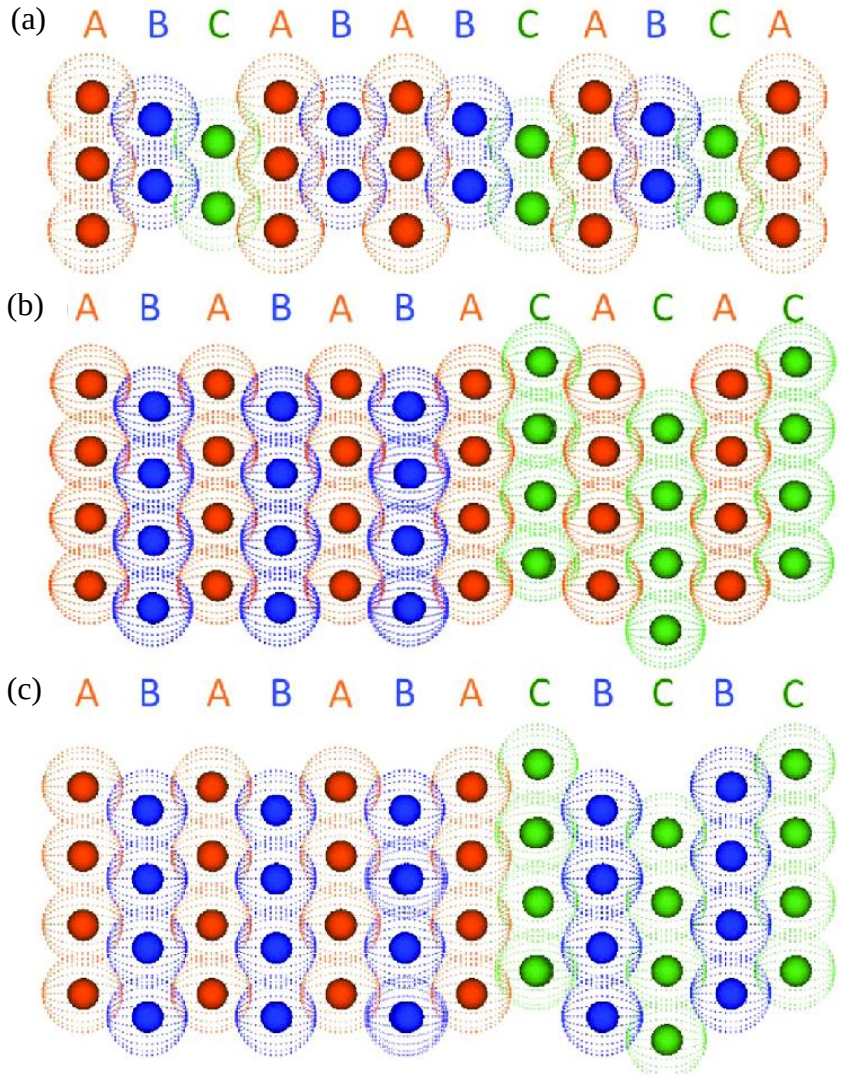

Figure 4.14: Stacking faults. (a) Missing A layer in ccp system, (b) insertion of an C extra layer, and (c) partial stacking fault.

Image taken from:
https://www.researchgate.net/profile/Zongrui_Pei/publication/327558871/figure/fig6/AS:674465021190144@1537816400591/Atomic-structures-of-stacking-faults-The-intrinsic-stacking-fault-in-fcc-crystals-a.png

4.5.1.5. Grain Boundaries

Until now, the crystalline solids descriptions have been limited to single crystal discussions. Although being a composed single chemical phase, most materials are polycrystalline in practice, for example, a metal wire or a ceramic component. Individual crystallites or grains are isolated crystals and maybe orientated arbitrarily concerning one another. As a result, the single grain crystal lattice has just one orientation, which may differ from nearby grains. There are regions between grains that are not aligned with either of their neighbors. Grain boundaries are these transition regions, and their size and complexity significantly impact a lot of the material properties.

Consider two crystallites with crystal lattices that are at an acute angle to one another. Atoms will also fill the gap between the two crystallites. However, due to the angle, atoms full planes will not fit; therefore, portion planes, i.e., edge dislocations, will occupy the gap. As just a consequence, this low-angle grain boundary may be thought of as being made up of a series of edge dislocations. This model is only suitable for low-angle grain boundaries; for angles higher than 10°, more sophisticated structural models are necessary. Low-angle grain boundaries are common in so-called single crystals, which have crystal lattice small misalignments owing to imperfections. This has been used to explain findings like line broadening in X-ray powder diffraction images. Low-angle grain boundaries may be measured using X-ray rocking curve widths; for example, in the IV–VI semiconductor $Pb_{1-x}Ge_xTe$ produced by vapor deposition techniques, low-angle grain boundaries of 1–3° were measured using this method. X-ray topography, which may provide information on dislocation densities and Burger's vectors as well as additional qualitative information about these features, is an alternative and powerful technique for analyzing low-angle grain boundaries and dislocations [23].

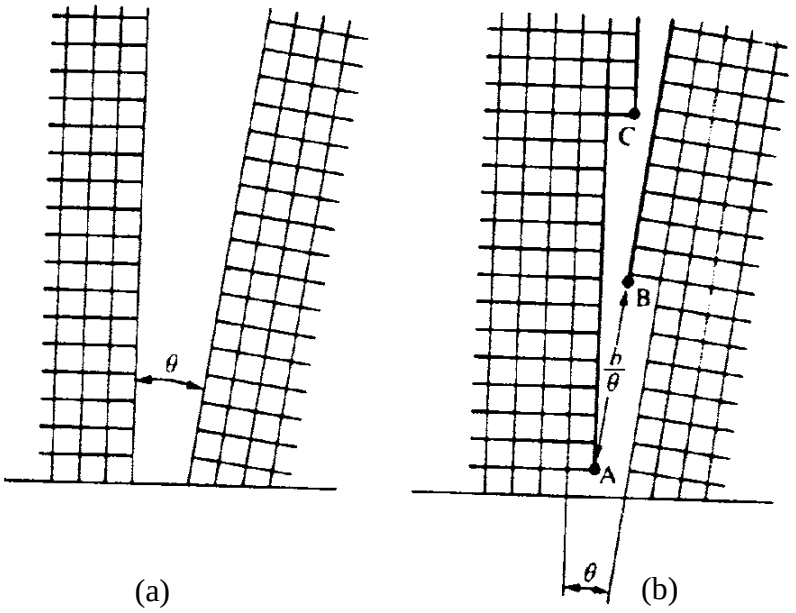

Figure 4.15: (a) Low-angle grain boundary schematic two-dimensional representation. (b) The space between the two crystallites is now filled, forming an edge dislocations array.

Image taken from: Ref. [23]

CHAPTER 5

Experimental Methods

5.1. Samples Selection and Hall Effect Measurements

To study the correlation between thermal and electrical properties in Si as a function of carrier concentration, samples with different resistivities values from 0.005 to 200 Ω·cm were analyzed. To obtain the sample resistivities, a Hall effect system made up of a Keithley 6220 DC source, a Keithley 2000 multimeter, a Keithley 6485 picoammeter, and a 7012-c terminal card coupled with a Keithley 7001 switch system. These instruments were communicated through the IEEE-488 connecters. The Hall effect system uses an Ecopia MP55T Easy-Slide Sample Kit with a 0.5 T magnet (see Fig. 5.1).

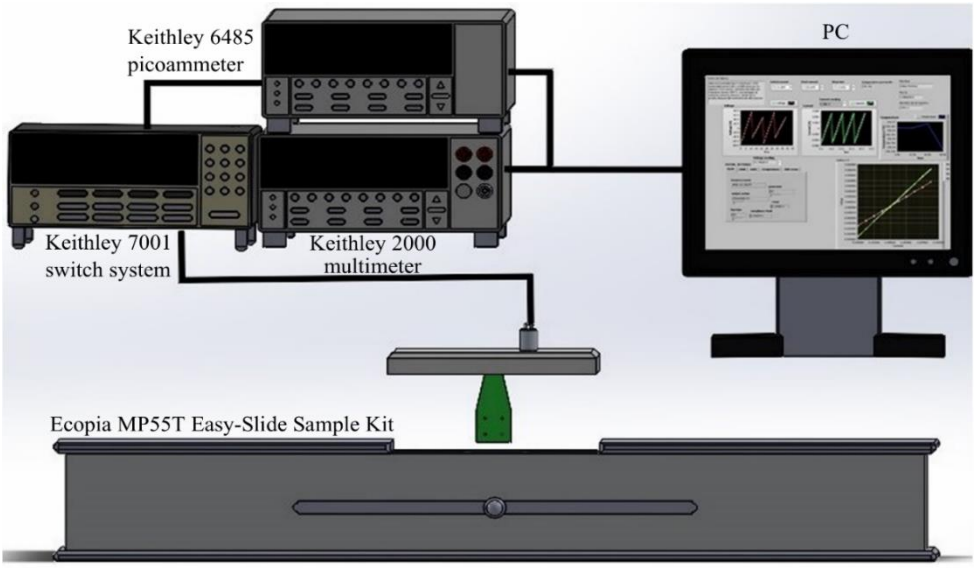

Figure 5.1: Hall effect system.

Table 5.1: Sample characteristics of *p*-Type Si grown in [100] crystallographic direction. The S2 samples set were obtained from a WRS Materials Si wafer, and S1, S3-S6 samples sets were obtained from Polishing Corporation of America Si wafers.

Samples Set	$\rho_{nominal}$ (Ω·cm)	$\rho_{measured}$ (Ω·cm)	Surface state	Thickness (μm)
S1	200	199.4134	One side polished	534 ± 10
	200	197.0557	One side polished	534 ± 10
	200	217.5148	One side polished	534 ± 10
	200	211.1538	One side polished	534 ± 10
S2	1 – 100	88.9174	Both sides polished	518 ± 10
	1 – 100	92.0697	Both sides polished	518 ± 10
	1 – 100	97.6952	Both sides polished	518 ± 10
	1 – 100	79.8467	Both sides polished	518 ± 10
S3	0.1	0.1234	One side polished	517 ± 10
	0.1	0.1478	One side polished	517 ± 10
	0.1	0.1796	One side polished	517 ± 10
	0.1	0.1632	One side polished	517 ± 10
S4	0.05	0.0406	One side polished	522 ± 10
	0.05	0.0415	One side polished	522 ± 10
	0.05	0.0452	One side polished	522 ± 10
	0.05	0.0393	One side polished	522 ± 10
S5	0.01	0.0134	One side polished	537 ± 10
	0.01	0.0129	One side polished	537 ± 10
	0.01	0.0137	One side polished	537 ± 10
	0.01	0.0130	One side polished	537 ± 10

S6	< 0.005	0.0013	One side polished	530 ± 10
	< 0.005	0.0014	One side polished	530 ± 10
	< 0.005	0.0013	One side polished	530 ± 10
	< 0.005	0.0013	One side polished	530 ± 10

Table 5.1 shows the sample characteristics used in this study for. The manufacturer gives the resistivity nominal values for each Si wafer which is an average value. It is necessary to highlight that the carrier distribution is non-homogeneous at different points of the same wafer [1,24]. Therefore, the Hall effect system was used to obtain the resistivities of each one of the samples. 1 cm × 1 cm *p*-Si wafer pieces grown in [100] crystallographic direction were cut by a diamond tip of the wafer center. These samples were obtained from this region because the carrier distribution in the *p*-Si wafer (boron) is more uniform. The S2 samples set were obtained from a WRS Materials Si wafer, and S1, S3-S6 samples sets were obtained from Polishing Corporation of America Si wafers.

5.2. Photocarrier (PCR) Radiometry

PCR was used to obtain sample thermal images. A high-power semiconductor laser (488 nm wavelength, 300 mW) was used. The laser beam was collimated, and then it was focused onto the sample surface with a 40 μm spot size using a gradium lens. The modulated infrared radiation from the excited surface was collected and collimated by two off-axis paraboloid mirrors, and then, it was focused onto a Judson Model J15D12-M204 HgCdTe detector, which was cooled by liquid nitrogen. The detector signal was amplified by a low-noise preamplifier, and then, it was sent to a Lock-In amplifier SR830 DSP Stanford Research System which was interfaced with a PC to collect the data (see Fig. 5.2). A xyz microstages was used to obtain PCR amplitude and phase images. Thermal images were obtained by scanning an area of 0.9 × 0.9 cm from a 0.01 Ω·cm *p*-Si wafer without cuttings.

5.3. X-Ray Diffraction (XRD)

For the crystalline quality determination of each one of the samples, these were crushed until obtaining silicon powder, and it was passed through 12000 US mesh (1 μm) since if the purpose is to make quantitative determinations of the FWHM, it is required that the powder sample be free of particle orientation effects. The measurements were carried out using a diffractometer Rigaku Ultima IV, the configuration was Bragg-Brentano, and the diffractograms were obtained from 5 to 80°. The FWHM was obtained using the characteristic peak (400).

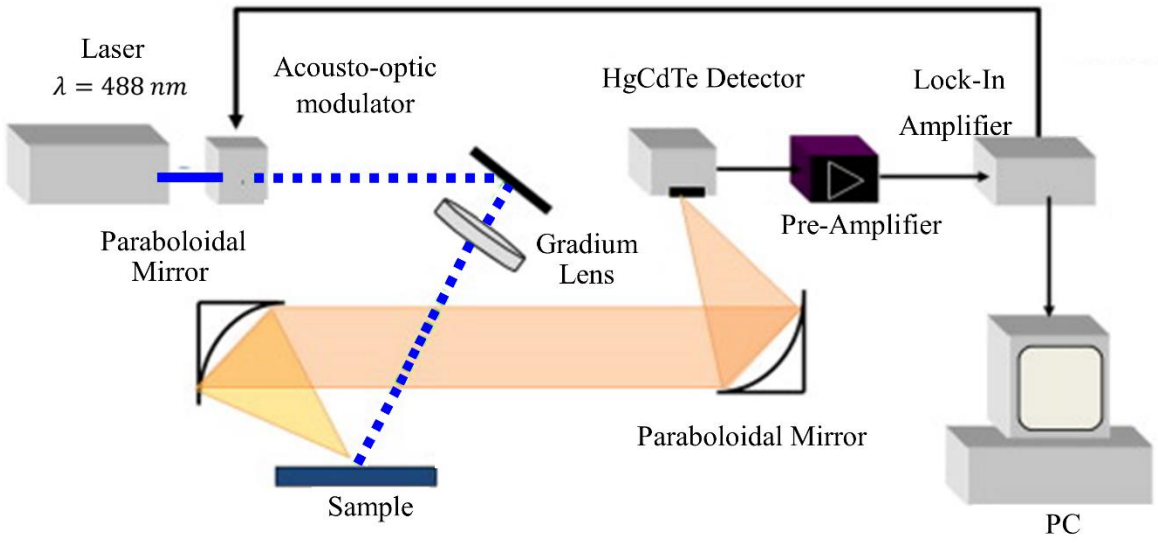

Figure 5.2: PCR experimental set up.

5.4. Photoacoustics

The PA system is made up of a 488 nm laser modulated by a Lock-In amplifier SR830 DSP Stanford Research System. An open photoacoustic cell (OPC) coupled with an electret microphone transduces pressure variations as an electrical signal (see Fig. 5.3). The Rosencwaig and Gersho thermal diffusion model [25] was used to determine photoacoustic signal. In the first place, it should be noted that there are two regimes: thermally thin and thermally thick. In the thermally thin, thermal diffusion length is longer than sample thickness, and for the thermally thick regime, heat flux is attenuated inside the sample. The equation that describes PA signal in thermally thin regime is given by:

$$P_{thin} = \frac{A}{\sqrt{1+(2\pi f\tau_M)^2}}\frac{1}{\sqrt{f}} \tag{5.1}$$

where A is a parameter to determine, f corresponds to frequency scan and τ_M represents the microphone time response. On the other hand, in thermally thick regime, PA signal has the form:

$$P_{thick} = \frac{B}{\sqrt{1+(2\pi f\tau_M)^2}}e^{-a\sqrt{f}} \tag{5.2}$$

where B and a are parameters to determine. The other magnitudes have the same interpretation as Eq. (5.1). Thermal diffusivity is calculated using the following equation:

$$\alpha = \frac{\pi l^2}{a^2} \tag{5.3}$$

α represents the thermal diffusivity, l corresponds to the sample thickness and a comes from Eq. (2).

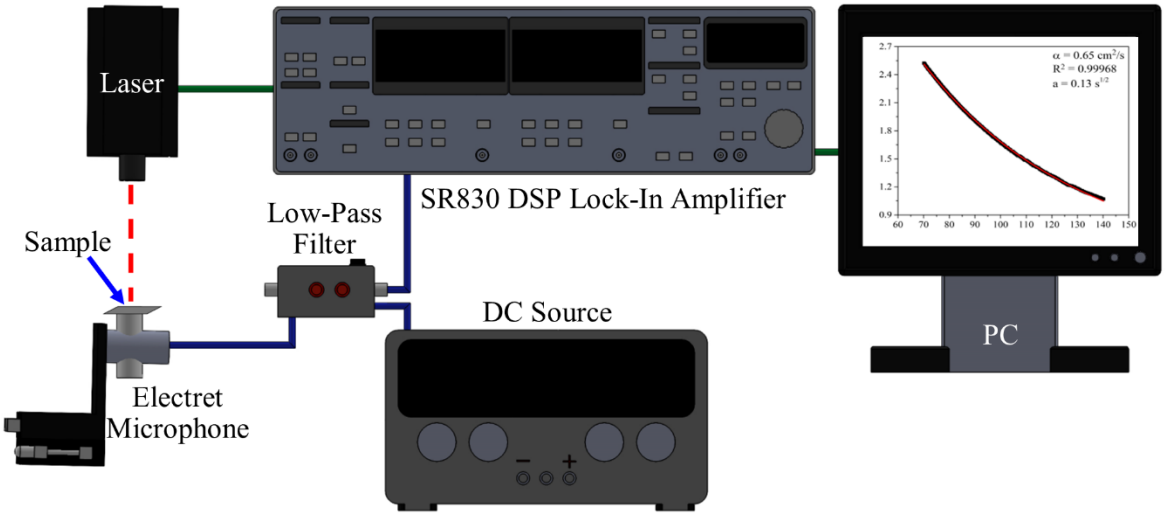

Figure 5.3: PA system arrangement.

5.5. Thermal Relaxation Method

Volumetric heat capacity (ρC) can be determined by the thermal relaxation method [26-28], a thermocouple was placed in contact with the sample back part, in front was illuminated the whole sample area by a 150 Watts LR92240 Schott Lamp to illuminate continuously and uniformly. The sample was inside an isolated vacuum camera to make that heat transfer was mainly by radiation, minimizing convection and conduction contributions. One surface of the sample was sprayed with matte black paint to ensure complete light absorption. The experimental array used for thermal relaxation measurements is shown in Fig. 5.4.

The temperature rise is given by:

$$T(t) = T_f + \Delta T_{MAX} e^{\frac{-t}{\tau_R}} \tag{5.4}$$

where T_f is the final temperature, t represents the thermal excitation time, ΔT_{MAX} corresponds to the maximum temperature difference, and τ_R corresponds to the thermal relaxation time, τ_R value is related to the volumetric heat capacity through the following equation:

$$\rho C = \frac{8\tau_R \epsilon \sigma T_0^3}{l} \tag{5.5}$$

ϵ is the thermal emissivity that is considered 1 in this case, σ is the Stefan-Boltzmann constant, T_0 is the initial temperature and l is the thickness sample. The thermal conductivity is calculated by Eq. (5.6):

$$\kappa = \alpha \rho C \tag{5.5}$$

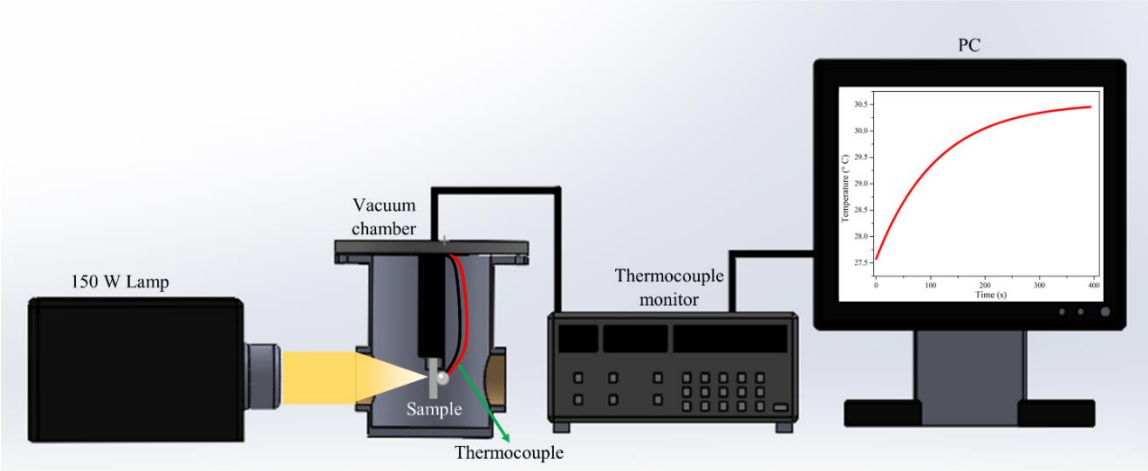

Figure 5.4: Thermal relaxation method experimental arrangement.

CHAPTER 6

Results and Discussion

6.1. Microphone Calibration in Photoacoustics

The microphone calibration, which is generally done using aluminum foil, is an important part of the PA technique. To determine the microphone time response τ_M, a 1 cm × 1 cm × 17 cm commercial aluminum foil sample (Azteca, produced in México) was utilized. This technique has been used to determine the thermal diffusivities of semiconductors [29], metals [26], and polymers [30]. This τ_M was not reported [31-34], which, according to Eq. (5.1), is a crucial point for determining thermal diffusivity values.

The PA amplitude signal as a function of frequency for the thermally thin regimen is shown in Fig. 6.1(a). The black squares represent experimental data, whereas the continuous red line is the Eq. (5.1) best fitting. The microphone time response was 2.12 ms, which was used to obtain the thermal diffusivity values. The PA signal for Al in the thermally thick regimen is shown in Fig. 6.1(b). The experimental data are shown by black squares, whereas the continuous red line represents the Eq. (5.2) best fitting. Fig. 6.1(c) shows the Al sample diffraction pattern, where it is possible seeing a polycrystalline structure and various crystalline phases. These phases were identified with PDF-4 software. Each phase card number from the International Centre for Diffraction Data (ICDD) is displayed. Commercial aluminum foil (see Fig. 6.1(c)) is composed of alloys including manganese (Mn), iron (Fe) in various phases, and silicon dioxide (SiO_2). The α for Al was 0.46 cm^2/s, as seen in Fig. 6.1(b). This value differs from those determined via a photothermal technique for Al [35]. The published values for various Al single-crystals are 0.83 cm^2/s, 0.94 cm^2/s, and 0.95 cm^2/s; it is important to note that these results are valid provided the sample is monocrystalline with high crystalline quality, although a diffraction pattern was not presented in Ref. [35]. So, there is no way of knowing if it is an Al single-crystal. Due to the presence of impurities, defects, and mechanical stress caused by rolling, the commercial Al thermal diffusivity found was 0.46 cm^2/s, which is lower than reported by MacCormack [35].

$M0n_{11.6}Al_{27.4}$, $FeAlO_3$, Al, Fe, $MnAl_2O_4$, and SiO_2 are among the phases found. Mn, Fe, O, and Si atoms modify the Al crystal structure, affecting the diffusive process due to a greater defect density. As a result, the low thermal diffusivity value found in this study is consistent.

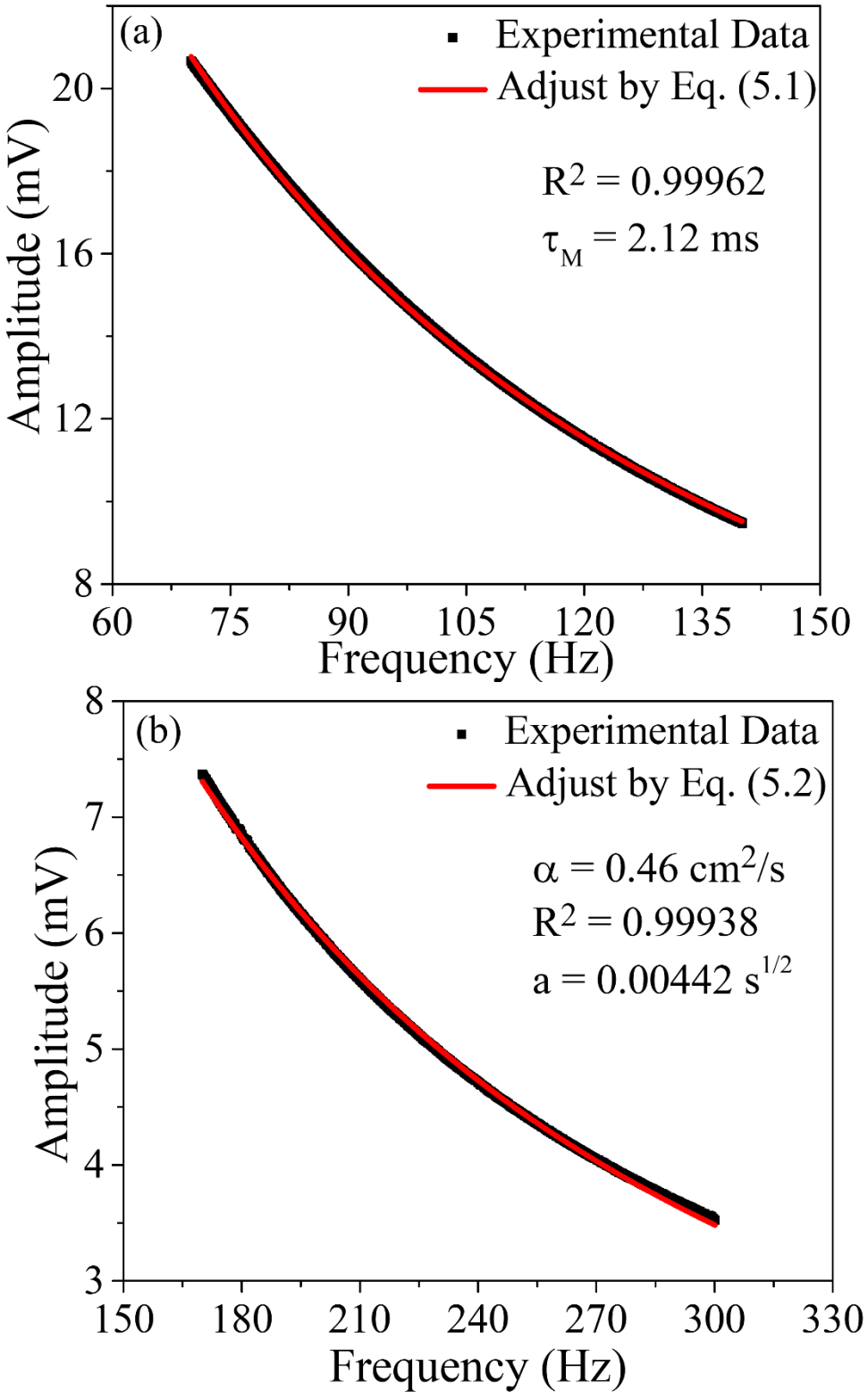

Figure continue

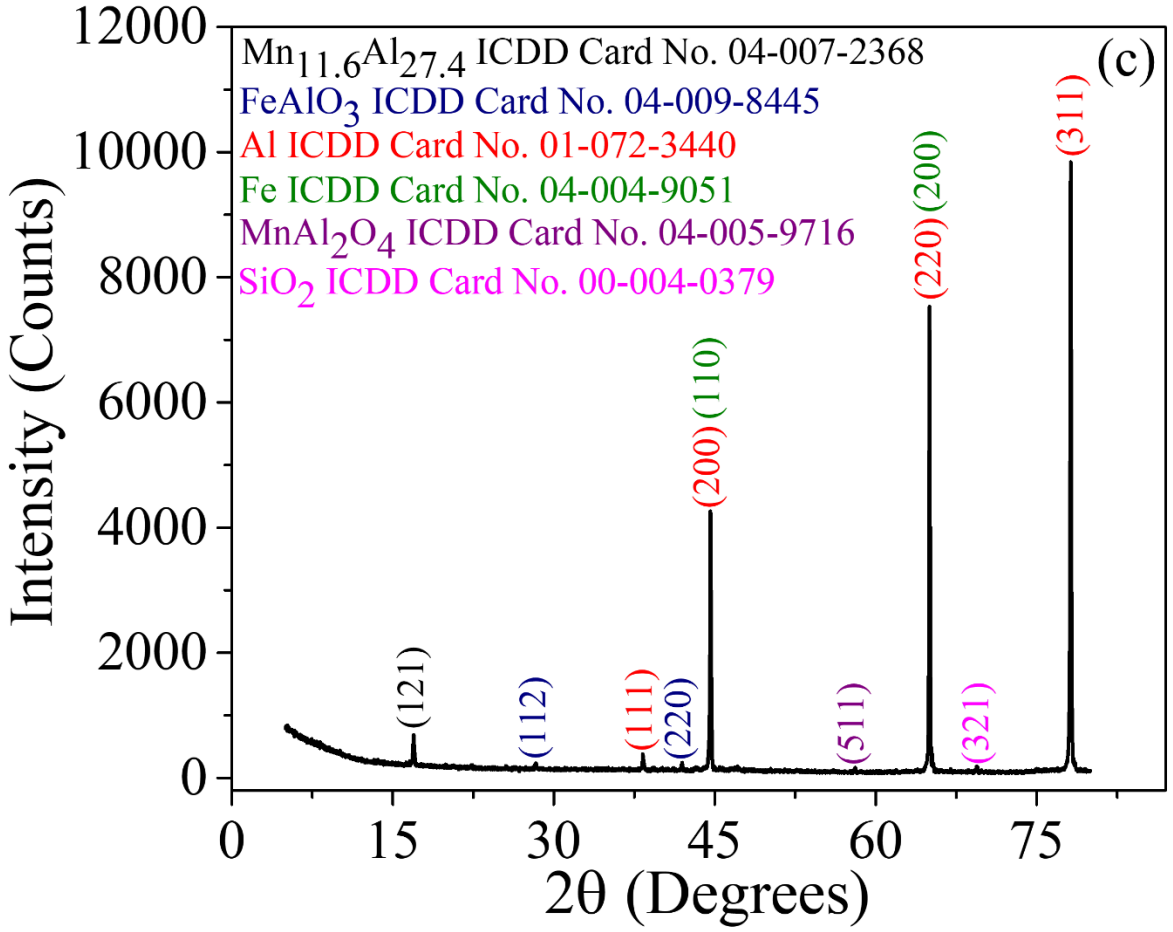

Figure 6.1: For Al foil: (a) PA amplitude signal as a function of frequency in thermally thin regimen, (b) PA amplitude signal as a function of frequency in thermally thick regimen, and (c) X-ray diffraction pattern with identified phases.

6.2. Thermal Images

At room temperature, PCR was utilized to get the carrier distribution in the center section of a *p*-Si wafer (see Fig. 6.2(a)). The PCR amplitude signal for two locations in this area is shown in Fig. 6.2(b). The boron atoms are not evenly distributed over the wafer, according to Rodriguez et al. [1], resulting in intrinsic defects in the wafer [23]. This defect type affects the structural and thermal properties of the wafer, implying that different carrier distributions affect the wafer thermal properties in local regions

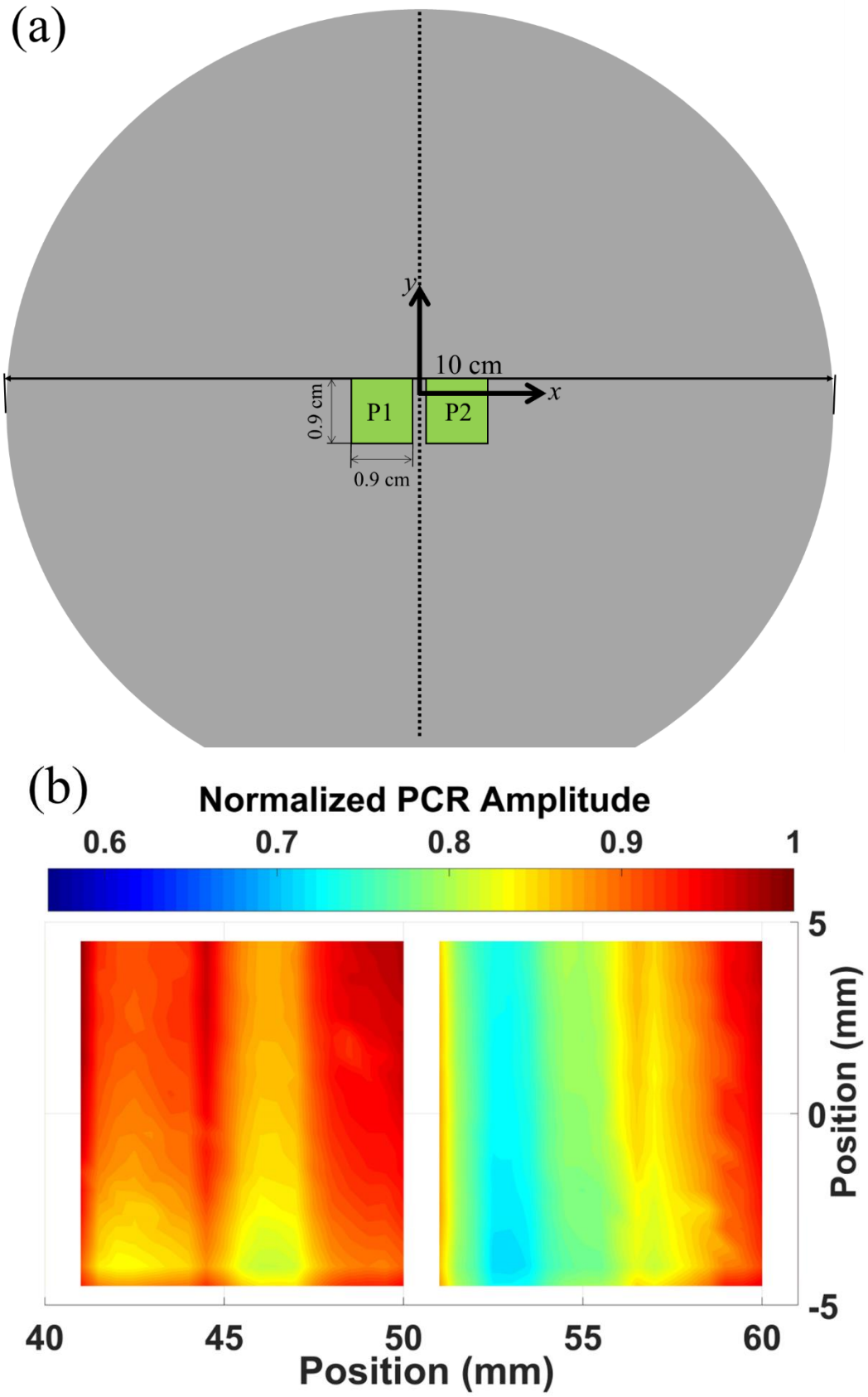

Figure 6.2: (a) Schematic Si wafer scanned places by PCR and (b) PCR thermal images of Si wafer central part.

6.3. Electrical Properties

The *p*-Si sample variations in the resistivity as a function of carrier concentration are shown in Fig. 6.3. S1 to S6 correspond to the experimental data for each studied sample set cut from six Si wafers at different positions using the four points method and the Hall effect system. The black squares and red circles correspond to the resistivity behaviors reported by [36,37]. The carrier concentration measurements reported in this study show an apparent rise of several orders of magnitude for each sample set. The carrier concentration values that should have been attained in this investigation are shown by the arrows.

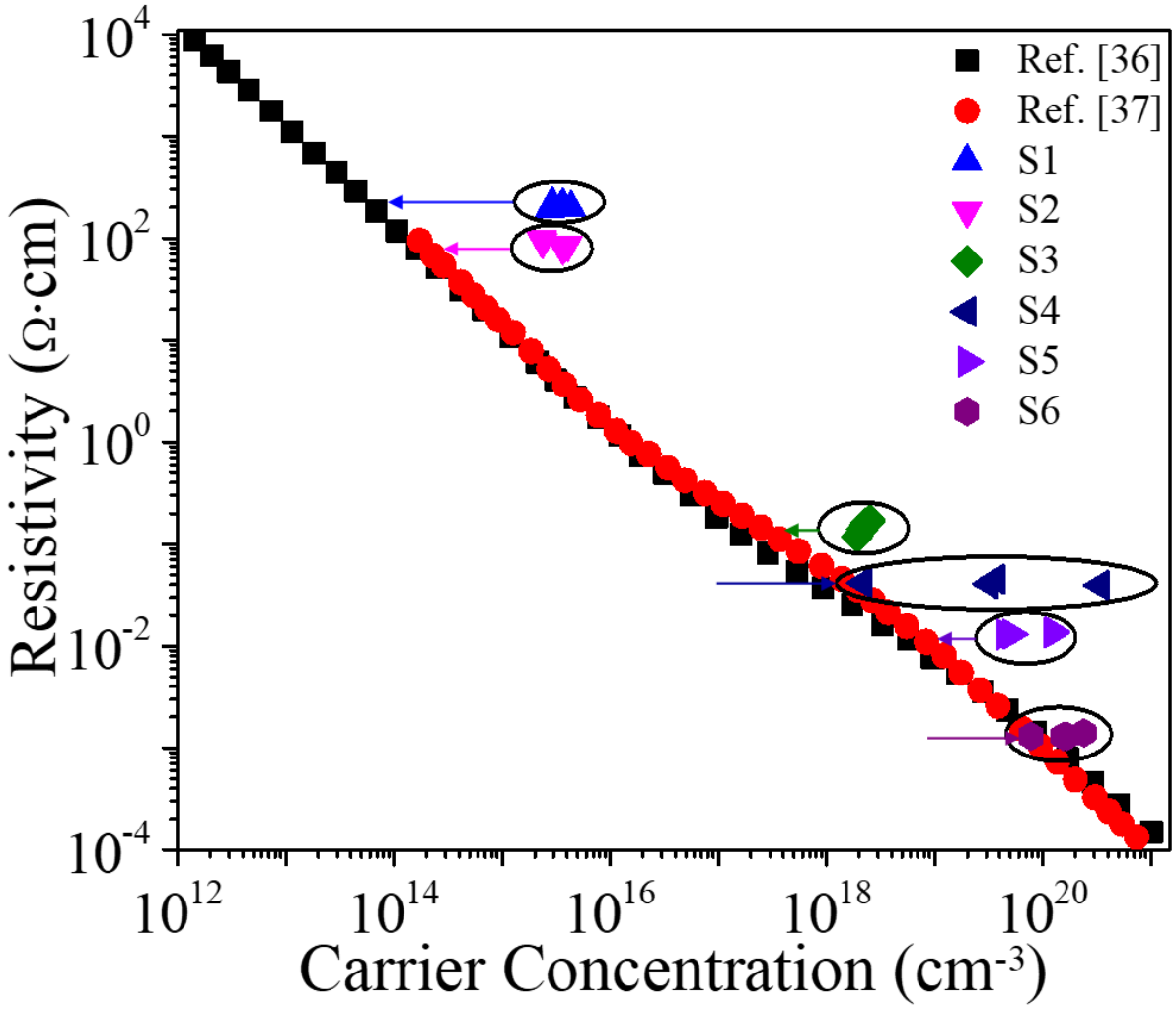

Figure 6.3: *p*-Si resistivity as a function of carrier concentration obtained by Refs. [36, 37], and this work.

The Hall effect detects variations in spatial carrier distribution that result in changes in carrier concentration determinations. Discrepancies between reported values and these experimental results, as seen in Fig. 3, are explained by Hall effect models. The Hall coefficient may be calculated as follows:

$$R_H = \frac{\rho e \tau}{m_e^*} \tag{6.1}$$

where ρ corresponds to the resistivity, τ is related to the effective carrier lifetime, and e and m_e^* represent the charge and effective mass for the electron, respectively. Furthermore, the carrier concentration is:

$$n = \frac{1}{R_H e} \tag{6.2}$$

which is the same:

$$n = \frac{m_e^*}{\rho \tau e^2} \tag{6.3}$$

Eq. (6.3) explain why the carrier concentration values were several orders of magnitude higher than the reported values in Fig. 6.3. It can be observed from Eq. (6.3) that the high values of carrier concentration found in this study are attributable to electrons having a shorter effective lifetime, which is related to the damage caused by sample preparation associated with a defect density increase. The samples appear to contain more carriers, but really, the lifetime was lowered. It is due to interactions between the Si bulk and defect interfaces, on the other hand, scatter phononic modes, influencing the heat diffusion process.

6.4. Structural Properties

Because carrier diffusion is linked to the free mean path, sample structural properties influence other properties such as electrical, vibrational, optical, and thermal. Electrons, holes, and phonons go through the lattice depending on the lattice state that governs the diffusion (conduction) and the vibrational modes scattering. The thermal properties are usually measured in tiny cut samples, but the influence on the lattice of the cut is never taken into account. The structural properties of the samples, as well as their thermal ones, are never reported. Because carrier diffusion is linked to the free mean path, sample structural properties influence other properties such as electrical, vibrational, optical, and thermal. Electrons, holes, and phonons go through the lattice, which it state governs the diffusion (conduction) and the vibrational modes scattering. The thermal properties are usually measured in cut tiny samples, but the cut influence on the lattice is never taken into account. The structural properties of the samples, as well as their thermal ones, are never reported.

Fig. 6.4(a) shows the peak position of the powdered Si sample for the (400) plane, which corresponds to the [100] direction. Fig. 4(b) shows the FWHM as a function of the carrier concentration, the (400) peak was used for this determination. As seen in Fig. 4(b), the FWHM rises in a non-linear manner as the carrier concentration increases. The boron (B) distribution in the Si matrix is associated with reductions in crystalline quality. The B radius is 180 pm, while the Si radius is 210 pm. As a result, the crystalline quality diminishes when carrier concentration rises, revealing that the Si lattice is deformed by doping.

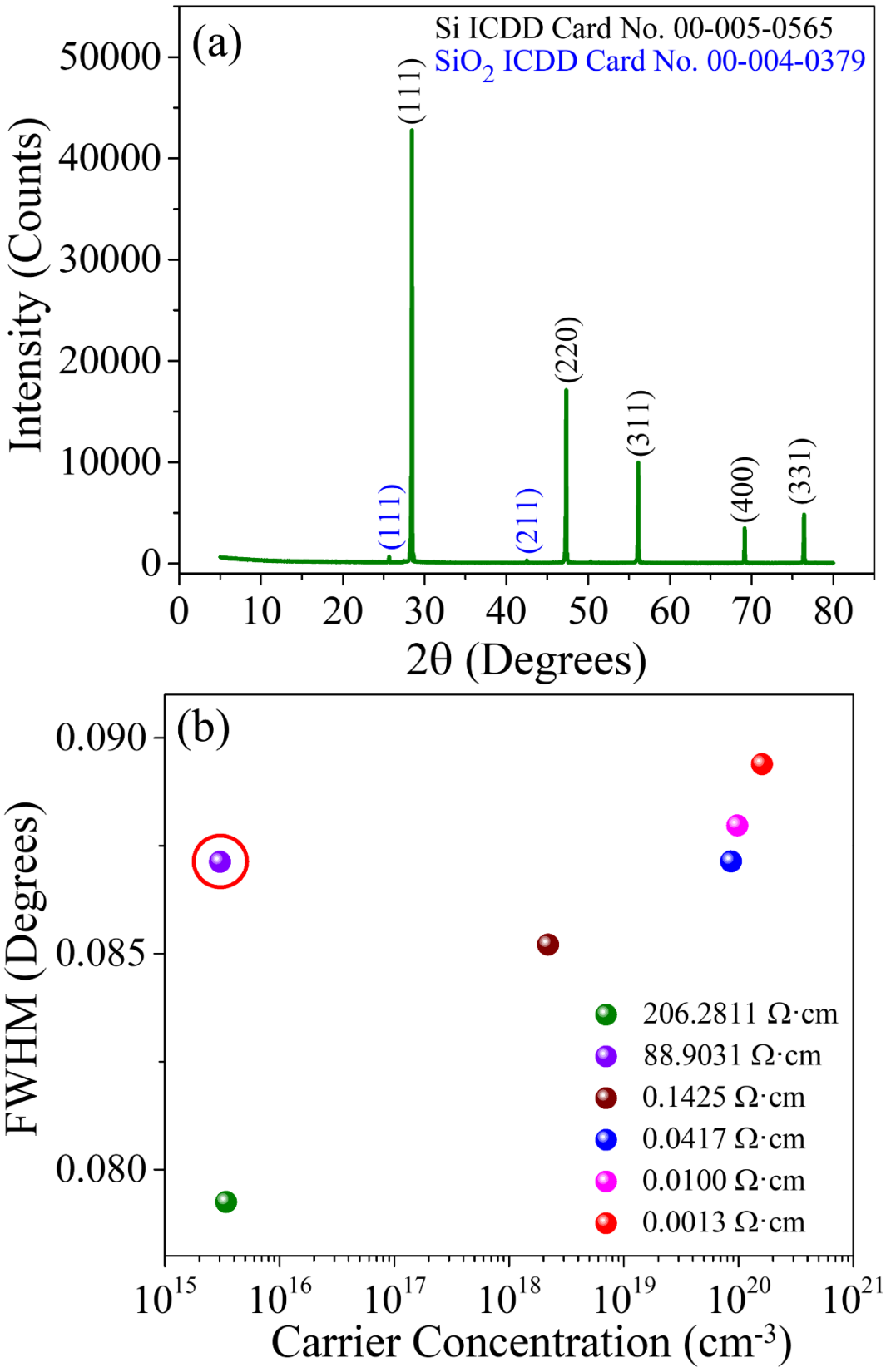

Figure 6.4: (a) Diffraction pattern for the 0.0013 Ω·cm Si sample and (b) FWHM as a function of carrier concentration.

The sample S2 (88.9031 cm) crystalline quality, which is highlighted with a red circle, is lower than the crystalline quality of samples S3 (0.1425 cm) and S4 (0.0417 cm), which have greater carrier concentrations. In this sample, both sides were polished, and the defect density was greater than in the other samples. This is understandable given that various manufacturers produce samples with the same resistivity but different thermo-electronic properties due to different postproduction procedures.

6.5. Thermal Diffusivity

As was the above-mentioned, structural properties affect thermal ones, in this sense, thermal diffusivity measures carrier and phonon diffusion across the lattice, dependent on the lattice state (extrinsic and intrinsic behavior). There are intrinsic and extrinsic defects in a Si wafer. The carrier distribution determines intrinsic ones, whereas the manufacturing process regulates extrinsic ones. Mechanical damage occurs when a crystalline wafer is sliced with a diamond tip to get tiny samples. Rodriguez-Garcia et al. [1] described a line scratch that was intentionally created and measured by PTR. The line was made by a diamond tip; the technique detects the structural changes as defects, producing lattice damages that impact carrier and phonon diffusion, implying that sample preparation causes lattice damage, which affects the thermal and electrical properties of a particular sample.

Using the methodology described in the 5.4 and 6.1 sections, the thermal diffusivity of a *p*-type Si wafer with resistivity of 0.1 Ω·cm was obtained at different points in the same wafer without mechanical damages. Fig. 6.5 depicts the variations in thermal diffusivity throughout the wafer at various positions. Local variations ranging from 0.54 to 0.86 cm^2/s can be observed. The carrier distribution and local changes in the densities of surface and bulk defects (states) created during the polishing process are related to these variations in this thermal property.

6.6. Thermal, electrical, and structural properties: The correlation

The thermal properties as a function of carrier concentration and the thermal ones as a function of FWHM are shown in Figs. 6.6 and 6.7, respectively. The reduction in thermal conductivity, thermal diffusivity, and volumetric heat capacity is related to FWHM rises by the decrease in the crystalline quality. The S2 (88.9031 Ω·cm) sample set verifies the B inclusion effect and the local defect density changes relating to the polishing procedure. Both sides of this sample have been polished, as previously stated. As a result, a high defect density generates a high FWHM value, indicating low crystalline quality regardless of B dosages. The scattering process via electron-defect and phonon-defect interactions rises, suggesting a

reduction in carrier lifetime, which influences heat transport by electron flux, and a decrease in the mean free path, that governs the phonon distribution affecting the heat diffusion process.

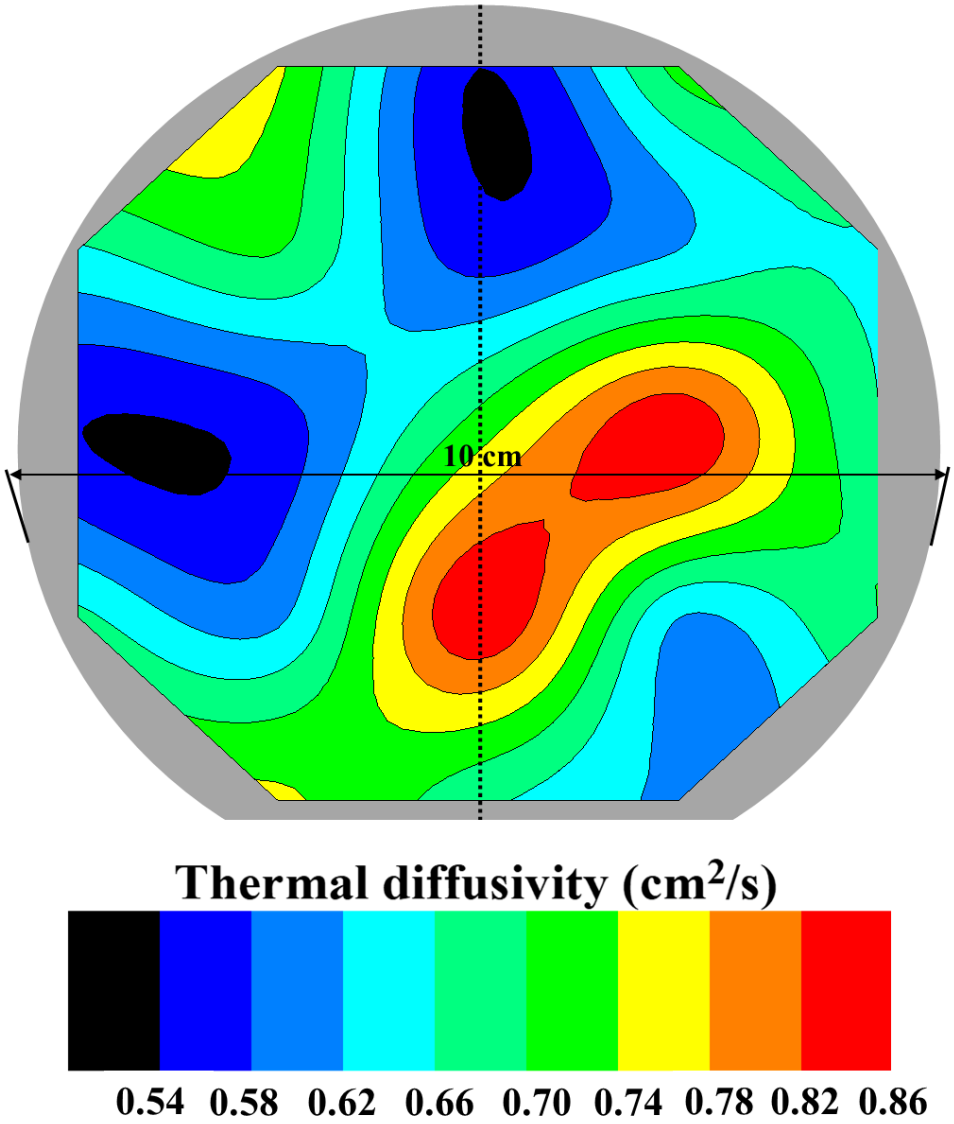

Figure 6.5: Thermal diffusivity contour map taken from a *p*-type Si wafer with a resistivity of 0.1 Ω·cm (S3) grown in the [100] direction.

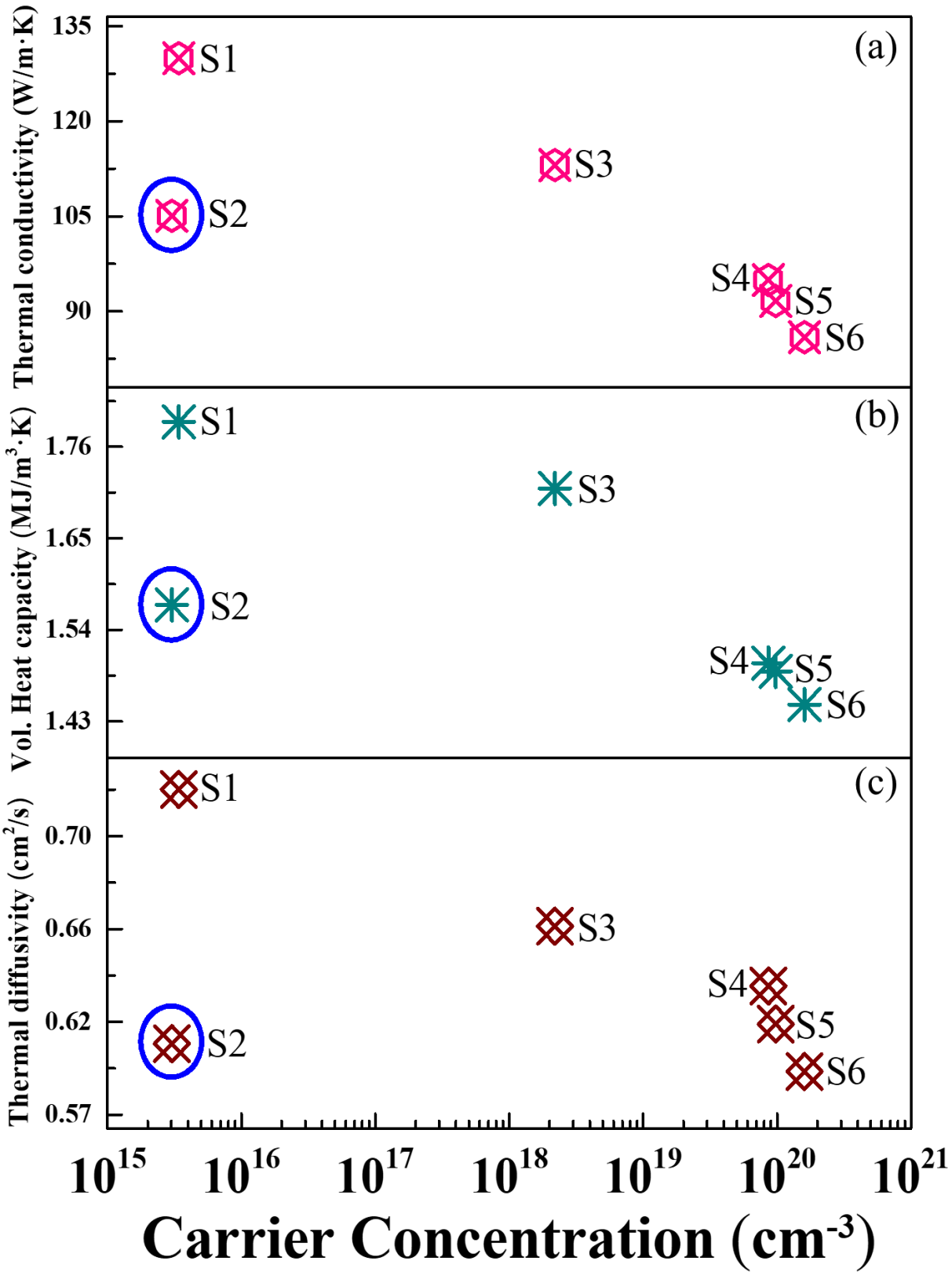

Figure 6.6: As a function of carrier concentration, (a) thermal conductivity, (b) volumetric heat capacity, and (c) thermal conductivity.

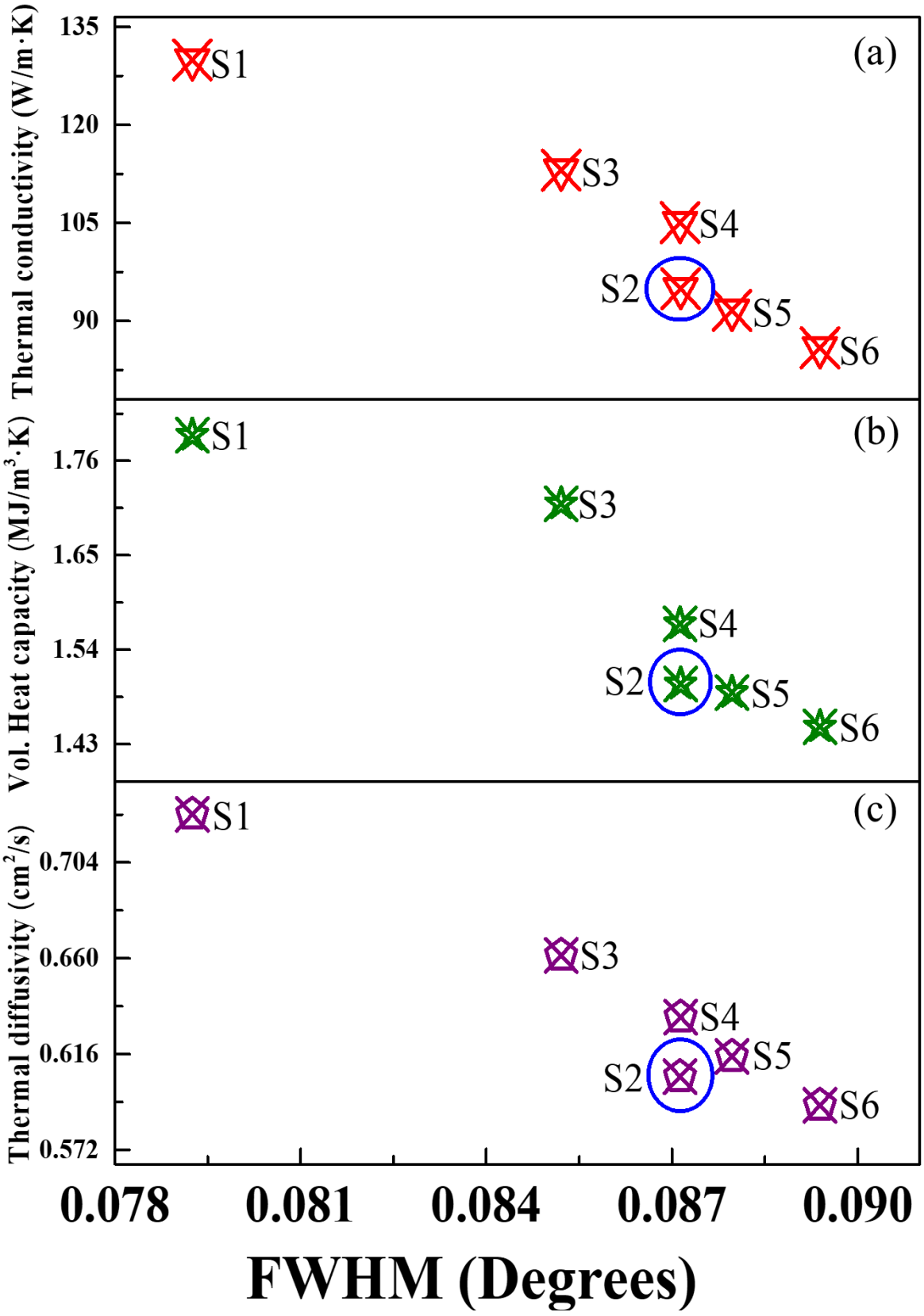

Figure 6.7: As a function of FWHM, (a) thermal conductivity, (b) volumetric heat capacity, and (c) thermal conductivity.

CHAPTER 7

Conclusions

- The photoacoustic technique requires the microphone calibration and the microphone time response determination to obtain the thermal diffusivity as suggested by the models of the photoacoustic signal both in the thermally thin regime and in the thermally thick regime.

- The characteristic Si wafer PCR images showed that the B is not uniformly distributed across the wafer, affecting thermal and electrical properties locally.

- The apparent carrier concentration increases are associated with the decreasing effective carrier lifetime, corroborated by the Hall effect measurements relating it the structure and the electrical transport. The structure state produces drastic effects on the thermal and electrical properties.

- The crystalline quality depends on the B concentration increase, intrinsically. The thermal properties decrease if the FWHM increases by the lattice deformation, product of the B inclusion in the Si matrix.

- The defect density varies locally in the whole Si wafer by the polishing and the manufacturing processes, extrinsically, giving local thermal and electrical properties.

- The thermal properties are affected by the decrease in the mean free path that governs the phonon distribution determined by the lattice state.

- The sample preparation induces mechanical damages in the Si samples structure, extrinsically

- The thermal, electrical, and structural properties are determined by intrinsic and extrinsic parameters involving B doping concentration, manufacturing process, and sample preparation.

- Thermal, electrical, and structural properties are inseparable.

- The photothermal techniques allowed the relations of the lattice state with the intrinsic and extrinsic parameters corroborating that the lattice state governs thermal and electrical properties.

References

[1] M. Rodriguez-Garcia, A. Mandelis, G. Pan, L. Nicolaides, J. García and Y. Riopel, "Computational Aspects of Laser radiometric multiparameter Fit for carrier transport property measurements in Si wafers," *J. Electrochem. Soc.,* vol. 147, no. 2, pp. 687-698, 2000.

[2] C. Feng, P. Chen, T. Yang, B. Yu and L. Qian, "Repairing slight damages on monocrystalline silicon surface by thermal annealing," *Materials Research Express,* vol. 8, no. 045005, pp. 1-8, 2021.

[3] D. Dumin and W. Henry, "Defect generation in silicon," *Metallurgical Transactions,* vol. 2, pp. 677-681, 1971.

[4] L. Wu, B. Yu, P. Zhang, C. Feng, P. Chen, L. Deng, J. Gao, C. S., S. Jiang and L. Qian, " Rapid identification of ultrathin amorphous damage on monocrystalline silicon surface," *Physical Chemistry Chemical Physics,* vol. 22, pp. 12987-12995, 2020.

[5] H. R. Shanks, P. D. Maycock, P. H. Sidles and G. C. Danielson, "Thermal Conductivity of Silicon from 300 to 1400°K," *Phys. Rev.,* vol. 130, no. 5, pp. 1743-1748, 1963.

[6] C. J. Glassbrenner and G. A. Slack, "Thermal conductivity of silicon and germanium from 3 K to the melting point," *Phys. Rev.,* vol. 134, pp. A1058-A1069, 1964.

[7] M. Rodriguez-Garcia, A. Gutiérrez, O. Zelaya-Angel, C. Vázquez and J. Giraldo, "Influence of crystalline quality on the thermal, optical and structural properties of $Cd_{1-x}Zn_xTe$ for low zinc concentration," *Journal of Crystal Growth,* vol. 233, no. 1-2, pp. 275-281, 2001.

[8] A. Stranz, J. Kähler, A. Waag and E. Peiner, "Thermoelectric properties of high-doped silicon from room temperature to 900 K," *Journal of Electronic Materials,* vol. 42, pp. 2381-2387, 2013.

[9] P. Drude, "Zur Elektronentheorie der Metalle," *Annalen der Physik,* vol. 306, no. 3, pp. 566-613, 1900.

[10] B. Donovan, Elementary Theory of Metals, Oxford: Pergamon Press, 1967.

[11] S. Kasap and P. Capper, Springer Hanbook of Electronic and Photonic Materials, © Springer International Publishing, 2017.

[12] P. Y. Yu and M. Cardona, Fundamentals of Semiconductor - Fourth Edition, Berkely and Stuttgart: Springer, 2010.

[13] A. P. Sutton, Electronic Structure of Materials, Oxford: Carendon Press, 1994.

[14] L. J. Van der Pauw, "A method of measuring specific resistivity and Hall effect of discs of arbitrary shape," *Phillips Research Reports,* vol. 13, pp. 1-9, 1958.

[15] L. J. Van der Pauw, "A method of measuring the resistivity and Hall coeffcient on lamellae of arbitrary shape," *Phillips Tehcnical Review,* vol. 20, pp. 220-224, 1958.

[16] D. P. Almond and P. M. Patel, Photothermal Science and Techniques, London: Chapman and Hall, 1996.

[17] H. S. Carslaw and J. C. Jaeger, Conduction of Heat in Solids, New York: Oxford Science Publications, 1989.

[18] W. D. Callister, Materials Science and Engineering, New York: John Wiley & Sons Inc, 2007.

[19] A. Salazar, "On thermal diffusivity," *European Journal of Physics,* vol. 24, pp. 351-358, 2003.

[20] C. Kittel, Solid State Physics, Eight Edition, Hoboken, New Jersey: John Wiley & Sons, Inc, 2005.

[21] M. Fox, Optical Properties of Solids, Second Edition, New York: Oxford University Press Inc., 2010.

[22] A. Goetzberger, J. Knobloch and B. Voss, Crystalline Silicon Solar Cells, Chichester: John Wiley & Sons, 1998.

[23] P. Gellings and H. Bouwmeesterm, The CRC Handbook of Solid State Electrochemistry, Boca Raton: CRC Press Inc. , 1997.

[24] C. F. Ramirez-Gutierrez, H. D. Martinez-Hernandez, I. A. Lujan-Cabrera and M. E. Rodriguez-Garcia, "Design, fabrication, and optical characterization of one-dimensional photonic crystals based on porous siliconassisted by in-situ photoacoustics," *Scientific Reports,* vol. 9, pp. 1-9, 2019.

[25] A. Rosencwaig and A. Gersho, "Theory of the photoacoustic effect with solids," *Journal of Applied Physics,* vol. 47, no. 1, pp. 64-69, 1976.

[26] I. Rojas-Rodriguez, A. Lara-Guevara, M. Salazar-Sicacha, J. C. Mosquera-Mosquera, M. Robles-Agudo, C. Ramirez-Gutierrez and M. Rodriguez-Garcia, "The Influence of the Precipitation Heat Treatment Temperature on the Metallurgical,Microstructure, Thermal Properties, andMicrohardness of an Alpha Brass," *Materials Sciences and Applications,* vol. 9, pp. 440-454, 2018.

[27] E. Marín, O. Delgado-Vasallo and H. Valiente, "A temperature relaxation method for the measurement of the specific heat of solids at room temperature in student laboratories," *American Journal of Physics,* vol. 71, no. 10, pp. 1032-1036, 2003.

[28] I. Hatta, "Heat capacity measurements by means of thermal relaxation method in medium temperature range," *Review of Scientific Instruments,* vol. 50, pp. 292-295, 1979.

[29] S. Zelewski and R. Kudrawiec, "Photoacoustic and modulated reflectance studies of indirect and direct band gap in van der Waals crystals," *Scientific Reports,* vol. 7, pp. 1-11, 2017.

[30] N. A. George, "Thermal diffusivity of liquid crystalline polymers measured using open cell photoacoustic technique," *Smart Materials and Structures,* vol. 11, pp. 561-564, 2002.

[31] D. M. Todorovic, P. M. Nikolic, M. D. Dramicanin, D. G. Vasiljevic and Z. D. Ristovski, "Photoacoustic frequency heat-transmission technique: Thermal and carrier transport parameters measurements in silicon," *Journal of Applied Physics,* vol. 78, no. 9, pp. 5750-5755, 1995.

[32] A. Somer, A. Gonçalvez, T. Moreno, G. Kniphoff da Cruz, M. Baesso, N. Astrath and A. Novatski, "Photoacoustic signal with two heating sources: theoretical predictions and experimental results for the open photoacoustic cell technique," *Measurement Science and Technology,* vol. 31, pp. 1-11, 2020.

[33] J. A. Baldera-Lopez and A. Mandelis, "Thermal diffusivity measurements in the photoacoustic open-cell configuration using simple signal normalization techniques," *Jorunal of Applied Physics,* vol. 90, no. 5, pp. 2273-2279, 2001.

[34] W. L. Barros Melo and R. M. Faria, "Photoacoustic procedure for measuring thermal parameters of transparent solids," *Applied Physics Letter,* vol. 67, no. 26, pp. 3892-3894, 1995.

[35] E. MacCormack, A. Mandelis, M. Munidasa, B. Farahbaksh and H. Sang, "Measurements of the Thermal Diffusivity of Aluminum Using Frequency-Scanned, Transient, and Rate Window Photothermal Radiometry.Theory and Experiment," *International Journal of Thermophysics,* vol. 18, no. 1, pp. 221-250, 1997.

[36] J. Irvin, "Resistivity of Bulk Silicon and of Diffused Layers in Silicon," *The Bell System Technical Journal,* vol. 41, no. 2, pp. 387-410, 1962.

[37] S. Wagner, "Diffusion of Boron from Shallow Ion Implants in Silicon," *Journal of the Electrochemical Society ,* vol. 119, no. 11, pp. 1570-1576, 1972.

Appendix A

Published Paper

SCIENTIFIC REPORTS
nature research

OPEN

Design, fabrication, and optical characterization of one-dimensional photonic crystals based on porous silicon assisted by *in-situ* photoacoustics

Received: 10 June 2019
Accepted: 29 August 2019
Published online: 14 October 2019

Cristian Felipe Ramirez-Gutierrez[1,3], Harol David Martinez-Hernandez[2], Ivan Alonso Lujan-Cabrera[3] & Mario Enrique Rodriguez-García[4]

We present a methodology to fabricate one-dimensional porous silicon (PSi) photonic crystals in the visible range by controlled etching and monitored by photoacoustics. Photoacoustic can record *in-situ* information about changes in the optical path and chemical reaction as well as in temperature, refractive index, and roughness during porous layers formation. Radiometry imaging can determine the carrier distribution of c-Si substrate that is a fundamental parameter to obtain high-quality PSi films. An electrochemical cell was calibrated through a series of single PSi layers that allows knowing the PA amplitude period, porosity, and roughness as a function of the current density. Optical properties of single layers were determined using the reflectance response in the UV-Vis range to solve the inverse problem through genetic algorithms. PhC structures were designed using the transfer matrix method and effective media approximation.Based on the growth kinetics of PSi single layers, those structures were fabricated by electrochemical etching monitored and controlled by *in-situ* photoacoustics.

Nowadays, groundbreaking sensors are based on photonic crystals (PhC)[1], porous materials[2], and bio-inspired structures that allow accurate and reliable measures through its optical and electrical response[3–6]. Moreover, PhCs are fundamental components of other optoelectronic devices such as light emitting diodes (LEDs) and lasers. One of the promissory materials for these applications is porous silicon (PSi) thin films. PSi is a nanostructured and nanocomposite material with diverse porous morphology, different surface chemistry, and the enormous surface area, commonly obtained through electrochemical etching in hydrofluoric based (HF) aqueous media. The self-limited character of the PSi electrochemical reaction allows the fabrication of homogeneous films and heterostructures[7,8]. Besides, it is possible to custom PSi properties by changing the growing parameters, oxidation grade[9,10], and surface chemistry through functionalization[7,11,12]. This fact makes the PSi an excellent candidate to develop optical devices such as porous distributed Bragg reflector (DBR) and optical microcavities (OMC)[13,14]. However, the physicochemical properties of PSi are critically dependent on the etching parameters, and there are not theoretical models to predict the refractive index, absorption coefficient, thickness, porosity, and interfaces roughness. Nonetheless, *in-situ* methodologies based on infrared spectroscopy[15], laser interferometry[16–18], and photoacoustic[18–20] have been developed as an alternative to monitor the formation in real time of PSi thin films that allows feedback to control the electrochemical reaction.

[1]Posgrado en Ciencia e Ingenieŕia de Materiales, Centro de Física Aplicada y Tecnología Avanzada, Universidad Nacional Autónoma de México Campus Juriquilla, C.P., 76230, Qro., Mexico. [2]Programa de Física, Facultad de Ciencias Básicas y Tecnologías, Universidad del Quindío, Quindío, C.P., 630004, Colombia. [3]Ingeniería Física, Facultad de Ingeniería, Universidad Autónoma de Querétaro, C.P., 76010, Querétaro, Qro., Mexico. [4]Departamento de Nanotecnología, Centro de Física Aplicada y Tecnología Avanzada, Universidad Nacional Autónoma de México Campus Juriquilla, C.P., 76230, Qro., Mexico. Cristian Felipe Ramirez-Gutierrez and Mario Enrique Rodriguez-García contributed equally. Correspondence and requests for materials should be addressed to M.E.R.-G. (email: marioga@fata.unam.mx)

There are several reports about DBRs based on PSi and methods to fabricate tunable PSi thin films[21–25]. Vincent[21] manufactured DBR in the infrared range applying a square waveform of current density to produce a periodic structure of the PSi layer. These current profiles produced an interleaved high (η_H) and low (η_L) refractive index.

Some limitations were found related to the thickness of the layers, bandwidth, spectral position, and optical quality. Pavesi *et al.*[26] used the same methodology[21] but changed the etching time of the high refractive index film randomly. This means that the obtained DBR is, in fact, a random system. Setzu *et al.*[27] studied the optical properties of multilayered PSi system; they fabricated DBR using square waveform of current density selected arbitrary, and presented a methodology to control the interface roughness to improve the optical quality of PSi structures. Other works relate to applications of PSi DBR as chemical and biological sensors[28–30], and mirrors for photovoltaics devices[31,32]. Nevertheless, a common characteristic in the cited works is that the fabrication of the PSi DBRs always depends in using an arbitrary value of current density and etching time, resulting in a random optical response referred to the position of photonic band-gap, limited bandwidths, and low optical quality. This means that before producing the PSi DBR there was not a previous design or control. Therefore, it is imperative to mention that random devices are not related to quasi-periodic or disordered photonic structures[33–35]. The randomness is referred to as no certainty of optical properties at determined experimental fabrication conditions. For these reasons, the *in-situ* monitoring of the fabrication processes is needed to obtain reliable PSi devices. Therefore, intrinsic and extrinsic parameters must be taken into account to produce high quality and reproducible PSi devices. Extrinsic parameters are closely related to the fabrication methods of PSi films to obtain a tunable thicknesses, reflective index (porosity), and smooth interfaces. On the other hand, intrinsic parameters are associated with the substrate quality which is directly related to the carrier distribution, the crystalline quality, and the optothermal surface stability[36–38].

In this sense, there are few works about techniques that monitor the formation in real time of PSi films. Particularly interferometry and photoacoustic are non-contact and non-destructive techniques that can follow the etching rate, the evolution of thickness, porosity, and interfaces roughness in real time. However, the main limitation of interferometry is related to the monitoring of temperature during the chemical reaction; this is a crucial parameter because it changes the etching kinetics. As a solution for this limitation, this group has reported a differential photoacoustic system as well as a systematic study on following the PSi films formation[19,20]. The photoacoustic (PA) signal contains the information about the electrochemical reaction[20], optical, and thermal properties of layered systems[39–41]. Indeed, photoacoustic is an excellent technique to follow the fabrication process and reach tunable optical devices based on PSi. Therefore, this work is focused on establishing a methodology based on photoacoustic to monitor the DBR fabrication and a procedure to design and customize optical devices based on PSi such as DBRs and OMC. This means, the design and fabrication of PSi photonic structures at defined wavelength ranges.

According to this, this work shows key-points such as substrate quality, etching rate, porosity determination, and a model to determine the refractive index of porous media by using photoacoustic and effective medium approximation (EMA)[42–44] that are necessary to fabricate high-quality DBRs and OMC. Fabrication of tunable PSi thin films requires a previous determination of c-Si substrate quality. This can be done by using photocarrier radiometry spectroscopy (PCR) imaging. PCR is a non-contact, non-intrusive, and non-destructive technique that has been used for mapping the implant dose across the c-Si wafers[45–47] as well as to determine the carrier distribution in p and n Si wafers[48].

Thus, calibration of the electrochemical setup was performed. Then, a specific design of the device configuration was carried out, and finally, the fabrication monitoring and control processes are described. Figure 1 summarizes all steps followed that combine simulation, design, and experimental.

Results and Discussion

Substrate quality determination by PCR imaging. It is well known that c-Si wafers present non-homogeneous carrier distribution[36,49], and defects induced for the fabrications method and cleaving process. These can influence the PSi formation during the etching process given that the local magnitude of the electric field changes as a function of the position producing nonuniform porous nucleation. Usually, it is recommended to measure the nominal resistivity of the c-Si substrate[50], but it is an average value that does not give information about local variations of the carrier distribution. Figure 2a shows ten different areas from the central part of the wafer that were used to obtain the photocarrier images. Figure 2b shows the PCR amplitude for points 3 to 7 while the inset in this figure shows the changes in the phase for a point in these locations. The changes in the PCR amplitude around 1000 Hz have been associated with the changes in the minority carrier diffusion coefficient that are directly related to the carrier concentration[36,37]. It means that the wafer does not have a uniform carrier distribution. Moreover, the phase signal is not quite sensitive to the changes in the carrier distribution. Figure 2c shows the PCR amplitude of the ten regions across the wafer, red colors represent high carrier concentration while the blue ones can be associated with a decrease in the carrier concentration. These PCR images evidence the non-uniformity in the carrier distribution that has to affect any electrochemical process and porous distribution.

Etch calibration by *in-situ* photoacoustics. S1 calibration series was made to satisfied those criteria stablished for PCR imaging and Van der Pauw methods. The criteria ask for substrates with homogeneous carrier distribution and similar nominal resistivity. Mainly, it is considered a good quality substrate the one whose normalized PCR amplitude does not change more than 10% of the mean value such as those found in samples 3, 4, 7, 8, or 9 in Fig. 2c. On the other hand, sample 10 does not meet PCR criterion, so it is not used for further procedures. To verify the reproducibility of PA cycles, a second calibration series (S2) was performed.

The substrates that satisfied these conditions were selected to fabricate the calibration series. S1 and S2 are individual layers of PSi that were obtained upon varying the anodizing current density from 5 to 60 mA/cm^2.

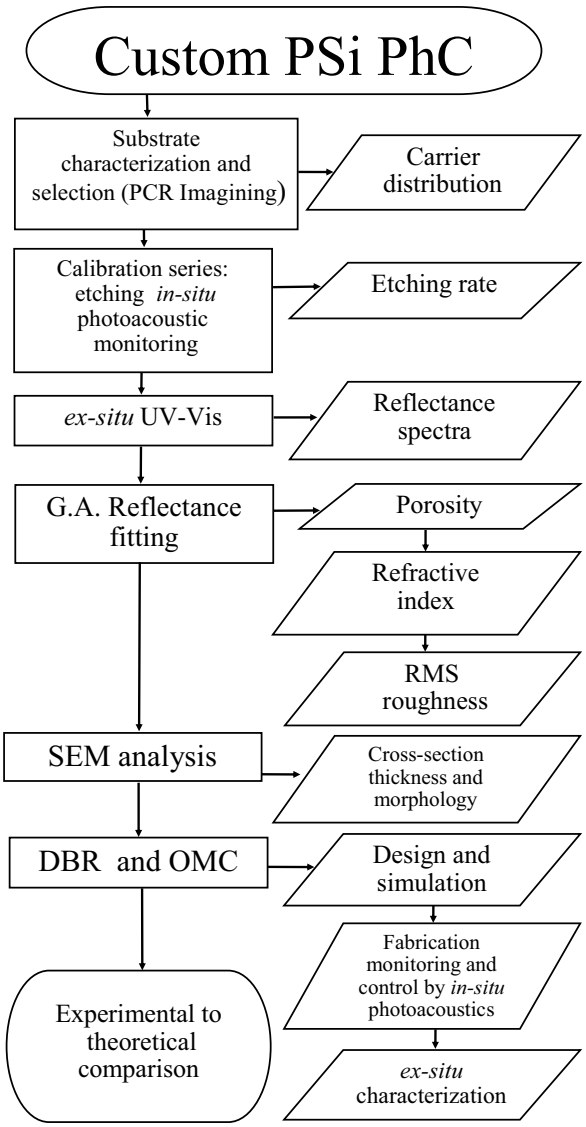

Figure 1. Flowchart of the procedures to design and fabricate PSi photonic crystals.

Each etching was monitored using a differential photoacoustic system[18], and temperature of the cell was kept at 25 °C. These series of individual layers were used as a calibration of the cell to obtain the of porosity, etching rate, photoacoustic cycle time, and interface roughness as a function of current density.

This technique allows controlling the etching time through the monitoring of PA cycles. In a previous publication of this group[19], we have proved how to estimate the porosity using the PA amplitude and the sample thickness measured by SEM. PA effect is produced by the absorption of modulated light (heat source) that produces a heat diffusion process. Moreover, the changes in the optical path, as a result of the formation of the porous film, make a self-modulation of the intensity of incident radiation (changes in the reflectance) that modules the PA effect. This modulation is periodic[19] and depends on the phase given for normal incidence by:

$$\delta(t, p) = \frac{2\pi\eta_i(p)d_i(t)}{\lambda}, \tag{1}$$

where $\eta_i(p)$ is the real part of the refractive index of the film that is porosity (p) dependent, d_i is the thickness film, and λ is the wavelength of the laser. The maximum of PA signal occurs when the reflectance of all the structure is a minimum, and it takes

place when:

$$\delta(t, p) = \left(m - \frac{1}{2}\right)\pi, \ \text{anti} - \text{reflective condition}. \tag{2}$$

Consequently, the minimum of the PA signal is reached in a maximum of reflectance when:

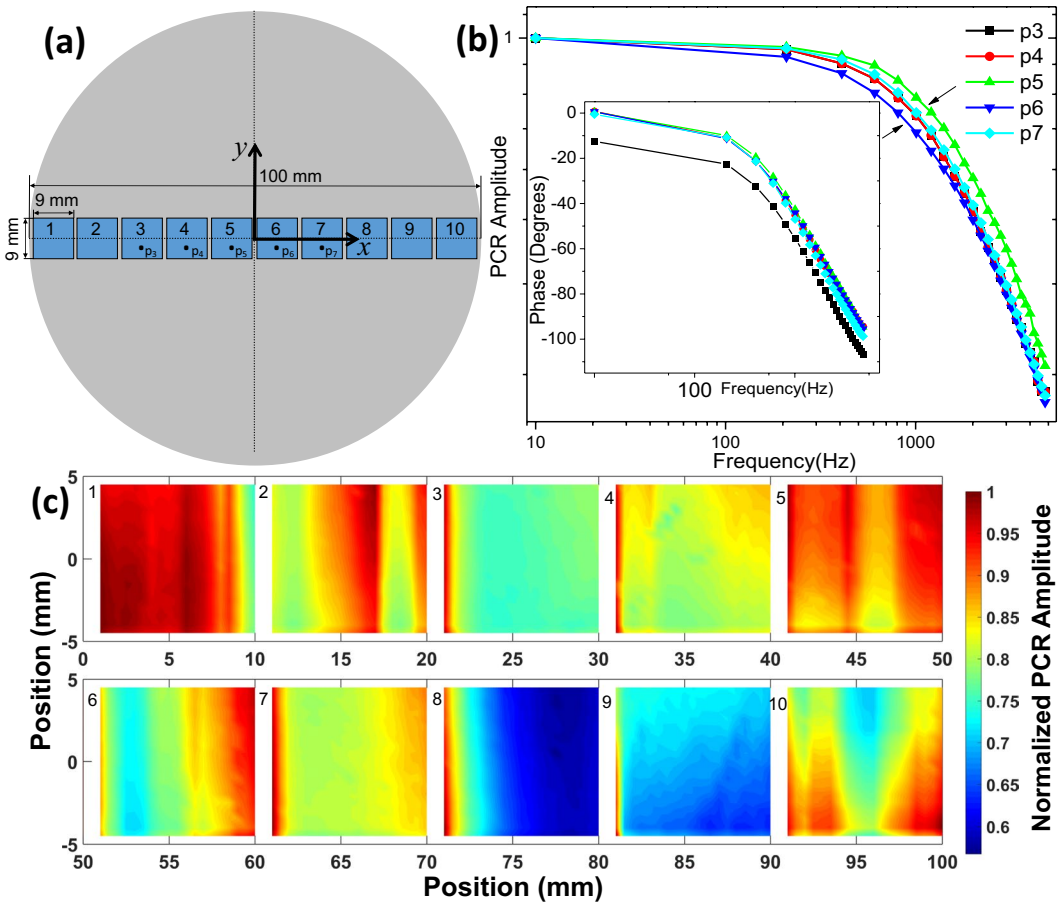

Figure 2. (**a**) Shows the silicon wafer and the scanned places by PCR. (**b**) PCR amplitude and phase of five points located at the center of the wafer. (**c**) Thermal images across the wafer. Laser beam radius 500 μm. Frequency 1 kHz.

$$\delta(t, p) = m\pi, \text{ reflective condition} \tag{3}$$

for $m = 1, 2, 3...$, that is related to the number of PA cycles. These conditions allow to determine the refractive index for λ_0 that is related to the porosity of the PSi film, if the thickness is known and PA amplitude signal ends in a local maximum or minimum (Eqs. 2 and 3).

Figure 3a shows the time of one PA cycle as a function of current density. As Eq. 1 shows, the increase of current density rises the etching rate and film porosity producing a reduction of the PA cycle. After that, reflectance spectra were measured and fitted by using genetic algorithms (GA) reported by Ramirez-Gutierrez[51–53] to determine simultaneously the effective porosity (Fig. 3b), interface roughness[54], and thickness using the Transfer Matrix Method (TMM).

Figures 3c,d show the interface roughness of air/PSi (σ_{01}) and PSi/Si substrate (σ_{12}) interfaces. This parameter is critically dependent on electrolyte composition and temperature. Only roughness values of less than 20 nm were found.

Porosity is usually determined by gravimetric analysis[55], but in this work, two methods to determine it as a function of current density were used (Fig. 3b). In the first one, the reflectance spectrum of every single film was fitted and compared with a simulated one using the refractive index calculated by Landau-Lifshitz-Looyenga (LLL) EMA rule[42–44]. The second was carried out using the anti-reflective condition on the PA signal (Eq. 2), and the thickness was determined by SEM. This shows that it is probable to obtain refractive index for λ_0 using Eq. 1, making possible to introduce this value in the LLL EMA to calculate the porosity. In order to achieve this, the refractive index of HF as 1.157[56] and ethanol 1.365 were used. There are some discrepancies in the porosity values (Fig. 3b). Nonetheless, it is well known that the porosity determined by optical methods is model dependent[31,57]. Besides, the roughness of PSi interfaces is critically reliant on electrolyte temperature and composition (HF/surfactant ratio)[27]. For the calibration series, the parameters electrolyte temperature and composition were retained constants. Moreover, layer thicknesses calculated by GA and the ones measured by SEM (Fig. 4) were close. Also, the etching rate was obtained using two methods: the PA methodology fitting the PA amplitude[20] and by direct calculation using the total etching time and the SEM thickness.

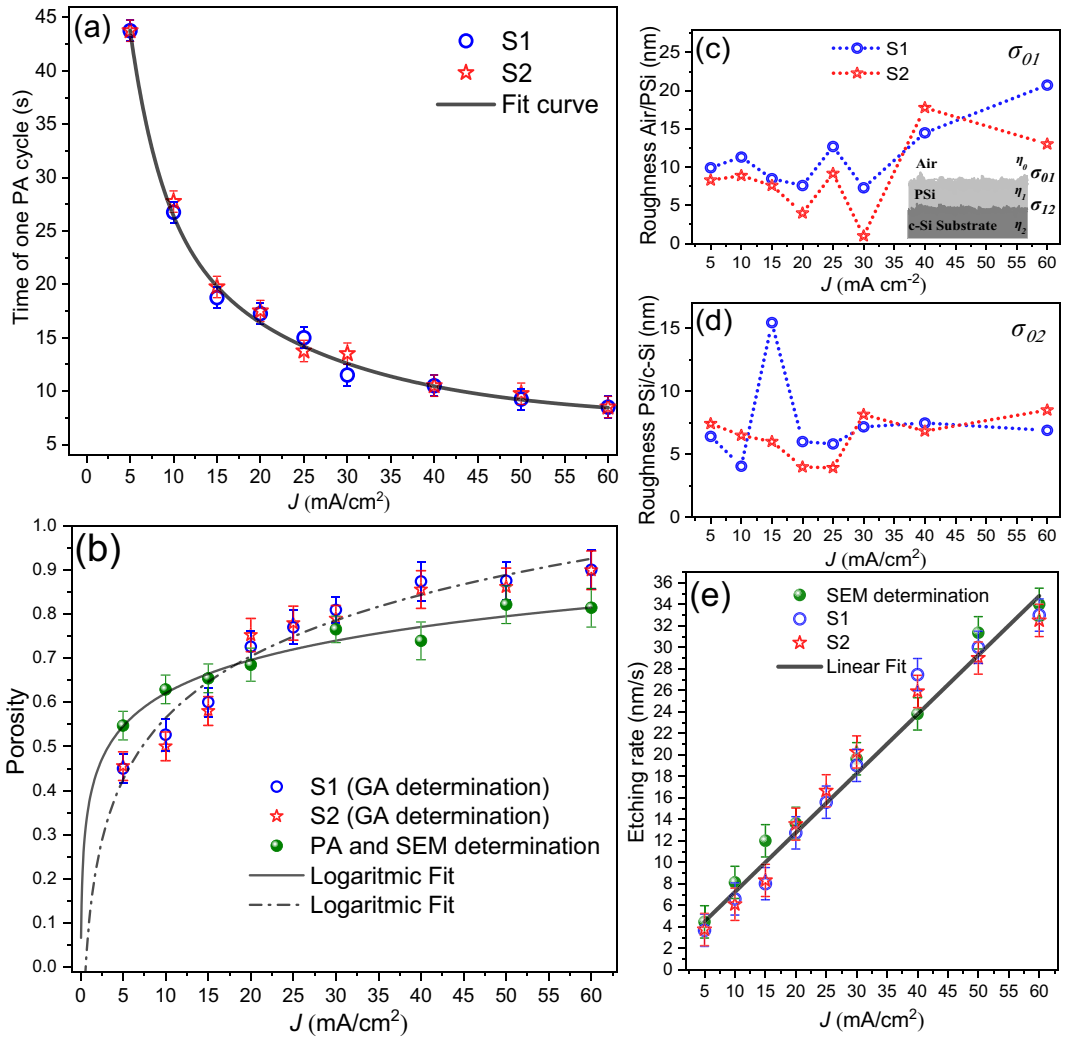

Figure 3. Calibration series parameters. (**a**) PA time as a function of current density that exhibits an exponential decay behavior. (**b**) Average porosity determined by GA and PA-SEM, (**c**) and (**d**) interface roughness as a function of current density determined by GA fitting of UV-Vis spectrum. (**e**) Etching rate that exhibits linear behavior.

Figure 3e shows the etching rate as a function of current density obtained through thickness obtained by GA and SEM divided by total anodizing time recorded by PA amplitude. As can be seen, the etching rate obtained by the two methods has a linear behavior from 5 to 60 mA/cm^2.

Figure 4 shows the cross section of some single films of the calibration series. It was observed in these images that porosity and etching rate increase as a function of the current density. Besides, all samples exhibited straight porous formation and interfacial roughness mainly in the interface PSi/substrate.

Design and simulation of photonic structures. The PSi based one-dimensional PhCs were designed using the quarter-wave condition[58] (Eq. 5), in which the optical thickness of each layer should be equal to a one-quarter of the central resonance wavelength (λ_0). Therefore, by controlling the refractive index and thickness of each layer is possible to design a customized PhC. Furthermore, it is worth noticing that the refractive index of c-Si has a plateau between 500 and 1450 nm, and it increases rapidly for values near to UV as the absorption coefficient does[59]. It means that it is recommendable to design PSi PhC in the plateau region. Thus, all photonic structures of this work were designed in the plateau refractive index region.

The PSi is a composite material, hence, its optical properties can be described as a mixture of dielectric functions (effective medium approximation), that in the case of PSi is a mixture of dielectric properties of c-Si host matrix ($\hat{\varepsilon}_M$) with incrustations within it of another material that full the pores ($\hat{\varepsilon}_1$) (some gas or liquid). The incrustations size with a dielectric function ($\hat{\varepsilon}_1$) in the majority system ($\hat{\varepsilon}_M$) must be comparable or less than the wavelength of the radiation that interacts with the medium. The LLL effective dielectric function[43,44] can be described as:

$$\hat{\varepsilon}_{ef}^{1/3} = \varepsilon_M^{1/3} + p(\hat{\varepsilon}_1^{1/3} - \hat{\varepsilon}_M^{1/3}) \quad (4)$$

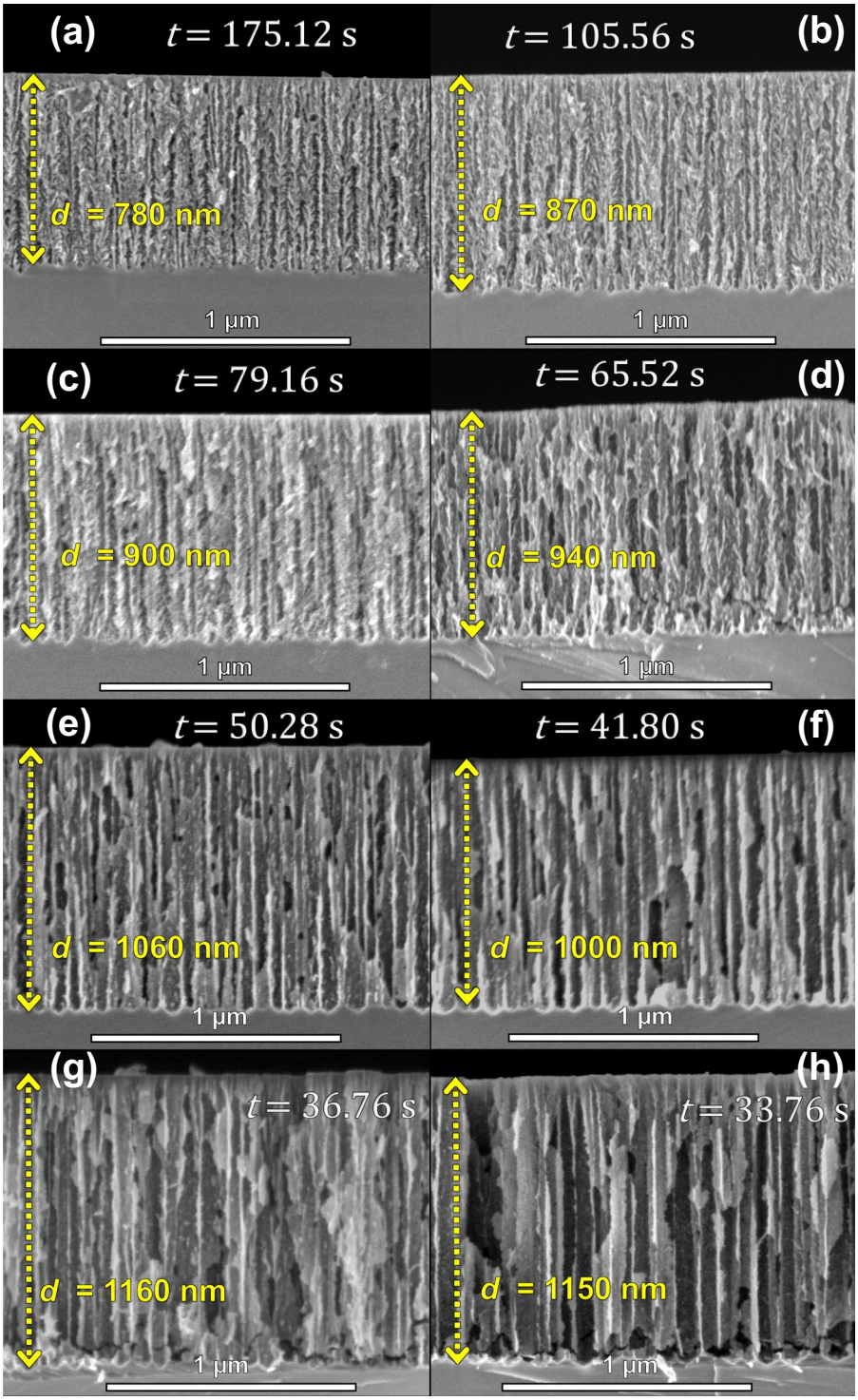

Figure 4. Cross-section SEM images of calibration series. (**a**) 5 mA/cm^2, (**b**) 10 mA/cm^2, (**c**) 15 mA/cm^2, (**d**) 20 mA/cm^2, (**e**) 30 mA/cm^2, (**f**) 40 mA/cm^2, (**g**) 50 mA/cm^2 and (**h**) 60 mA/cm^2. The images show the total anodizing time and thickness of each sample.

where p represents the porosity, $\hat{\varepsilon}_1$ corresponds to dielectric function of the incrustations, and $\hat{\varepsilon}_M$ represents the c-Si dielectric function. In particular, the porosification of c-Si reduces significantly the refractive index compared to the c-Si. This means that the values available of refractive index for PhC design are between the c-Si and the filling material (i.e. $\eta_S = 3.675$ and $\eta_0 \approx 1$ at 800 nm)[59].

For the DBRs and OMCs structures presented in this work, the reflectance is calculated through (TMM)[54,60]. As it is shown in Fig. 5, it is considered a stack of n alternating films with a high refractive index $\hat{N}_H = \eta_H + i\kappa_H$

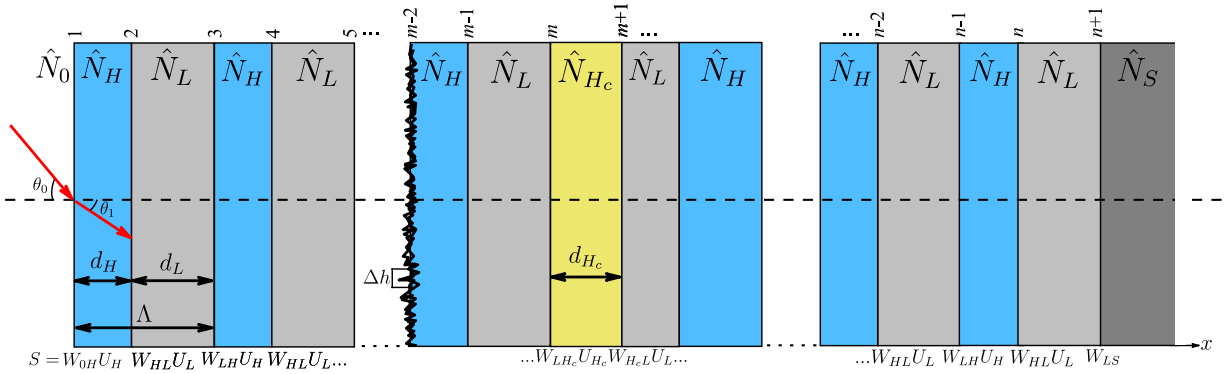

Figure 5. Schematic of the multilayer structure composed of n films that form $n + 1$ interfaces. The order of subscripts indicates the propagation direction.

and low refractive index $\hat{N}_L = \eta_L + i\kappa_L$ coupled to an incident media (air) with $\hat{N}_0 = \eta_0$, and a c-Si backing with $\hat{N}_S = \eta_S + i\kappa_S$. This structure contains $n + 1$ interfaces, and $\Lambda = d_H + d_L$ corresponds to the period of the structure. Each interface between two materials is represented by an admittance matrix $\mathbf{W}_{i,j}$ defined in terms of the optical admittance, which is a ratio of tangential components of the electric and magnetic fields amplitudes, and a phase matrix $\mathbf{U}_m$ that describes the action of the bulk. The product of all matrices resulting in the transfer matrix ($\mathbf{S}$) of the stack. Besides, this formalism allows introducing the effects produced by random irregularities (roughness) in each interface through the modified Fresnel coefficients. This approximation supposes that the interface irregularities are much smaller than the incident wavelength, i.e., $\Delta h\ \lambda$. Therefore, the description can be made by using the root mean square (RMS) roughness (σ_k) of each interface. The effect of the interface roughness in the optical response of photonic crystal was studied by Lujan-Cabrera *et al.*[54].

The DBR and OMC structures were designed fixing λ_0 and the stopband width $\Delta\lambda$. These parameters allow to obtain the thickness and refractive index of each layer by using the quarter-wave condition (Eq. 5).

$$\lambda_0 = 2(\eta_H d_H + \eta_L d_L), \tag{5}$$

To determine the stopband width was used the following expression:

$$\frac{\Delta\lambda}{\lambda_0} = \frac{\pi}{2}\left(\frac{1}{\cos^{-1}(\rho)} - \frac{1}{\cos^{-1}(\rho)}\right), \tag{6}$$

$$\rho = \frac{\eta_H - \eta_L}{\eta_H + \eta_L}, \tag{7}$$

where λ_0 is the central resonant wavelength or Bragg wavelength, η_H and η_L are the refractive indexes, d_H and d_L are the layer thickness (Fig. 5), and ρ is a refractive index ratio. The intensity, shape, and width of the stopband are also dependent on the number of periods of the structure. Considering these conditions (Eq. 5 and Eq. 7), refractive indexes are selected taking into account the desired bandwidth and stopband position, and these determine experimental parameters such as the current density and the etching time.

Three DBR prototypes were designed: the DBR550 is a structure designed near to the UV edge of plateau region with a stopband that does not contain the laser wavelength of PA setup. The DBR700 is a structure designed with a high refractive index contrast, this means a high contrast of layers porosity that produces a wide stopband. Also, PA laser wavelength is near to stopband in order to show the effect of the photonic bandgap formation over the PA signal. The DBR750 is a structure designed with a low refractive index contrast, this means a low contrast of layers porosity that produces a narrow-stopband. All DBRs are formed by 15 periods.

The OMC1 and OMC2 are PhC designed with the same conditions of DBR700 that includes a defective layer calculated by using the half-wavelength condition ($\eta_{Hc}\, d_c = \lambda_0/2$), and different sequences were explored to avoid the absorption effect of the first pair of layers and to obtain high Q-factor cavities. Table 1 presents the constants for the design of each PhC and its characteristics such as structure sequence, resonant wavelength, and stopband width. These values were used to simulate the reflectance spectrum using the TMM.

Fabrication and characterization of photonic structures. The first step was to select c-Si substrates with a homogeneous carrier distribution tested by PCR and Vander Pow method. This guaranteed the substrate quality. The refractive index, determined by the design (Table 1), fixes the porosity according to EMA theory[43,44]. At the same time, the porosity defines the current density for the etching process. These values were selected from the calibration series (Fig. 3b). The next step was to calculate the etching time using the value of the etching rate (Fig. 3d). Consequently, all the parameters mentioned above defined the photoacoustic profile that was used as a control parameter for the etching.

Table 2 shows the anodization time ($t_{H,L}$) and current density ($J_{H,L}$) for each layer of PhC, where the indices H and L indicate the high and the low refractive index layer respectively. Also, it shows the experimental values

Structure	DBR550	DBR700	DBR750	OMC1	OMC2
sequence	$(HL)^{15}S$	$(HL)^{15}S$	$(HL)^{15}S$	$(HL)^{3}H_{c1}\,(HL)^{3}S$	$(HL)^{3}H_{c2}\,(LH)^{6}S$
λ_0(nm) (simulated)	550	700	750	700	700
$\Delta\lambda$ (nm) (simulated)	78	164	66	311	235
η_H	1.45	1.73	2.26	1.73	1.73
η_L	1.16	1.20	1.97	1.20	1.20
η_{Lc}	—	—	—	2.10	1.73
d_H (nm)	95	102	83	102	102
d_L(nm)	131	146	96	146	146
d_{Hc} (nm)	—	—	—	330	167

Table 1. Constants for the design of the photonic PSi structures.

Structure	DBR550	DBR700	DBR750	OMC1	OMC2
Sequence	$(HL)^{15}S$	$(HL)^{15}S$	$(HL)^{15}S$	$(HL)^{3}H_{c1}\,(HL)^{3}S$	$(HL)^{3}H_{c2}\,(LH)^{6}S$
Etching parameters					
$t_H \pm 0.05$ (s)	6.03	16.87	13.20	16.87	12.28
$t_L \pm 0.05$ (s)	4.40	4.25	8.20	4.25	4.25
t_{Lc} 0.05 (s)	—	—	—	97.25	24.69
J_H (mA/cm^2) ± 0.01	25	7.21	10	7.21	7.21
J_L (mA/cm^2) ± 0.01	60	58.48	20	58.48	58.48
J_{Hc} (mA/cm^2) ± 0.01	—	—	—	4.42	7.21
Obtained parameters					
λ_0 (nm) (experimental)	572	725	764	700	707
$\Delta\lambda$ (nm) (experimental)	64	140	67	293	232
$p_H \pm 0.01$	0.75	0.68	0.57	0.68	0.68
$p_L \pm 0.01$	0.92	0.91	0.70	0.91	0.91
$p_c \pm 0.01$	—	—	—	0.55	0.68
d_H (nm)	90 ± 5	107 ± 8	110 ± 8	107 ± 6	100 ± 5
d_L (nm)	140 ± 9	143 ± 7	122 ± 8	143 ± 7	143 ± 7
d_{Hc} (nm)	—	—	—	335 ± 5	168 ± 7
$^{\sigma}HL$	15	20	12	20	20

Table 2. Etching conditions and experimental parameters obtained for PSi PhCs. The thickness of each layer represents an average values determined by SEM. The porosity and roughness were determined by GA. The spectral position and bandwidth were determined by the reflectance spectrum analysis.

obtained for the layer porosity, thickness and roughness, and PhC resonance wavelength and stopband width. On the other hand, the PSi photonic structures present interfacial roughness inherently impacting in the optical quality. The roughness contribution at internal faces (H/L and L/H) has more impact on the optical quality than the first interface (Air/DBR) and the last one (DBR/substrate). Thus, Table 2 reports a roughness value of internal faces determined by GA and SEM. The previous works done by this group[18–20] showed that the PA cycle observed during the PSi formation depends on refractive index, porosity, etching rate, and laser wavelength (Eq. 1), and the etching rate is almost constant for short anodizing times. Thus, each frequency component of PA signal is related to a single film formation. In order to obtain good control of the formation process, it was designed a selected layer thickness in which anodizing times were half multiplies of PA cycles. This means a minimum or a maximum to obtain symmetric cycles that is the case of samples DBR550 and DBR700. If the etching time does not satisfy this condition, the PA signal will have a beat behavior. Hence, the PA amplitude contains all frequency components of the etching rate of PSi films formation.

Figure 6 shows the *in-situ* PA signal for each designed DBRs as well as their cross-sectional SEM images. For the DBR550 (Fig. 6a) and DBR700 (Fig. 6c), the etching time was set as half of one PA cycle for the corresponding current density (see Table 2). Thus, a entire period in the PA signal represented a pair of *HL* layers. The porosity ratio between *H* and *L* allows clear identification of each layer as is shown in Fig. 6b,d. Furthermore, all interfaces exhibited roughness.

In the case of DBR550, the bandgap was centered at 550 nm and its bandwidth was 64 nm, so it did not reflect the wavelength (808 nm) of the laser that produces the PA effect. Therefore, the PA amplitude decreased only when the optical path increased. For DBR700 the PA amplitude decreased fast, even the PA periods disappeared after the formation of eleven pair of layers. This is an expected result given that the optical bandgap was near to the laser wavelength. This means that the most fraction of the incident radiation was reflected and the PA effect disappeared.

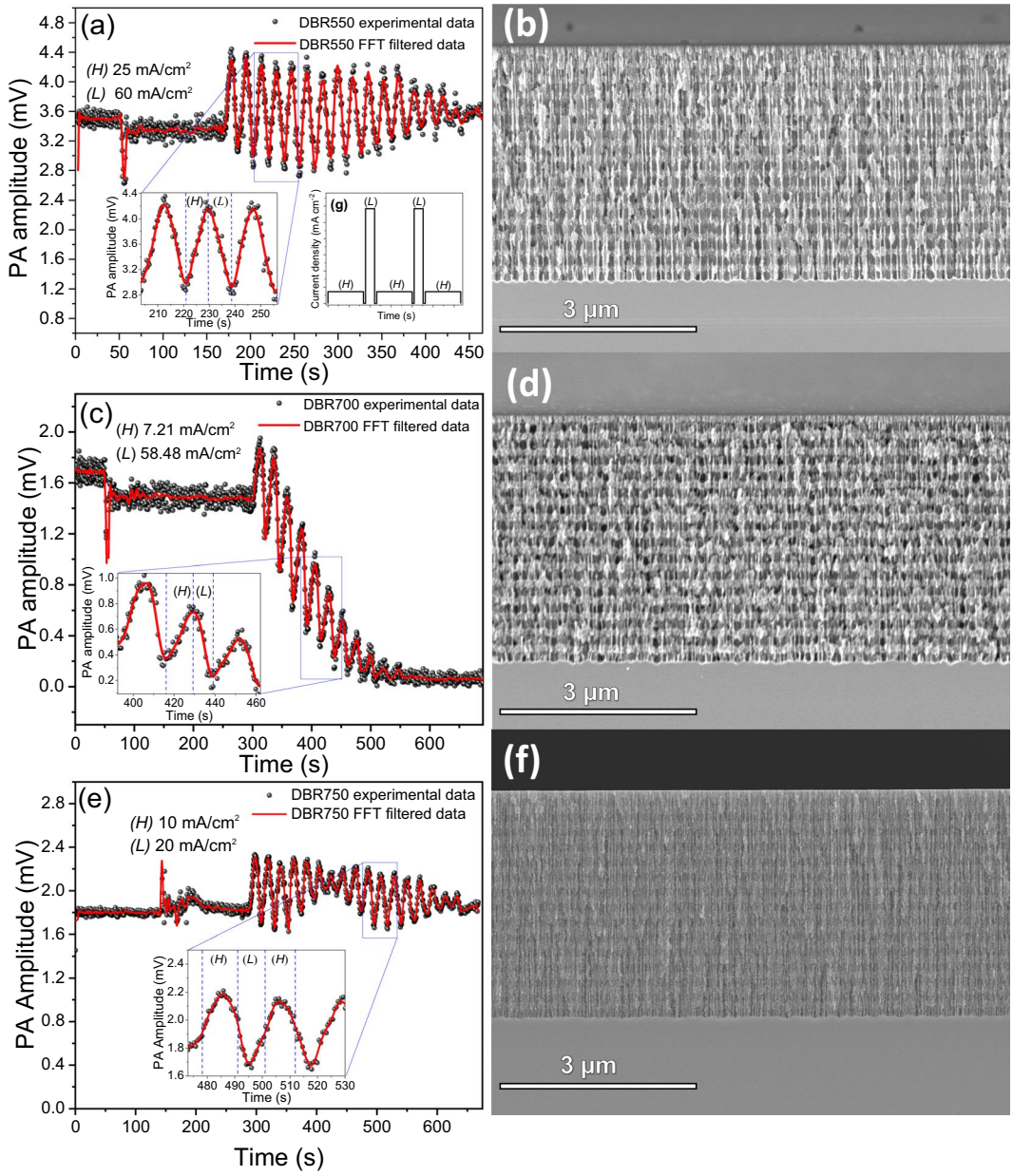

Figure 6. PA amplitude during DBRs fabrication. (**a**) DBR550, (**c**) DBR700, (**e**) DBR750. (**b**,**d**,**f**) are its corresponding cross-sectional SEM images. Inset (**g**) shows the current density profile used for DBRs fabrication. Insets in (**a**,**c**,**e**) correspond to a zoomed view of PA amplitude where dashed blue lines define each layer formation.

DBR750 PA signal in Fig. 6e corresponds to a beat profile since the etching time of each layer is not an integer multiple of a half PA period. For this reason, one period does not correspond to a pair of layers. However, PA amplitude frequency components allow the control of the etching process because the frequency associated with each layer is well known. DBR750 was designed with low porosity ratio and current densities that produce low contrast in the stack cross-sectional SEM image. Even though, the stack conformation is appreciable.

Measured and simulated reflectance spectra of DBRs are presented in Fig. 7, and the obtained structural and optical parameters are summarized in Table 2. All DBRs display redshifts and bandwidth narrowing compared with the simulated ones. These are due to parasite capacitance in the stack structure and the electrochemical circuit[61,62] which the current source cannot control. Consequently, the discharge process held the etching during a short time generating layers thickness higher than the designed ones. Nonetheless, the deviation in the thickness of the layers, related to the designs, was around 15 nm that produced a redshift in the stopband position proportional to the optical path.

Figure 8a,c shows the PA amplitude signals, and insets represent the current profile used to fabricate the OMCs. Figure 8b,d shows the cross-sectional SEM images for the OMCs. OMC1 and OMC2 were manufactured using the same conditions of DBR700, this means that it was introduced a defective layer into the DBR700

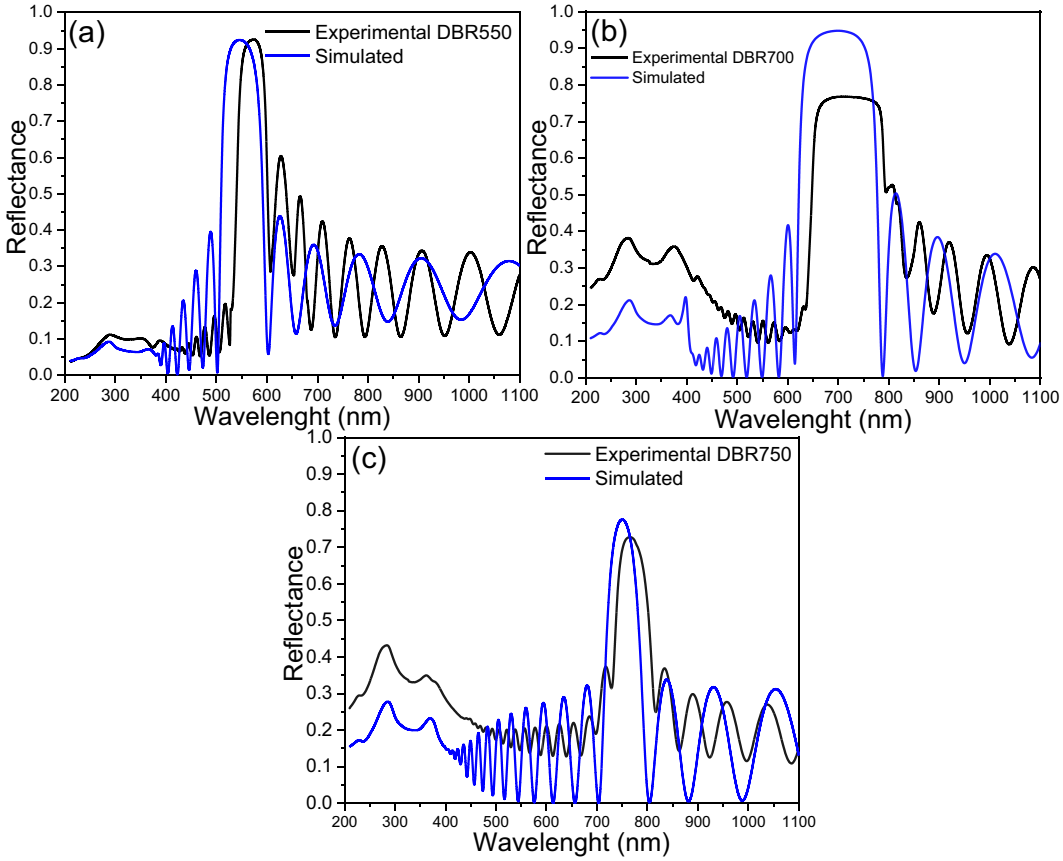

Figure 7. Reflectance spectra simulated (blue line) and measured (black line) for (**a**) DBR550, (**b**) DBR700, and (**c**) DBR750.

structure. The experimental parameters used for OMCs fabrication are summarized in Table 2. The OMC1 stack was designed as $(HL)^3H_{c1}\ (HL)^3S$ sequence. In the micrograph (Fig. 8b), given that the current density used for the defective layer is near to the used one for *H* layer, there is no porosity contrast to differentiate *H* to H_{c1} layer, and it looks like a thick one. However, PA amplitude clearly shows the formation of a defective layer that corresponds to two PA cycles. The defective layer was designed with a thickness of 335 nm to make two cavities into the bandgap located at 650 and 787 nm. OMC2 (Fig. 8c,d was designed as $(HL)^3H_{c2}\ (LH)^6S$ sequence with a defective layer of 168 nm that produces a microcavity (MC) at 668 nm. This sequence was selected to improve the reflectance percentage keeping the cavity depth. Clearly, the PA signal shows the formation of each *HL* pair of layers and the defective layer.

Likewise, in this stack, the sequence after the formation of defective layers is inverted, and it is appreciable in PA amplitude signal. In both OMCs the PA amplitude is sensitive to the photonic gap formation which is evidenced by the quickly signal attenuation. Figure 9 shows the reflectance spectrum of each OMC manufactured. Figure 9a corresponds to OMC1, and it is well appreciable the formation of two MC located at 649 and 783 nm with an FWHM about 27 and 32 nm respectively, that corresponds to a relatively high Q-factor. Shifts of 1 and 4 nm were produced for each MC compared with the simulation design, respectively. Fig. 9b corresponds to OMC2 and the MC is located at 672 nm, this means that a redshift of 4 nm was produced compared with the designed one. Moreover, the sequence of OMC2 improved the Q-factor whose FWHM is 16 nm. In both OMCs, a diminution is observed in the depth of the MC that is caused by the interface roughness of the stack[55].

Tolerance fabrication. The etching rate of c-Si in HF-based media was not constant for long etching times[18,20], and the films presented porosity gradients as a function of depth[10,23]. Also, the electrolyte composition changed because of the chemical species released during the etching[7]. Furthermore, the silicon-electrolyte interface presented an inherent capacitance[61] that could store enough charge to continue the etch even if the current supply was off. This effect produced layers thicker than the designed ones and generated a redshifted in the reflectance spectrum. This effect can be reduced if the current density decreases monotonously as a function of the time to compensate the remnant charges. Another alternative is to reduce the etching time. Nevertheless, in this work, and others related, PSi optical devices always presented deviations respect to the design ones. This is mainly attributed to the substrate quality and random fluctuations during the PSi formation. Hence, it is introduced the tolerance fabrication as a term related to the possible deviations of the optical response of the devices. In this work, we found a redshift in DRBs about 30 nm associated with layers ticker than the designed ones. In this case, the average reflectance shift was the layer thickness deviation times the refractive index. In the case of

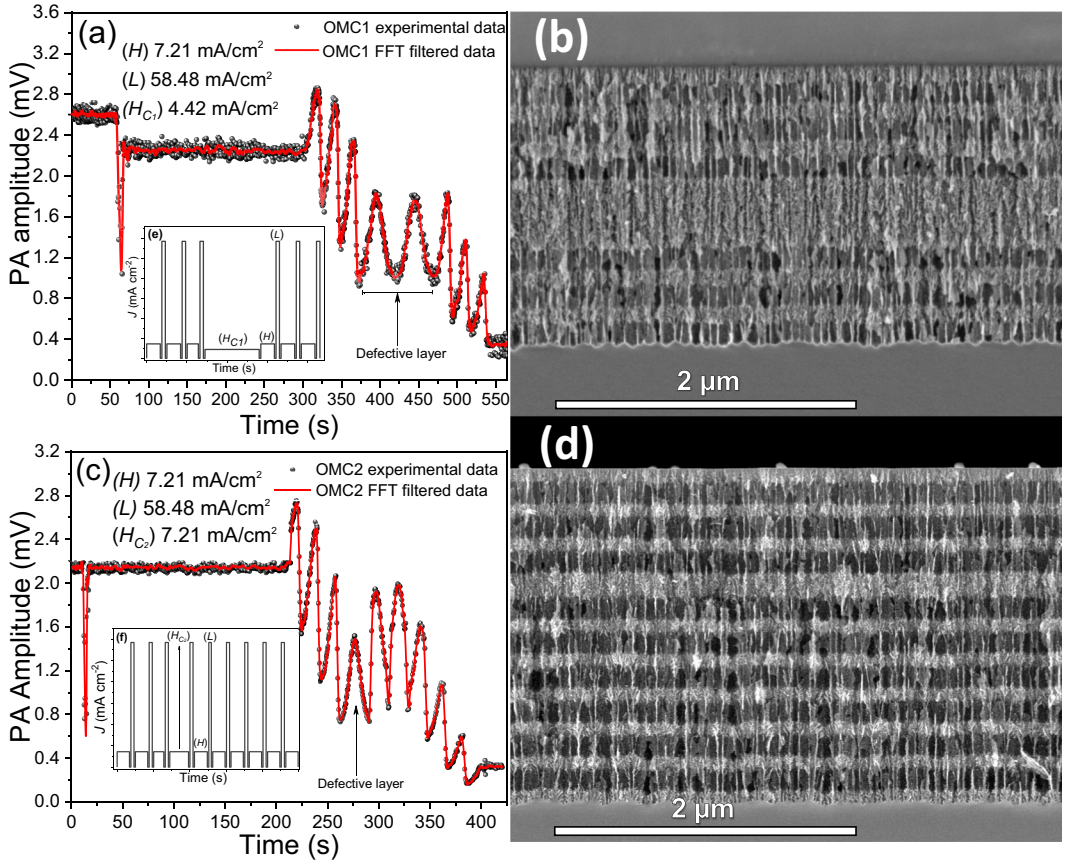

Figure 8. PA amplitude during OMC fabrication. (**a**) OMC1, (**c**) OMC2, and its respective SEM cross-sectional images (**b**,**d**). Insets (**e**,**f**) correspond to the current profiles used for OMC1 and OMC2 fabrication respectively.

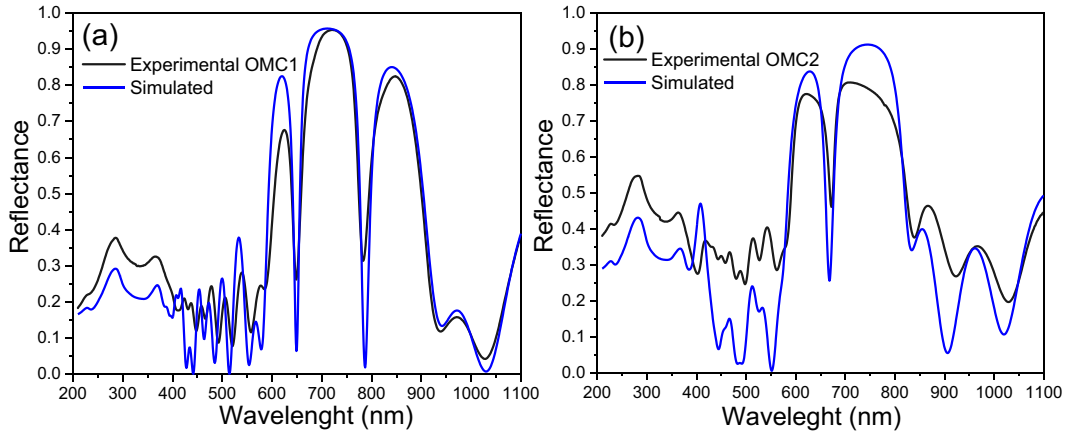

Figure 9. Reflectance spectra simulated (blue line) and measured (black line) of (**a**) OMC1 and (**b**) OMC2.

OMCs, the main effect was observed in the Q-factor that is affected by the interface roughness. Several works have reported PhCs based on PSi in the infrared region, which means that the thickness of the layers (optical path) is higher than those for PhC in the visible spectrum as is our case. Thus, deviations in layer thickness because of the intrinsic capacitance has more height on the optical response for the PhC designed in the visible region, usually a redshift.

Conclusions

In this work was presented a complete methodology to design, fabricate, and characterize PSi one-dimensional PhC using *in-situ* photoacoustic as a monitor and control technique. The critical parameters that influence the PSi formation are the substrate quality, that is related to the carrier distribution along the wafer as was showed by

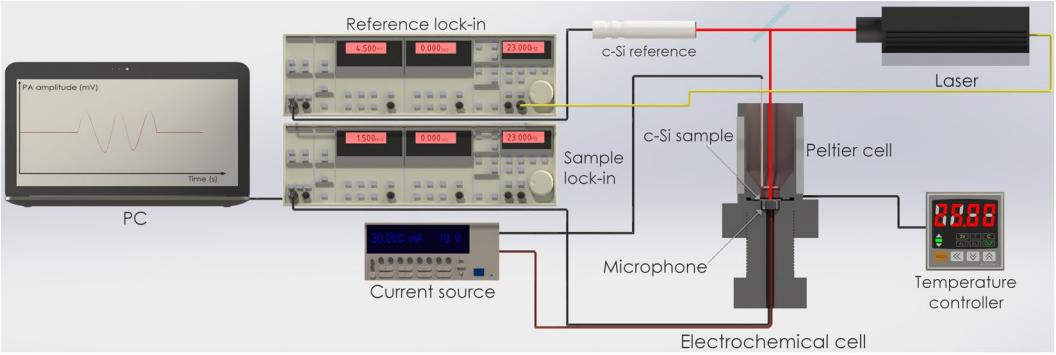

Figure 10. A stylized representation of the experimental electrochemical and photoacoustic setup used for PSi PhC fabrication. The surface samples were illuminated by a laser (808 nm) with square-wave modulated intensity. The Lock-In amplifiers and the current source were controlled using the GPIB card and software developed in Matlab (MathWorks, Inc.).

photocarrier radiometry images as well as the control of the electrolyte composition and reaction temperature. The first step of this methodology consisted of the substrate quality determination to select pieces of c-Si with carrier homogeneity. The second step was the etching cell calibration by using photoacoustic that allowed knowing the behavior of manufacture parameters as a function of the current density to control the PSi formation. After that, simulation and design using the TMM and EMA formalisms were carried out to determine the manufacturing process of the customized devices. Finally, the fabrication was made with real-time monitoring and control using photoacoustic that can detect *in-situ* any deviation or unexpected event that could interfere in the formation process. The experimental results showed that electrochemical etching of c-Si in HF media is dependent on multiple parameters and each one plays a synergy role with others, i.e., the electrolyte composition and temperature in the interface roughness, carrier distribution and current density in the etching rate. Therefore, natural deviations in the morphology, such as layer thickness and porosity, produced variation in the optical response showed in the redshift compared with the ideal simulated device. SEM images and reflectance spectra showed clearly that this methodology allows the fabrication of reproducible DBRs and OMCs photonic devices with high accuracy. This methodology is a versatile technique that provides adequate real-time control in the optical path of multilayered systems that can be explored and implemented to monitor and control other thin films fabrication techniques such as vapor deposition, spin coating, or epitaxy.

Methods

Materials. Boron-doped monocrystalline c-Si wafers by Pure Wafer company with (p^{++}) with 0.001 Ω cm of resistivity, (100) crystalline orientation, and single polish was used as a substrate. Deionized water, ammonium hydroxide solution (NH_4OH wt 29%), and hydrogen peroxide (H_2O_2) supplied by Sigma-Aldrich were used for RCA cleaning process of c-Si substrates. Hydrofluoric acid (HF wt 48%) and ethanol (C_2H_5OH wt 99.98%) provided by Sigma-Aldrich were used for preparing the electrolyte used in this study. A platinum wire (99%) was used as a counter electrode. A total of 23 samples were prepared for these experiments.

Sample Anodizing. Figure 10 shows the etching and PA setup that consists of an electrochemical cell coupled to an open photoacoustic cell and an external (acoustic) cell as a reference. This configuration allows comparing the reference signal with the one obtained from the anodized sample, this reduces the noise from external sonic sources and improves the signal to noise ratio.

The PA setup is composed by a container that holds the electrolyte solution. A screw is used to set the microphone and the c-Si sample, and to seal the holder. An 808 nm laser line (<200 mW of power by Laser-Mate Group) modulated at 23 Hz is used as an excitation source. The laser was split by using a 60/40 beam splitter and the transmitted and reflected beams were focused on a c-Si external reference and on a c-Si sample respectively. Two electret condenser microphones were located at the back of c-Si samples; the microphones were polarized using a 9 V DC battery A Pt wire and a Cu ring were used as a counter electrode and as a collector respectively. The cell temperature was kept at 25 C using Peltier cells regulated by a PID controller.

PSi was prepared by electrochemical etching in an electrolyte solution composed of HF and ethanol in a 3:7 volumetric ratio. The anodization current profiles were created using a precision Keithley current source (6220). During the etching, the photo-induced acoustic signals (amplitude and phase) were recorded using a Stanford Research SR830 Lock-In Amplifiers and GPIB-USB-HS (National Instruments) acquisition card. The cell was calibrated through two sample series (S1 and S2), each one composed by 9 samples anodized at 5, 10, 15, 20, 25, 30, 40, 50, and 60 mA/cm^2. Three DBRs and two OMCs were anodized using current density values determined by the calibration series, and the etching time was monitored and controlled by the feedback of the PA amplitude. A total of 23 c-Si samples were used in the experiments.

Sample characterization. The carrier distribution of c-Si substrates was characterized by using PCR implementing the methodology proposed by Mandelis and Rodriguez-Garcia[37,46,49]. An InGaAs infrared detector with spectral range 0.8–1.8 μm, and a laser 532 nm was modulated from 10 to 5000 Hz. PCR images were taken at

1 kHz with a step size 100 μm, and spot size of 40 μm in the linear regimen[36]. Each image was taken in a 9 9 mm square and a 1 mm gap between areas.

Morphological characterization of PSi stacks was carried out with a high-resolution scanning electron microscope (Hitachi SU8230) employing secondary electron imaging operated at 1 kV. Reflectance measurements were conducted with a PerkinElmer Lambda 35 spectrophotometer in the near-specular (6°) configuration in a spectral range of 200–1100 nm.

References

1. Yablonovitch, E. Photonic crystals. *J. Mod. Opt.* **41**, 173–194, https://doi.org/10.1080/09500349414550261 (1994).
2. Innocenzi, P., Malfatti, L. & Soler-Illia, G. J. A. A. Hierarchical mesoporous films: From self-assembly to porosity with different length scales. *Chem. Mater.* **23**, 2501–2509, https://doi.org/10.1021/cm200050r (2011).
3. Inan, H. *et al*. Photonic crystals: Emerging biosensors and their promise for point of care applications. *Chem. Soc. Rev.* **46**, 366–388, https://doi.org/10.1039/C6CS00206D (2017).
4. Hernandez-Montelongo, J. *et al*. Nanostructured porous silicon: The winding road from photonics to cell scaffolds. a review. *Front. Bioeng. Biotechnol.* **3**, 60, https://doi.org/10.3389/fbioe.2015.00060 (2015).
5. Rasson, J., Poncelet, O., Mouchet, S. R., Deparis, O. & Francis, L. A. Vapor sensing using a bio-inspired porous silicon photonic crystal. *Mater. Today Proc.* **4**, 5006–5012, https://doi.org/10.1016/j.matpr.2017.04.107 (2017).
6. Hu, S. *et al*. Experimental realization of deep-subwavelength confinement in dielectric optical resonators. *Sci. Adv.* **4**, https://doi.org/10.1126/sciadv.aat2355 (2018).
7. Föll, H., Christophersen, M., Carstensen, J. & Hasse, G. Formation and application of porous silicon. *Mater. Sci. Eng., R* **39**, 93–141, https://doi.org/10.1016/S0927-796X(02)00090-6 (2002).
8. Kolasinski, K. W. Etching of silicon in fluoride solutions. *Surf. Sci.* **603**, 1904–1911, https://doi.org/10.1016/j.susc.2008.08.031 (2009).
9. Ocier, C. R., Krueger, N. A., Zhou, W. & Braun, P. V. Tunable visibly transparent optics derived from porous silicon. *ACS Photonics* **4**, 909–914, https://doi.org/10.1021/acsphotonics.6b01001 (2017).
10. Huanca, D. R., Ramirez-Fernandez, F. J. & Salcedo, W. J. Porous silicon optical cavity structure applied to high sensitivity organic solvent sensor. *Microelectron. J.* **39**, 499–506, https://doi.org/10.1016/j.mejo.2007.07.025 (2008).
11. Sahare, P., Ayala, M., Vazquez-Duhalt, R. & Agrawal, V. Immobilization of peroxidase enzyme onto the porous silicon structure for enhancing its activity and stability. *Nanoscale Res. Lett.* **9**, 409, https://doi.org/10.1186/1556-276X-9-409 (2014).
12. Martin, M. *et al*. Effect of surface functionalization of porous silicon microcavities on biosensing performance. *J. Nanophotonics* **6**, 1–12, https://doi.org/10.1117/1.JNP.6.061506 (2012).
13. Do, T. C. *et al*. A microcavity based on a porous silicon multilayer. *Adv. Nat. Sci: Nanosci. Nanotechnol* **2**, 035001, https://doi.org/10.1088/2043-6262/2/3/035001 (2011).
14. Pacholski, C. Photonic crystal sensors based on porous silicon. *Sensors* **13**, 4694–4713, https://doi.org/10.3390/s130404694 (2013).
15. Rao, A. V., Ozanam, F. & Chazalviel, J. N. *In situ* fourier-transform electromodulated infrared study of porous silicon formation: Evidence for solvent effects on the vibrational linewidths. *J. Electrochem. Soc.* **138**, 153–159, https://doi.org/10.1149/1.2085526 (1991).
16. Steinsland, E., Finstad, T. & Hanneborg, A. Laser reflectance interferometry for *in situ* determination of silicon etch rate in various solution. *J. Electrochem. Soc.* **146**, 3890–3895, https://doi.org/10.1149/1.1392568 (1999).
17. Foss, S. E., Kan, P. Y. Y. & Finstad, T. G. Single beam determination of porosity and etch rate in situ during etching of porous silicon. *J. Appl. Phys.* **97**, 114909, https://doi.org/10.1063/1.1925762 (2005).
18. Ramirez-Gutierrez, C. F., Castaño-Yepes, J. D. & Rodriguez-Garcia, M. E. Optical interferometry and photoacoustics as *in-situ* techniques to characterize the porous silicon formation: A review. *Open Mater. Sci.* **4**, 23–32, https://doi.org/10.1515/oms-2018-0003 (2018).
19. Ramirez-Gutierrez, C. F., Castaño-Yepes, J. D. & Rodriguez-García, M. E. *In situ* photoacoustic characterization for porous silicon growing: Detection principles. *J. Appl. Phys.* **119**, 185103, https://doi.org/10.1063/1.4948946 (2016).
20. Ramirez-Gutierrez, C. F., Castaño-Yepes, J. D. & Rodriguez-García, M. E. Modeling the photoacoustic signal during the porous silicon formation. *J. Appl. Phys.* **121**, 025103, https://doi.org/10.1063/1.4973940 (2017).
21. Vincent, G. Optical properties of porous silicon superlattices. *J. Appl. Phys.* **64**, 2367–2369, https://doi.org/10.1063/1.111982 (1994).
22. Hulkkonen, H. H., Salminen, T. & Niemi, T. Block copolymer patterning for creating porous silicon thin films with tunable refractive indices. *ACS Appl. Mater. Interfaces* **9**, 31260–31265, https://doi.org/10.1021/acsami.6b16110 (2017).
23. Caballero-Hernández, J. *et al*. Fabrication of optical multilayer devices from porous silicon coatings with closed porosity by magnetron sputtering. *ACS Appl. Mater. Interfaces* **7**, 13889–13897, https://doi.org/10.1021/acsami.5b02356 (2015).
24. Nava, R., de la Mora, M. B., Tagüeña-Martínez, J. & del Río, J. A. Refractive index contrast in porous silicon multilayers. *Phys. Status Solidi C* **6**, 1721–1724, https://doi.org/10.1002/pssc.200881090 (2009).
25. Estrada-Wiese, D. & del Río, J. A. Refractive index evaluation of porous silicon using bragg reflectors. *Rev. Mex. Fis.* **64**, 72–81, https://doi.org/10.31349/RevMexFis.64.72 (2018).
26. Pavesi, L. & Dubos, P. Random porous silicon multilayers: Application to distributed bragg reflectors and interferential fabry - pérot filters. *Semicond. Sci. Technol.* **12**, 570, https://doi.org/10.1088/0268-1242/12/5/009 (1997).
27. Setzu, S., Ferrand, P. & Romestain, R. Optical Properties of Multilayered Porous Silicon. *Mater. Sci. Eng. B.* **69–70**, 34–42, https://doi.org/10.1016/S0921-5107(99)00261-5 (2000).
28. Kim, H. J., Kim, Y. Y. & Lee, K. W. Multiparametric sensor based on dbr porous silicon for detection of ethanol gas. *Curr. Appl. Phys.* **10**, 181–183, https://doi.org/10.1016/j.cap.2009.04.020 (2010).
29. Tsai, W. T. *et al*. ppb-level heavy metal ion detection by electrochemistry-assisted nanoporous silicon (eca-nps) photonic sensors. *Sens. Actuators, B* **265**, 75–83, https://doi.org/10.1016/j.snb.2018.01.232 (2018).
30. Caroselli, R. *et al*. Real-time and in-flow sensing using a high sensitivity porous silicon microcavity-based sensor. *Sensors* **17**, https://doi.org/10.3390/s17122813 (2017).
31. Estrada-Wiese, D. *et al*. Staggered padé wavelength distribution for multi-bragg photonic mirrors. *Sol. Energy Mater. Sol. Cells* **141**, 315–321, https://doi.org/10.1016/j.solmat.2015.05.048 (2015).
32. de la Mora, M., Jaramillo, O., Nava, R., Tagüeña-Martínez, J. & del Río, J. Viability study of porous silicon photonic mirrors as secondary reflectors for solar concentration systems. *Sol. Energy Mater. Sol. Cells* **93**, 1218–1224, https://doi.org/10.1016/j.solmat.2009.01.007 (2009).
33. Wiersma, D. S. Disordered photonics. *Nat. Photonics* **7**, 188–196, https://doi.org/10.1038/nphoton.2013.29 (2013).
34. Bellingeri, M., Kriegel, I. & Scotognella, F. One dimensional disordered photonic structures characterized by uniform distributions of clusters. *Opt. Mater.* **39**, 235–238, https://doi.org/10.1016/j.optmat.2014.11.033 (2015).
35. Bellingeri, M., Chiasera, A., Kriegel, I. & Scotognella, F. Optical properties of periodic, quasi-periodic, and disordered one-dimensional photonic structures. *Opt. Mater.* **72**, 403–421, https://doi.org/10.1016/j.optmat.2017.06.033 (2017).
36. Rodriguez, M. E. *et al*. Computational aspects of laser radiometric multiparameter fit for carrier transport property measurements in si wafers. *J. Electrochem. Soc.* **147**, 687, https://doi.org/10.1149/1.1393254 (2000).

37. Rodríguez, M. E. *et al*. Minority carrier lifetime and iron concentration measurements on p-si wafers by infrared photothermal radiometry and microwave photoconductance decay. *J. Appl. Phys.* **87**, 8113–8121, https://doi.org/10.1063/1.373506 (2000).
38. Ramirez-Gutierrez, C. F. *et al*. Photoluminescence study of porous p-type silicon: Identification of radiative transitions. *J. Lumin.* **201**, 11–17, https://doi.org/10.1016/j.jlumin.2018.04.036 (2018).
39. Lishchuk, P. *et al*. Photoacoustic characterization of nanowire arrays formed by metal-assisted chemical etching of crystalline silicon substrates with different doping level. *Phys. E* **107**, 131–136, https://doi.org/10.1016/j.physe.2018.11.016 (2019).
40. Lishchuk, P. *et al*. Interfacial thermal resistance between porous layers: Impact on thermal conductivity of a multilayered porous structure. *Int. J. Therm. Sci.* **134**, 317–320, https://doi.org/10.1016/j.ijthermalsci.2018.08.015 (2018).
41. Dubyk, K. *et al*. Features of photothermal transformation in porous silicon based multilayered structures. *Appl. Phys. Lett.* **115**, 021902, https://doi.org/10.1063/1.5099010 (2019).
42. Looyenga, H. Dielectric constants of heterogeneous mixtures. *Phys.* **31**, 401–406, https://doi.org/10.1016/0031-8914(65)90045-5 (1965).
43. Choy, T. C. *Effective Medium Theory Principles and Applications*, 1–24, 2 edn. (Oxford University Press, 2016)
44. Liu, X.-D. *et al*. A general model of dielectric constant for porous materials. *Appl. Phys. Lett.* **108**, 102902, https://doi.org/10.1063/1.4943639 (2016).
45. Li, B., Shaughnessy, D., Mandelis, A., Batista, J. & Garcia, J. Accuracy of photocarrier radiometric measurement of electronic transport properties of ion-implanted silicon wafers. *J. Appl. Phys.* **96**, 186–196, https://doi.org/10.1063/1.1755847 (2004).
46. Mandelis, A. Photo-carrier radiometry of semiconductors: A novel powerful optoelectronic diffusion-wave technique for silicon process non-destructive evaluation. *NDT E Int.* **39**, 244–252, https://doi.org/10.1016/j.ndteint.2005.07.009 (2006).
47. Garcia, J. A., Guo, X., Mandelis, A. & Simmons, A. Photo-carrier-radiometry (pcr) metrology for semiconductor manufacturing inspection. *AIP Conf. Proc.* **788**, 625–627, https://doi.org/10.1063/1.2063030 (2005).
48. Gutiérrez, A., Rodríguez-García, M. & Giraldo, J. Photoelectronic characterization of n-type silicon wafers using photocarrier radiometry. *Phys. B* **406**, 3687–3693, https://doi.org/10.1016/j.physb.2011.06.073 (2011).
49. Mandelis, A., Batista, J. & Shaughnessy, D. Infrared photocarrier radiometry of semiconductors: Physical principles, quantitative depth profilometry, and scanning imaging of deep subsurface electronic defects. *Phys. Rev. B* **67**, 205208, https://doi.org/10.1103/PhysRevB.67.205208 (2003).
50. Sailor, M. J. *Porous Silicon in Practice*, 14 (Wiley-VCH Verlag GmbH & Co. KGaA, 2011).
51. Ramirez-Gutierrez, C. F., Castaño-Yepes, J. D. & Rodriguez-García, M. E. Porosity and roughness determination of porous silicon thin films by genetic algorithms. *Optik* **173**, 271–278, https://doi.org/10.1016/j.ijleo.2018.08.019 (2018).
52. Ramirez-Gutierrez, C., Mosquera-Mosquera, J. & Rodríguez-García, M. Study of percolation and modeling of the order–disorder transition for zincblende–diamond structures: Percolation and the existence of a unique band of events. *Comput. Condens. Matter* **1**, 58–64, https://doi.org/10.1016/j.cocom.2014.11.003 (2014).
53. Torres-Costa, V., Martín-Palma, R. J. & Martínez-Duart, J. M. Optical constants of porous silicon films and multilayers determined by genetic algorithms. *J. Appl. Phys.* **96**, 4197–4203, https://doi.org/10.1063/1.1786672 (2004).
54. Lujan-Cabrera, I. A., Ramirez-Gutierrez, C. F., Castaño-Yepes, J. D. & Rodriguez-Garcia, M. E. Effects of the interface roughness in the optical response of one-dimensional photonic crystals of porous silicon. *Phys. B* **560**, 133–139, https://doi.org/10.1016/j.physb.2019.02.010 (2019).
55. Pacholski, C., Sartor, M., Sailor, M. J., Cunin, F. & Miskelly, G. M. Biosensing using porous silicon double-layer interferometers: Reflective interferometric fourier transform spectroscopy. *J. Am. Chem. Soc.* **127**, 11636–11645, https://doi.org/10.1021/ja0511671 (2005).
56. Smith, R. A. *Fluorine Compounds*, *Inorganic*, *Hydrogen*, 1–26 (American Cancer Society, 2003).
57. Pap, A. E. *et al*. Optical properties of porous silicon. part iii: Comparison of experimental and theoretical results. *Opt. Mater.* **28**, 506–513, https://doi.org/10.1016/j.optmat.2005.02.006 (2006).
58. Starkey, T. & Vukusic, P. Light manipulation principles in biological photonic systems. *Nanophotonics* **2**, 289–307, https://doi.org/10.1515/nanoph-2013-0015 (2013).
59. Green, M. A. Self-consistent optical parameters of intrinsic silicon at 300k including temperature coefficients. *Sol. Energy Mater. Sol. Cells* **92**, 1305–1310, https://doi.org/10.1016/j.solmat.2008.06.009 (2008).
60. Mitsas, C. L. & Siapkas, D. I. Generalized matrix method for analysis of coherent and incoherent reflectance and transmittance of multilayer structures with rough surfaces, interfaces, and finite substrates. *Appl. Opt.* **34**, 1678–1683, https://doi.org/10.1364/AO.34.001678 (1995).
61. Meek, R. L. n+ silicon-electrolyte interface capacitance. *Surf. Sci.* **25**, 526–536, https://doi.org/10.1016/0039-6028(71)90141-5 (1971).
62. Mogoda, A. S. & Ahmad, Y. H. Electrochemical impedance study of porous silicon prepared by metal-assisted chemical etching. *Silicon*, https://doi.org/10.1007/s12633-019-0077-4 (2019).

Acknowledgements

Cristian Felipe Ramirez-Gutierrez and Ivan Alonso Lujan-Cabrera thank CONACYT-México for their scholarship. This work was supported by PAEP program of Universidad Nacional Autónoma de México. Authors are eternally grateful to Laboratorio Nacional de Caracterización de Materiales (LaNCaM) for characterization material support, and Alicia del Real, Carmen Peza-Ledesma, and Rodrigo Esparza Muñoz for SEM experiments, and Beatriz Millan-Malo for her assistance in the simulations. Finally, the authors thank Liliana Tirado-Mejía and Julio Cesar Mosquera from Instituto Interdisciplinario de las Ciencias (IIC) of the Universidad del Quindío for the valuable discussions about optical models and PCR measurements.

Author Contributions

Cristian Felipe Ramirez-Gutierrez and Mario Enrique Rodriguez-Garcia designed the experiments and wrote the manuscript and analyzed results. Ivan Alonso Lujan-Cabrera and Harol David Martinez-Hernandez conducted the simulations, the experiments, and obtained all samples.

Additional Information

Competing Interests: The authors declare no competing interests.

Publisher's note Springer Nature remains neutral with regard to jurisdictional claims in published maps and institutional affiliations.